Ordered Spin States and Quantum Coherence in Low-Dimensional Structures: Quantum Dots and Nanowires

INAUGURALDISSERTATION

zur

Erlangung der Würde eines Doktors der Philosophie

vorgelegt der

Philosophisch-Naturwissenschaftlichen Fakultät

der Universität Basel

von

Viktoriia Kornich
aus Zaporizhzhya, Ukraine

Basel, 2016

Originaldokument gespeichert auf dem Dokumentenserver der Universität Basel
edoc.unibas.ch

Dieses Werk ist unter dem Vertrag „Creative Commons Namensnennung-Keine kommerzielle Nutzung-Keine Bearbeitung 2.5 Schweiz“ lizenziert. Die vollständige Lizenz kann unter
creativecommons.org/licences/by-nc-nd/2.5/ch
eingesehen werden.

Namensnennung-Keine kommerzielle Nutzung-Keine Bearbeitung 2.5 Schweiz

---

Sie dürfen:

das Werk vervielfältigen, verbreiten und öffentlich zugänglich machen

Zu den folgenden Bedingungen:

Namensnennung. Sie müssen den Namen des Autors/Rechteinhabers in der von ihm festgelegten Weise nennen (wodurch aber nicht der Eindruck entstehen darf, Sie oder die Nutzung des Werkes durch Sie würden entlohnt).

Keine kommerzielle Nutzung. Dieses Werk darf nicht für kommerzielle Zwecke verwendet werden.

Keine Bearbeitung. Dieses Werk darf nicht bearbeitet oder in anderer Weise verändert werden.

- Im Falle einer Verbreitung müssen Sie anderen die Lizenzbedingungen, unter welche dieses Werk fällt, mitteilen. Am Einfachsten ist es, einen Link auf diese Seite einzubinden.

- Jede der vorgenannten Bedingungen kann aufgehoben werden, sofern Sie die Einwilligung des Rechteinhabers dazu erhalten.
- Diese Lizenz lässt die Urheberpersönlichkeitsrechte unberührt.

Die gesetzlichen Schranken des Urheberrechts bleiben hiervon unberührt.

Die Commons Deed ist eine Zusammenfassung des Lizenzvertrags in allgemeinverständlicher Sprache: http://creativecommons.org/licenses/by-nc-nd/2.5/ch/legalcode.de

Haftungsausschluss:
Die Commons Deed ist kein Lizenzvertrag. Sie ist lediglich ein Referenztext, der den zugrundeliegenden Lizenzvertrag übersichtlich und in allgemeinverständlicher Sprache wiedergibt. Die Deed selbst entfaltet keine juristische Wirkung und erscheint im eigentlichen Lizenzvertrag nicht. Creative Commons ist keine Rechtsanwaltsgesellschaft und leistet keine Rechtsberatung. Die Weitergabe und Verlinkung des Commons Deeds führt zu keinem Mandatsverhältnis.

Quelle: http://creativecommons.org/licenses/by-nc-nd/2.5/ch/ Datum: 3.4.2009

Genehmigt von der Philosophisch-Naturwissenschaftlichen Fakultät auf Antrag von

Prof. Dr. Daniel Loss

Prof. Dr. Guido Burkard

Basel, den 23. Februar 2016

Prof. Dr. Jörg Schibler
Dekan

Acknowledgments

It is my great pleasure to thank all the people who helped, educated and encouraged me during my PhD studies.

First of all I would like to thank my advisor Prof. Daniel Loss, who accepted me as a PhD student in his group. I am very grateful for his guidance and help and the opportunity to work on many exciting projects. I would like to underline his ability to suggest the projects which are of great interest to the scientific community worldwide, and together with this to develop and support the great atmosphere in the group.

Furthermore, I would like to thank Prof. Guido Burkard who kindly agreed to co-referee my thesis and Prof. Christoph Bruder who chaired my PhD defense exam.

The work presented here would not have been possible without my collaborators Dr. Christoph Kloeffel, Dr. Tobias Meng, Dr. Peter Stano and Dr. Alexander A. Zyuzin. I had a great time working with them and benefited greatly from their scientific expertise and ideas.

I would like to thank Prof. Christoph Bruder, Dr. Vitaly N. Golovach, Dr. Niels Loerch, Prof. Thomas L. Schmidt, Dr. Rakesh Tiwari and Dr. James R. Wootton for numerous scientific discussions, help and encouragement.

I wish to underline the great role of many experimentalists in my research. I started my first project with the data obtained in the group of Prof. Amir Yacoby, who also kindly provided us the information about the sample. I enjoyed the visit to the group of Prof. Hendrik Bluhm and benefited a lot from discussions with him and Prof. David P. DiVincenzo, Dr. Lars Schreiber and Dr. Sebastian Mehl. The second project was connected to the research of the group of Prof. Martino Poggio, and I am very grateful to Benedikt Herzog for the detailed discussions about their measurements. I am also very grateful for the opportunity to work closely with the group of Prof. Dominik Zumbühl, who helped me to adjust to the new activity with the inspiring encouragement and respect. I had a great time working with his group members Taras Patlatiuk and

Dr. Christian Scheller. I would like to thank the group of Prof. Seigo Tarucha for the hospitality during my visit to RIKEN and interesting scientific discussions with Dr. Tomohiro Otsuka and Dr. Kenta Takeda.

I enjoyed many scientific discussions and social activities with the group members and visitors. My thanks to Samuel Aldana, Mohammad Alidoust, Ehud Amitai, Christoph Bruder, Daniel Becker, Bernd Braunecker, Stefano Chesi, Denis Chevallier, Carlos Egues, Gerson Ferreira, Suhas Gangadharaiah, Leonid Glazman, Silas Hoffman, Kevin van Hoogdalem, Adrian Hutter, Arthur Jaffe, Jelena Klinovaja, Christoph Kloeffel, Niels Loerch, Axel Lode, Franziska Maier, Dmitrii Maslov, Tobias Meng, Kouki Nakata, Simon Nigg, Andreas Nunnenkamp, Christoph Orth, Fabio Pedrocchi, Christina Psaroudaki, Diego Rainis, Hugo Ribeiro, Arijit Saha, Thomas Schmidt, Constantin Schrade, Tibor Sekera, Marcel Serina, Pascal Simon, Peter Stano, Dmitrije Stepanenko, Vladimir Stojanović, Grégory Strübi, Pavel Szumniak, Rakesh Tiwari, Mircea Trif, Luka Trifunovic, Andreas Wagner, Stefan Walter, Ying-Dan Wang, James Wootton, Robert Zielke, and Alexander Zyuzin. It is impossible to list here all bright and interesting researchers whom I have met during my PhD studies and whom I deeply grateful for their role in my professional life.

Finally, I want to thank my parents Grygoriy and Olga, my grandmother Valeriia, my sister Valeriia, and my whole family for their unconditional support and encouragement.

Summary

Since the development of microsized devices is moving forward at enormous speed, there is huge amount of new industrial opportunities. However such devices also require high precision and understanding of the operating of their constituent parts up to the quantum level. The device of the purely quantum nature being developed so far is quantum computer. However the physical realization of it is still not performed, as the requirements for it are very rigorous.

In the pioneering work by Loss and DiVincenzo it was suggested to use a spin of electron placed in a quantum dot as an information qubit. Following this work the study of electron or hole spin qubits developed. Both experimental and theoretical tools for studying them greatly advanced.

In the first part of the thesis we study the phonon-induced decoherence and relaxation of singlet-triplet qubits in the double quantum dots. First of all we consider AlGaAs/GaAs double quantum dots. The important result we present here is the strong dephasing that occurs at large detuning. This dephasing is due to two-phonon process that affects mainly singlet state of the qubit and consequently changes the splitting between singlet and triplet leading to dephasing. Remarkably at small detuning this dephasing process is suppressed and the decoherence time is by orders of magnitude longer than in case of large detuning and is mainly defined by one-phonon process. We also present the dependence of relaxation time and decoherence time on the strength of spin-orbit interaction and different directions of the system. Our results provide a deeper insight into the recently obtained experimental data.

We also studied Si/SiGe quantum dots as a potential candidate for a qubit. Apart from the absence of hyperfine interaction and bulk spin-orbit interaction in the isotopically purified ^{28}Si, its electron-phonon interaction is different from GaAs that also leads to longer qubit lifetimes. We study S-T_- qubit near the anticrossing of the basis states. This particular region is interesting due to possibilities in operating the qubit. We

show that the type of singlet plays a crucial role, i.e. whether it is a singlet with each dot singly occupied or a singlet with only one dot doubly occupied. Depending on the type of singlet the qubit lifetimes change by several orders of magnitude. We also study the influence of a micromagnet, usually used in experiments to operate the qubit, on the relaxation time and decoherence time and present the regime where its effect is negligible. We suggest how to test experimentally our theory of one-phonon and two-phonon processes separately. We also show how the relaxation and decoherence time depend on different system parameters for S-T_0 qubits.

The second part of the thesis is devoted to the other important constituent part of microsized devices, namely nanowires. We are interested in the dynamic of polarization of localized spins in the nanowires, as it can affect such important device characteristics as e.g. conductance.

We studied Ruderman-Kittel-Kasuya-Yosida (RKKY) interaction-induced polarization in the nanowire in case when the voltage is applied to it. It was already proposed theoretically that in the ground state the localized spins in 1D systems align in a helix due to RKKY interaction. This polarization is still present until some critical temperature. The presence of such polarization acts as a spin filter for electrons, that most likely affects the conductance of the nanowire. Therefore we studied how this helical polarization changes when the voltage is applied. The key result is the appearance of the uniform polarization perpendicular to the helix plane, that occurs due to backscattering of electrons that is accompanied by flip-flop process with localized spins. When this uniform polarization is formed, the helix starts to rotate as a whole around the direction of the uniform polarization. We present the dependence of polarization of the localized spins on temperature and voltage. Remarkably the uniform polarization grows both with voltage and temperature in the given range of parameters.

We also considered the electron-induced relaxation of the nuclear spins. As the electron spins and nuclear spins interact via hyperfine interaction, the nuclear relaxation time reflects some properties of electron bath. Namely, we see a strong dependence of nuclear relaxation time on spin-orbit interaction strength. We present here the dependence of the nuclear relaxation time on the external magnetic field and chemical potential of the wire, that can be experimentally varied via gate. The dependences for the strong spin-orbit interaction and for the weak one are substantially different. Moreover, they have distinct peaks, that allow to get the value of spin-orbit interaction amplitude with the high precision.

Contents

Contents ix

1 Introduction **1**
1.1 Quantum Computing based on the Loss-DiVincenzo proposal . . . 1
1.2 Ruderman-Kittel-Kasuya-Yosida interaction-induced helical polarization . . . 9

I Decoherence and Relaxation of the Singlet-Triplet Qubits

2 Introduction **16**

3 Phonon-mediated decay of singlet-triplet qubits in double quantum dots **19**
3.1 Introduction . . . 20
3.2 System, Hamiltonian, and Basis States . . . 21
3.3 Regime of Large Detuning . . . 24
3.4 Regime of Small Detuning . . . 35
3.5 Conclusions and outlook . . . 36
3.6 Acknowledgments . . . 37
3.A Basis States . . . 38
3.B Hamiltonian . . . 41
3.C Model Hamiltonian at small detuning . . . 51
3.D Model Hamiltonian at large detuning . . . 55
3.E Bloch-Redfield theory . . . 55
3.F Continuum Limit . . . 57
3.G Simple model for dephasing at large detuning . . . 58
3.H Dephasing via singlet states at small detuning . . . 61
3.I Summary of input parameters . . . 63

4 Phonon-assisted decay of singlet-triplet qubits in Si/SiGe quantum dots 66
4.1 Introduction 67
4.2 Model 67
4.3 S-T_- qubit 74
4.4 S-T_0 qubit 86
4.5 Comparison with other decay mechanisms 97
4.6 Conclusions 99
4.7 Acknowledgments 100
4.A Diagonalization of the Hamiltonian in the S-T_- basis . . . 100

II Ordered state and coherence of the localized spins in semiconductor nanowires

5 Introduction 104

6 Voltage-induced conversion of helical to uniform nuclear spin polarization in a nanowire 108
6.1 Introduction 109
6.2 The model 109
6.3 Helical electrons and finite voltage 114
6.4 Bloch Equation for the total nuclear spin in the wire 116
6.5 Resulting Polarizations 119
6.6 Conclusions 123
6.7 Acknowledgments 124
6.A Bloch equation for one nuclear spin 125

7 Nuclear spin relaxation in Rashba nanowires 127
7.1 Introduction 127
7.2 Relaxation in a non-interacting electron gas 129
7.3 Relaxation in an interacting electron system 133
7.4 Conclusions 137
7.5 Acknowledgements 138

Bibliography 139

CHAPTER 1

Introduction

In this chapter we introduce the basic concepts that will be used in this thesis. As half of the work presented here is about physical realization of the qubits for the quantum computer, we will start from introducing the ″Loss-DiVincenzo″ qubit and DiVincenzo criteria, see Sec. 1.1. We then discuss the spin states of electrons populating quantum dots as a basis for the qubit, main sources of decoherence, and consider singlet-triplet qubits in more details.

The other part of this thesis is about the polarization of localized spins in one-dimensional systems. One of the problems considered is an RKKY-induced polarization of localized spins. It was suggested theoretically, that in the ground state the localized spins tend to align along the helical direction [1]. However it was still unclear how the polarization reacts to the applied voltage, which might give a better insight into the behavior of the conductance of the nanowire, see Sec. 1.2. In the end of Sec. 1.2 we make a small note about Luttinger liquid theory which is widely used in describing the one-dimensional systems and in this thesis too.

1.1 Quantum Computing based on the Loss-DiVincenzo proposal

Quantum Computation and Quantum Information are one of the most rapidly developing areas of research in condensed matter physics worldwide. The reason for that is the following. Using quantum objects for computation would allow to solve the problems which are impossible to analyze using classical systems. As a simple example, to factor large numbers. However the conditions for the quantum computation are very restricting what makes it a challenge to actually build the quantum computer. These conditions that are known as DiVincenzo criteria [2] are the following:

- to find a system that can be defined as a quantum bit (qubit),
- the possibility to initialize a qubit in a predefined state and read out the final state,
- the lifetimes of the qubit states must be long enough to allow to perform a large number of qubit operations,
- the coherent control over qubit and interactions between qubits must be possible,
- scalability, i.e. it must be technically possible to use many qubits.

In the pioneering work by Loss and DiVincenzo [3] the information qubit is proposed to be based on the spin state of electron placed in the quantum dot. The quantum dot is suggested to be built in the semiconductor heterostructure using gates. The example of a lateral double quantum dot is shown in Fig. 1.1.

The Hamiltonian that describes the lowest states of the two electron spins in two quantum dots, when the wavefunctions of electrons slightly overlap, can be described using Heisenberg model

$$H_{12} = J(\tau)\boldsymbol{S}_1 \cdot \boldsymbol{S}_2, \tag{1.1}$$

where $\boldsymbol{S}_1$ and $\boldsymbol{S}_2$ are the spins of electrons, and $J(\tau)$ is the exchange coupling, that depends on time τ. In frame of Hubbard model $|J| = 4t^2(\tau)/U$, where U is the energy of the onsite repulsion and $t(\tau)$ is the tunneling coefficient that can be changed via gates. It was suggested to initialize the qubit and perform single qubit gates using a local magnetic field. The two-qubit gate can be performed via changing t. The readout is possible detecting electrostatically the change in the charge state due to the change in the spin state.

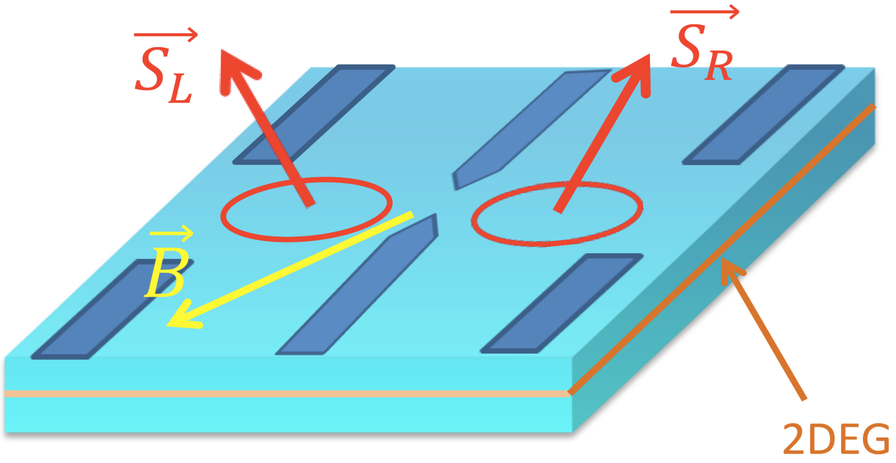

Figure 1.1: The scheme of the double quantum dot. Due to the band mismatch between the materials forming the heterostructure there is a two-dimensional electron gas (orange line). The gates on the top of the heterostructure form the electrostatic potential in the other two dimensions and allow to change the interaction between left spin ($\boldsymbol{S}_L$) and right spin ($\boldsymbol{S}_R$). The yellow arrow denotes the magnetic field B, that is usually applied.

Quantum dot populated by electron as a physical platform for a qubit

Quantum dots populated by one or more electrons or holes have become a widely studied systems as candidates for a physical realization of a logical qubit. There is a variety of methods to build quantum dots in different hosting materials. For example, self-assembled quantum dots, quantum dots in a nanowire, lateral quantum dots.

The self-assembled quantum dots are usually built via molecular beam epitaxy. Due to the lattice mismatch the growing material form islands on the host material surface. The widely used combination are GaAs as the host material and InGaAs as the growing one. Due to the difference in the structure of valence and conduction bands, there is a confinement potential in all three dimensions. As there is confinement in both valence band and conduction band, the quantum dot is populated by electron-hole pair and consequently is optically active. There are also experiments on Si and Ge based self-assembled quantum dots. Due to their band structure these quantum dots can be populated only by electrons or only by holes and consequently not active optically.

The other method is creating confinement in the nanowire in the remaining free dimension. This can be done for example via applying gates or structuring the growth of the nanowire in a certain way. Regarding the materials, the most popular ones for such quantum dots is InAs, however much attention recently attracted InSb and Ge/Si core-shell nanowires.

The quantum dot type we study in this work is lateral quantum dot. It is based on 2DEG, and the movement of electrons in the remaining two dimensions is confined via gates. The 2DEG is confined in the quantum well, which is formed due to bands mismatch of the materials in the heterostructure. The widely used heterostructures for the lateral quantum dots are AlGaAs/GaAs, however recently Si/SiGe also attracted much attention.

There are many different suggestions on how many dots should be used for a qubit and how many electrons or holes should populate them. For example, single dot with one electron, or with two electrons, double dot with two electrons, triple dot with three electrons, etc. It is still unclear which system is the best. One of the most often experimentally realized qubits is based on the spin states of two electrons in double quantum dots, namely singlet-triplet qubits [4, 5, 6]. The spin part of the possible basis electron wavefunctions are: $|S\rangle = \frac{|\uparrow\downarrow\rangle - |\downarrow\uparrow\rangle}{\sqrt{2}}$, $|T_0\rangle = \frac{|\uparrow\downarrow\rangle + |\downarrow\uparrow\rangle}{\sqrt{2}}$, $|T_-\rangle = |\downarrow\downarrow\rangle$, $|T_+\rangle = |\uparrow\uparrow\rangle$, where $|S\rangle$ and $|T_0\rangle$, $|T_-\rangle$, $|T_+\rangle$ denote singlet and triplet spin states with the magnetic quantum number 0, -1 and $+1$ respectively. Apart from singlet, one of the triplet states is normally chosen to form the qubit.

Coherence of the qubit

Among all the requirements for the qubit, one of the most challenging is the sufficently long lifetimes of the qubit states. For the lateral quantum dots the main sources of decoherence usually are:

- spin-orbit interaction,
- nuclear bath spins,
- electric noise in the gates,
- phonons.

The effect of nuclear spins can be schematically described as fluctuations of an Overhauser field, which they produce and which interacts with

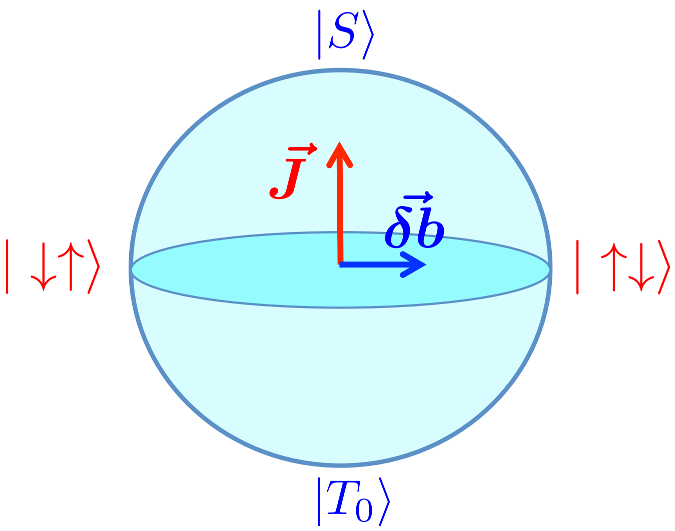

Figure 1.2: The Bloch sphere that describes the state of the qubit. The rotations $|S\rangle$-$|T_0\rangle$ are due to magnetic field gradient $\boldsymbol{\delta b}$, and the rotations $|\uparrow\downarrow\rangle$-$|\downarrow\uparrow\rangle$ are due to the exchange splitting J. Therefore if it is possible to control J and $\boldsymbol{\delta b}$, any state of the qubit (point on the Bloch sphere) can be reached.

the electron spin due to hyperfine interaction. However different experimental methods allowed to suppress this noise [7, 5]. First of all, Hahn echo technique, when in the middle of the evolution time of the qubit the echo-pulse is applied. There are also more compicated pulse techniques that allow to prolong the coherence of the qubit even more, for example, Carr-Purcell-Meiboom-Gillecho pulse sequence[8].

The other very useful method to suppress nuclear-induced decoherence of the qubit is dynamic nuclear polarization. It can be performed using the following scheme. The qubit is defined in the S-T_+ space near the anticrossing of these states. The initial state of the qubit is singlet, which then due to hyperfine interaction evolves into triplet. This is possible due to a flip-flop process between electron and nuclear spin. Repeating this procedure, the nuclear spins can be polarized in one direction [9]. The method of dynamic nuclear polarization allows to produce a stationary (compared to the electron spin lifetimes) polarization of nuclei that produce the effective magnetic field gradient δb. The reported measured value of it is of the order [7, 10] $\delta b \simeq 0.1\ \mu$eV. This effective magnetic field gradient leads not only to decoherence of the qubit, but is also used to control the state of the qubit [7]. For example, in S-T_0 qubits it allows for rotations in the plane S-T_0 (see Fig. 1.2). Therefore the logical space of S-T_0 qubit is fully controlled as the rotations in the plane $|\uparrow\downarrow\rangle$-$|\downarrow\uparrow\rangle$ is due to exchange coupling J, which in its turn is controlled via gates.

Similarly, spin-orbit interaction is both a source of decoherence and a tool to control the qubit. The spin-orbit interaction appears due to violation of a symmetry. For example, inversion symmetry of the crystal lattice. This kind of spin-orbit interaction was described by G. Dresselhaus [11]. For 2DEG grown along the direction [001] (we denote here the growth direction as z) the Hamiltonian for Dresselhaus spin-orbit interaction is

$$H_D \propto p_x p_y^2 \sigma_x - p_y p_x^2 \sigma_y - p_x \langle p_z^2 \rangle \sigma_x + p_y \langle p_z^2 \rangle \sigma_y, \tag{1.2}$$

where $p_x,\ p_y$ are the components of the momentum of the electron in the plane of 2DEG, and p_z is the momentum component out of the 2DEG plane. The first two terms in Eq. (1.2) are usually called as the "cubic" terms and the last two are the "linear" ones. As the width of 2DEG is usually around 100 times smaller than the dimensions of the dot in the 2DEG plane, $\langle p_z^2 \rangle \gg p_x p_y$, and consequently we can neglect the cubic terms in comparison to the linear ones.

The other kind of spin-orbit interaction is the one that appears often in the heterostructures due to the assymmetry of the quantum well or any other structural inversion assymetry, Rashba spin-orbit interaction. The Hamiltonian for it has the form

$$H_R \propto -p_y \sigma_x + p_x \sigma_y, \tag{1.3}$$

when the electric field produced by the given asymmetry is along z.

The physical meaning of spin-orbit interaction can be understood if we consider a single quantum dot populated by one electron. Let's say the electron in the quantum dot is in the state $|n, S\rangle$, where n includes all orbital quantum numbers and S denotes the spin state. We can see that the matrix elements of spin-orbit interaction between the same orbital states in the basis of non-perturbed electron wave functions are zero, because for the bound states $\langle p_{x,y} \rangle = 0$:

$$\langle n, S | H_{D,R} | n, S' \rangle \propto \underbrace{\langle n | p_{x,y} | n \rangle}_{=0} \langle S | \sigma_{x,y} | S' \rangle. \tag{1.4}$$

However it appears that the matrix elements of H_R and H_D are non-zero between the different orbital states with different spin states [12]. In the limit, when the Zeeman splitting due to the external magnetic field is much less than the orbital levels energy splitting, the electron wave functions corrected by spin-orbit interaction can be approximately written as

$$|n,\uparrow\rangle^{(1)} = |n,\uparrow\rangle + \sum_{n'\neq n} \frac{\langle n',\downarrow|H_{D,R}|n,\uparrow\rangle}{E_n - E_{n'} - E_Z}|n',\downarrow\rangle, \tag{1.5}$$

and for the state $|n,\downarrow\rangle$ analogously. Here E_Z is the Zeeman splitting due to the external magnetic field, E_n and $E_{n'}$ are the energies of the state with the orbital part n and n' respectively. We can see from Eq. (1.5), that the desired state of electron with the spin "up" is mixed with the higher orbital states with the opposite value of spin, "down". This means, that due to spin-orbit interaction the electron spin state can be affected by the sources of decoherence which do not have spins. For example, phonons.

However spin-orbit interaction can also be used to operate the qubit, for example Ref. [13]. In Ref. [13] was considered how the alternating electric field couples to the electron spin via spin-orbit interaction. This allows to control the qubit only by means of electric fields which is very convenient experimentally.

The electric fluctuations in the gates is also a significant source of decoherence and a subject to a wide study both theoretically and experimentally [10]. For example, it was shown recently that the low-frequency gate noise can be suppressed if the 2DEG is removed underneath the metallic gates [14].

As was mentioned above, even though phonons are spinless, they can be coupled to the spin of the electron via some interaction that mixes spin and orbital degrees of freedom, e.g. hyperfine or spin-orbit interactions. The hybridization of the qubit states with the other states also plays an important role, which we discuss in this thesis.

Following the development of experimental technique on singlet-triplet qubits and in particular the recent experiment by Dial *et. al*, Ref. [10], we studied singlet-triplet qubits based on two-electron spin states in a double quantum dot constructed in AlGaAs/GaAs and Si/SiGe heterostructures.

We show that the detuning between the quantum dots plays a crucial role in dephasing of S-T_0 qubit. The strong dephasing occurs when the detuning is enough large that the qubit subspace is close to the anticrossing between the singlet with each dot singly occupied $|(1,1)S\rangle$ and the singlet with the one dot doubly occupied $|(0,2)S\rangle$. Then as the phonons produce oscillations in detuning, which strongly affects the energy of

$|(0,2)S\rangle$, the exchange energy of the qubit oscillates too. As a consequence, the qubit loses its phase. We note that this process is a two-phonon process, the one-phonon process cannot produce dephasing. We also discuss the dependence of qubit lifetimes on spin-orbit interaction and angles between the dot axis and other directions in the system. The details and results can be found in Chapter 3.

Among all decoherence sources listed above the first two are characteristic for GaAs-based quantum dots. They can be avoided by changing the material to Si or Ge. Isotopically purified ^{28}Si or isotopes of Ge with the nuclear spin 0 allow to avoid the effects of hyperfine interaction between electron spin and nuclear spins. The spin-orbit interaction due to bulk inversion asymmetry is also absent in Si and Ge in contrast to GaAs. The Si/SiGe heterostructures usually used in experiments have rectangular quantum well, which confines 2DEG in the third direction. Whereas AlGaAs/GaAs heterostructures normally have triangular quantum well shape, that is a source of Rashba spin-orbit interaction.

Taking all above mentioned into account, Si and Ge based qubits seem to be attractive systems and there were many different suggestions for the actual qubit structure: donor electron spin, donor nuclear spin, nuclear-electron spin qubits, hole spin qubits in core-shell nanowires, and lateral quantum dots. We study the lifetimes of two types of singlet-triplet qubits based on spin states of two electrons in a double quantum dot: S-T_- and S-T_0 qubits. We consider the S-T_- qubit near the anti-crossing between singlet and triplet. In this case it is crucial whether the singlet if of type $|(1,1)S\rangle$ or of type $|(0,2)S\rangle$. The one of the type $|(1,1)S\rangle$ allows for several orders of magnitude longer times than the one of the type $|(0,2)S\rangle$. We also studied the dependence on the magnitude of the magnetic field gradient which is usually applied to operate the qubit [15, 16, 17, 18]. We showed that there is a range of values for the amplitude of magnetic field gradient where the one-phonon process dominates and the range, where the two-phonon process dominates. When the one-phonon process dominates, the qubit lifetimes can decrease by more than an order of magnitude. This happens because the one-phonon process depends strongly on the qubit energy splitting, which in this case is produced mainly by the applied magnetic field gradient. We also show and analyze the dependence of decoherence time and relaxation time on different sample parameters. All the results regarding the Si/SiGe double quantum dots are presented in Chapter 4.

1.2 Ruderman-Kittel-Kasuya-Yosida interaction-induced helical polarization

The self-ordered magnetic phases in mesoscopic systems is of high interest due to their possible use in different devices, e.g. memory [19] or sensors [20]. Apart from the obviously magnetically ordered ferromagnets, some attention attracted Ruderman-Kittel-Kasuya-Yosida (RKKY) interaction-induced magnetization in low-dimensional systems.

RKKY interaction is an effective interaction between localized spins mediated via electrons. The mechanism can be schematically described as follows. Electron spin and localized spin interact via hyperfine interaction

$$H_{hyp} \propto A\delta(R-r)\boldsymbol{\sigma}\cdot\boldsymbol{I}, \tag{1.6}$$

where A is the hyperfine constant, $\boldsymbol{\sigma}$ is the electron spin operator, $\boldsymbol{I}$ is the localized spin operator, and r and R are the positions of the electron and the localized spin respectively. When the electron comes close enough to the localized spin, their spins interact tending to align so that the energy is minimal. The electron moves further, encounters another localized spin and interacts with it in the same way as before. In such a way the electron delivers information about the first localized spin to the second one. This is a very simple model however it demonstrates the main message that localized spins do interact via electrons and therefore the ordered state of them is possible.

In a formal way RKKY interaction is derived as a second order perturbation in hyperfine interaction and has the form

$$H_{RKKY} = \sum_{i,j} \boldsymbol{I}_i \cdot J_{ij}\boldsymbol{I}_j, \tag{1.7}$$

where i, j label localized spins and J_{ij} is related to the static spin susceptibility of electrons.

The RKKY-induced polarization was studied in the bulk [21, 22] and in the two-dimensional structures [23, 24]. The possibility to control hole-induced ferromagnetism via electric field [25] is one of the important steps that might lead to the electric control of localized spins' states in semiconductors and consequently solve certain problems in quantum information technique. The manipulation of magnetization direction in such ferromagnetic semiconductors by electric field was already shown experimentally [26, 27].

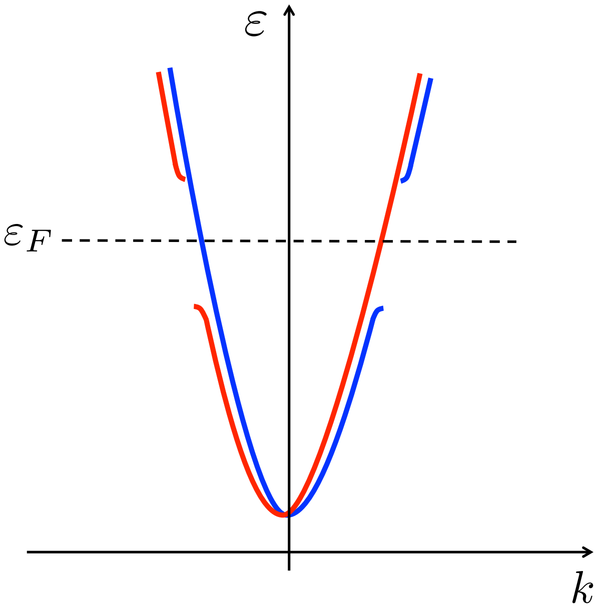

Figure 1.3: The spectrum of electrons in the helical Overhauser field produced by polarization of the localized spins. We see that the spin degeneracy is lifted in the partial gap, that presumably leads to the twofold decrease of the conductance.

It was shown theoretically that localized spins in the one-dimensional system in the ground state are polarized into a helix due to RKKY interaction [1, 28]. This helical polarization is still present up to critical temperature T_c. In the limit where the hyperfine constant A is much less than the electron Fermi energy ε_F, it can be assumed that electrons react instantaneously to the changes in localized spin subsystem. This allows to consider the effect of localized spins' polarization on electrons as an Overhauser field. Then the Hamiltonian of electrons is

$$H_{el} = -\frac{\hbar^2}{2m}\partial_r^2 + \mu_e \boldsymbol{B}_{Ov} \cdot \boldsymbol{\sigma}, \tag{1.8}$$

where $\hbar$ is the Planck constant, m is an effective mass of electrons, μ_e is the electron magnetic moment, and $\boldsymbol{B}_{Ov}$ is the Overhauser field. It was shown, that this Overhauser field produces a partial gap in the electron spectrum [1, 28]. Therefore it is natural to assume, that this gap affects the conductance of the nanowire. This was the main hypothesis that explains the experimental results presented in Ref. [29]. However the effect of current onto the electron-mediated polarization was still unclear.

It was shown by Slonczewski [30] and Berger [31] that when the electron current polarization differs from the polarization of the localized spins, the spin torque can appear. In the first work the magnetic multilayer consisting from ferromagnetic and paramagnetic sublayers was considered. It was shown that the current flowing perpendicular to the plane of the layers transfers the spin angular momentum between them. In the second work the "sandwich" structure was considered, consisting from ferromagnetic-normal-ferromagnetic metallic films. It was shown that when the current is driven through this structure the emission of spin waves takes place. Under certain conditions, spontaneous precession of the magnetization arises. There are also works on the effect of the current on domain walls [32, 33]. For example, it was shown that the current causes the domain wall to move [34, 35]. These examples show how complicated might be a reaction of spin system to a current flowing through it. Therefore to understand whether the presence of the localized spin helical polarization can explain the reduction of the conductance by 2 presented in Ref. [29], first of all the effect of current on the spin polarization should be studied. We address this problem in Chapter 6. The detailed study of electron-induced nuclear spin relaxation can be found in Chapter 7.

Luttinger Liquid Theory

Luttinger Liquid theory is the equivalent of the Fermi Liquid theory for one-dimensional systems. It is applicable only for the processes that involve the energies much smaller than the Fermi energy of electrons, however it is still very useful and gives results that are supported by experiments.

One of the main steps is linearizing of the electron spectrum around Fermi energy. Then the density fluctuations operator is defined as follows:

$$\rho^\dagger(q) = \sum_k c^\dagger_{k+q} c_k, \tag{1.9}$$

where k and q denote the momentums of electrons and $c^\dagger_k$, c_k are the creation and annihilation electron operators with the wavevector k respectively. As $\rho^\dagger(q)$ is a product of two fermionic operators, it is a bosonic operator. Using this operator we can introduce then bosonic fields ϕ and

θ:

$$\phi(x), \theta(x) = \mp \frac{i\pi}{L} \sum_{p\neq 0} \frac{1}{p} e^{-\alpha|p|/2 - ipx} (\rho_R^\dagger(p) \pm \rho_L^\dagger(p)) \mp (N_R \pm N_L) \frac{\pi x}{L}, \quad (1.10)$$

where x includes time and position coordinate and p includes frequency and momentum, L denotes the length of the one-dimensional system, N_R and N_L label the number of right-movers and left-movers respectively, and α is a cutoff that reintroduces the finite bandwidth in these formulas preventing momentum to become too large.

Using these bosonic fields one can represent Hamiltonian that describes electron-electron interaction in a quadratic form.

$$H = \frac{1}{2\pi} \int dx [uK(\nabla\theta(x))^2 + \frac{u}{K}(\nabla\phi(x))^2], \quad (1.11)$$

where K is the electron-electron interaction coefficient, and u is the velocity of excitations. This form of Hamiltonian allows to get a thermodynamic average of operators straightforwardly through the Gaussian integral and allows to use Wick's theorem. The great opportunities possible due to Luttinger liquid theory are widely studied and discussed in a number of reviews and books , e.g. Refs.[36, 37].

In this thesis we use Luttinger liquid theory to investigate critical temperature of the helical polarization of localized spins, when the voltage is applied and to study the behavior of the electron-induced relaxation time of nuclear spins in the nanowire.

Part I

Decoherence and Relaxation of the Singlet-Triplet Qubits

CHAPTER 2

Introduction

Adapted from:
Viktoriia Kornich, Christoph Kloeffel, and Daniel Loss
"Phonon-mediated decay of singlet-triplet qubits in double quantum dots",
Phys. Rev. B **89**, 085410 (2014),
ArXiv:1311.2197 (2014),

Viktoriia Kornich, Christoph Kloeffel, and Daniel Loss
"Phonon-assisted relaxation and decoherence of singlet-triplet qubits in Si/SiGe quantum dots",
ArXiv:1511.07369 (2016).

The spin states of quantum dots (QDs) are promising platforms for quantum computation [3, 38]. In particular, remarkable progress has been made with S-T_0 qubits in lateral GaAs double quantum dots (DQDs) [4, 6, 39, 40, 41], where a qubit is based on the spin singlet (S) and triplet (T_0) state of two electrons in the DQD. In this encoding scheme, rotations around the z axis of the Bloch sphere can be performed on a subnanosecond timescale [39] through the exchange interaction, and rotations around the x axis are enabled by magnetic field gradients across the QDs [6].

The lifetimes of S-T_0 qubits have been studied with great efforts. When the qubit state precesses around the x axis, dephasing mainly results from Overhauser field fluctuations, leading to short dephasing times $T_2^* \sim 10\,\text{ns}$ [7, 39, 42, 43, 44, 45]. This low-frequency noise can be dynamically decoupled with echo pulses [39, 46, 47, 48], and long decoherence times $T_2 > 200\,\mu$s have already been measured [47]. In contrast to x-rotations, precessions around the z axis dephase predominantly due to charge noise [10, 49]. Rather surprisingly, however, recent Hahn echo experiments by Dial *et al.* [10] revealed a relatively short $T_2 \simeq$ 0.1–1 μs and a power-law dependence of T_2 on the temperature T. The dependence on T suggests that lattice vibrations (phonons) may play an important role.

Much progress both in theory and experiment was made in studying GaAs-based QDs [4, 5, 8, 15, 41, 42, 43, 44, 45, 50, 51, 52, 53, 54, 55, 56, 57, 58, 59]. However, recently Si or Ge based QDs attracted much attention. The reason is that in isotopically purified ^{28}Si or isotopes of Ge with nuclear spin 0 (e.g. ^{76}Ge) decoherence sources characteristic to GaAs are absent, namely hyperfine interaction and spin orbit interaction (SOI) due to lattice-inversion asymmetry. Known schemes for spin qubits in Si or Ge are based on, e.g., donor electron spins [60, 61, 62, 63], host [64] and donor [65, 66, 67, 68, 69] nuclear spins, nuclear-electron spin qubits (Si:Bi) [70], qubits based on Si/SiO$_2$ structures [71, 72, 73], hole spin qubits in Ge-Si core-shell nanowires [74, 75, 76, 77], and lateral QDs within the 2D electron gas (2DEG) in Si/SiGe heterostructures [16, 78, 79]. The sixfold degeneracy of conduction band valleys in Si can be an additional source of decoherence [80] compared to GaAs. However, four of the six valleys get split off by a large energy of the order of a hundred meV in SiGe/Si/SiGe quantum wells because of the strain [81]. Due to confinement, which may also be varied via electric fields, the twofold degeneracy of the remaining valleys is lifted, and reported valley splittings are of the order of 0.1–1 meV [81, 82, 83, 84]. For instance, electric control over the valley splitting for QDs in Si/SiO$_2$ was reported, and the presented energy range for the valley splitting is 0.3–0.8 meV [84]. Therefore, it is possible to suppress the effect of many valleys in Si if the energies characteristic for the qubit subspace are small enough.

CHAPTER 3

Phonon-mediated decay of singlet-triplet qubits in double quantum dots

Adapted from:
Viktoriia Kornich, Christoph Kloeffel, and Daniel Loss
"Phonon-mediated decay of singlet-triplet qubits in double quantum dots",
Phys. Rev. B **89**, 085410 (2014),
ArXiv:1311.2197 (2014).

We study theoretically the phonon-induced relaxation (T_1) and decoherence times (T_2) of singlet-triplet qubits in lateral GaAs double quantum dots (DQDs). When the DQD is biased, Pauli exclusion enables strong dephasing via two-phonon processes. This mechanism requires neither hyperfine nor spin-orbit interaction and yields $T_2 \ll T_1$, in contrast to previous calculations of phonon-limited lifetimes. When the DQD is unbiased, we find $T_2 \simeq 2T_1$ and much longer lifetimes than in the biased DQD. For typical setups, the decoherence and relaxation rates due to one-phonon processes are proportional to the temperature T, whereas the rates due to two-phonon processes reveal a transition from T^2 to higher powers as T is decreased. Remarkably, both T_1 and T_2 exhibit a maximum when the external magnetic field is applied along a certain axis within the plane of the two-dimensional electron gas. We compare our results with recent experiments and analyze the dependence of T_1 and T_2 on system properties such as the detuning, the spin-orbit parameters, the hyperfine coupling, and the orientation of the DQD and the applied magnetic field with respect to the main crystallographic axes.

3.1 Introduction

In this Chapter, we calculate the phonon-induced lifetimes of a S-T_0 qubit in a lateral GaAs DQD. Taking into account the spin-orbit interaction (SOI) and the hyperfine coupling, we show that one- and two-phonon processes can become the dominant decay channels in these systems and may lead to qubit lifetimes on the order of microseconds only. While the decoherence and relaxation rates due to one-phonon processes scale with T for the parameter range considered here, the rates due to two-phonon processes scale with T^2 at rather high temperatures and obey power laws with higher powers of T as the temperature decreases. Among other things, the qubit lifetimes depend strongly on the applied magnetic field, the interdot distance, and the detuning between the QDs. Based on the developed theory, we discuss how the lifetimes can be significantly prolonged.

This Chapter is organized as follows. In Sec. 3.2 we present the Hamiltonian and the basis states of our model. In the main part, Sec. 3.3, we discuss the calculation of the lifetimes in a biased DQD and investigate the results in detail. In particular, we show that two-phonon processes lead to short dephasing times and identify the magnetic field direction at which the lifetimes peak. The results for unbiased DQDs are discussed in Sec. 3.4, followed by our conclusions in Sec. 3.5. Details and further information are appended.

3.2 System, Hamiltonian, and Basis States

We consider a lateral GaAs DQD within the two-dimensional electron gas (2DEG) of an AlGaAs/GaAs heterostructure that is grown along the [001] direction, referred to as the z axis. Confinement in the x-y-plane is generated by electric gates on the sample surface, and the magnetic field $\boldsymbol{B}$ is applied in-plane to avoid orbital effects. When the DQD is occupied by two electrons, the Hamiltonian of the system reads

$$\begin{aligned} H &= \sum_{j=1,2} \left(H_0^{(j)} + H_Z^{(j)} + H_{\mathrm{SOI}}^{(j)} + H_{\mathrm{hyp}}^{(j)} + H_{\mathrm{el-ph}}^{(j)} \right) \\ & \quad + H_C + H_{\mathrm{ph}}, \end{aligned} \tag{3.1}$$

where the index j labels the electrons, H_0 comprises the kinetic and potential energy of an electron in the DQD potential, H_Z is the Zeeman coupling, H_{SOI} is the SOI, H_{hyp} is the hyperfine coupling to the nuclear spins, $H_{\mathrm{el-ph}}$ is the electron-phonon coupling, H_C is the Coulomb repulsion, and H_{ph} describes the phonon bath.

The electron-phonon interaction has the form

$$H_{\mathrm{el-ph}} = \sum_{\boldsymbol{q},s} W_s(\boldsymbol{q}) a_{\boldsymbol{q}s} e^{i\boldsymbol{q}\cdot\boldsymbol{r}} + \mathrm{h.c.}, \tag{3.2}$$

where $\boldsymbol{r}$ is the position of the electron, $\boldsymbol{q}$ is a phonon wave vector within the first Brillouin zone, $s \in \{l, t_1, t_2\}$ stands for the longitudinal (l) and the two transverse (t_1, t_2) phonon modes, and "h.c." is the hermitian conjugate. The coefficient $W_s(\boldsymbol{q})$ depends strongly on $\boldsymbol{q}$ and s, and is determined by material properties such as the relative permittivity ϵ_r, the density ρ, the speed v_l (v_t) of a longitudinal (transverse) sound wave, and the constants Ξ and h_{14} for the deformation potential and piezoelectric coupling, respectively. The annihilation operator for a phonon of wave vector $\boldsymbol{q}$ and mode s is denoted by $a_{\boldsymbol{q}s}$. The Hamiltonian

$$H_{\mathrm{SOI}} = \alpha \left(p_{x'}\sigma_{y'} - p_{y'}\sigma_{x'} \right) + \beta \left(p_{y'}\sigma_{y'} - p_{x'}\sigma_{x'} \right) \tag{3.3}$$

contains both Rashba and Dresselhaus SOI. Here $p_{x'}$ and $p_{y'}$ are the momentum operators for the x' and y' axes, respectively. The latter coincide with the crystallographic axes [100] and [010], respectively, and $\sigma_{x'}$

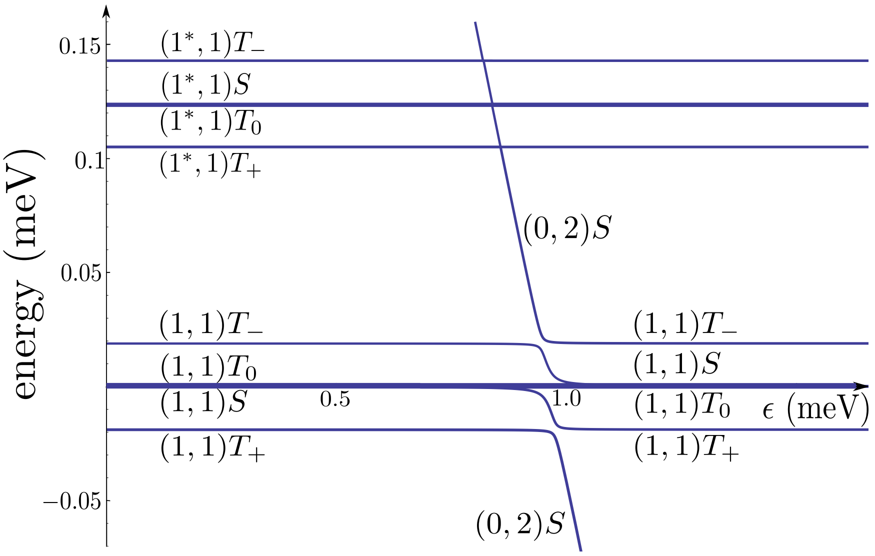

Figure 3.1: The energy spectrum of the DQD calculated for the parameters described in the text. The S-T_0 qubit is formed by the eigenstates of type $|(1,1)S\rangle$ and $|(1,1)T_0\rangle$.

and $\sigma_{y'}$ are the corresponding Pauli operators for the electron spin. We take into account the coupling to states of higher energy by performing a Schrieffer-Wolff transformation that removes H_{SOI} in lowest order [12, 85, 86, 87, 88, 89, 90]. The resulting Hamiltonian $\widetilde{H}$ is equivalent to H, except that H_{SOI} is replaced by

$$\widetilde{H}_{\mathrm{SOI}} \simeq g\mu_B(\boldsymbol{r}_{\mathrm{SOI}} \times \boldsymbol{B}) \cdot \boldsymbol{\sigma}, \tag{3.4}$$

where g is the in-plane g factor, $\boldsymbol{\sigma}$ is the vector of Pauli matrices, and

$$\boldsymbol{r}_{\mathrm{SOI}} = \left(\frac{y'}{l_R} + \frac{x'}{l_D}\right)\boldsymbol{e}_{[100]} - \left(\frac{x'}{l_R} + \frac{y'}{l_D}\right)\boldsymbol{e}_{[010]}. \tag{3.5}$$

Here x' and y' are the coordinates of the electron along the main crystallographic axes, whose orientation is provided by the unit vectors $\boldsymbol{e}_{[100]}$ and $\boldsymbol{e}_{[010]}$, respectively. The spin-orbit lengths are defined as $l_R = \hbar/(m_{\mathrm{eff}}\alpha)$ and $l_D = \hbar/(m_{\mathrm{eff}}\beta)$, where m_{eff} is the effective electron mass in GaAs and α (β) is the Rashba (Dresselhaus) coefficient. For our analysis, the most relevant effect of the nuclear spins is the generation of an effective magnetic field gradient between the QDs, which is accounted for by H_{hyp}.

We note that this magnetic field gradient may also result from a nearby positioned micromagnet [91, 92, 93]. For details of H and $\widetilde{H}$, see Appendix 3.B.

The S-T_0 qubit in this work is formed by the basis states $|(1,1)S\rangle$ and $|(1,1)T_0\rangle$, where the notation (m,n) means that m (n) electrons occupy the left (right) QD. In first approximation, these states read

$$|(1,1)S\rangle = |\Psi_+\rangle|S\rangle, \tag{3.6}$$

$$|(1,1)T_0\rangle = |\Psi_-\rangle|T_0\rangle, \tag{3.7}$$

with

$$|\Psi_\pm\rangle = \frac{|\Phi_L^{(1)}\Phi_R^{(2)}\rangle \pm |\Phi_R^{(1)}\Phi_L^{(2)}\rangle}{\sqrt{2}}, \tag{3.8}$$

where the $\Phi_{L,R}(\boldsymbol{r})$ are orthonormalized single-electron wave functions for the left and right QD, respectively (see also Appendix 3.A) [50, 94]. The spin singlet is

$$|S\rangle = \frac{|\uparrow\downarrow\rangle - |\downarrow\uparrow\rangle}{\sqrt{2}}, \tag{3.9}$$

whereas

$$|T_0\rangle = \frac{|\uparrow\downarrow\rangle + |\downarrow\uparrow\rangle}{\sqrt{2}}, \tag{3.10}$$

with the quantization axis of the spins along $\boldsymbol{B}$. Analogously, one can define the states $|(1,1)T_+\rangle = |\Psi_-\rangle|\uparrow\uparrow\rangle$ and $|(1,1)T_-\rangle = |\Psi_-\rangle|\downarrow\downarrow\rangle$, which are energetically split from the qubit by $\pm g\mu_B|\boldsymbol{B}|$. For our analysis of the phonon-induced lifetimes, a simple projection of $\widetilde{H}$ onto this 4D subspace of lowest energy is not sufficient, because

$$\sum_j \Big(\langle\Psi_+|H^{(j)}_{\mathrm{el-ph}}|\Psi_+\rangle - \langle\Psi_-|H^{(j)}_{\mathrm{el-ph}}|\Psi_-\rangle \Big) = 0. \tag{3.11}$$

That is, corrections from higher states must be taken into account in order to obtain finite lifetimes [89, 95]. The spectrum that results from the states considered in our model is plotted in Fig. 3.1. Depending on the detuning ϵ between the QDs, the lifetimes of the qubit are determined by admixtures from $|(2,0)S\rangle$, $|(0,2)S\rangle$, or states with excited orbital parts.

3.3 Regime of Large Detuning

Effective Hamiltonian and Bloch-Redfield theory

We first consider the case of a large, positive detuning ϵ at which the energy gap between $|(0,2)S\rangle$ and the qubit states is smaller than the orbital level spacing $\hbar\omega_0$. In this regime, contributions from states with excited orbital parts are negligible, and projection of $\widetilde{H}$ onto the basis states $|(1,1)T_0\rangle$, $|(1,1)S\rangle$, $|(1,1)T_+\rangle$, $|(1,1)T_-\rangle$, $|(0,2)S\rangle$, and $|(2,0)S\rangle$ yields

$$\tilde{H} = \begin{pmatrix} P_T & \frac{\delta b_B}{2} & 0 & 0 & 0 & 0 \\ \frac{\delta b_B}{2} & V_+ - V_- + P_T & \frac{\Omega}{\sqrt{2}} & -\frac{\Omega}{\sqrt{2}} & -\sqrt{2}t + P_S^\dagger & -\sqrt{2}t + P_S \\ 0 & \frac{\Omega}{\sqrt{2}} & E_Z + P_T & 0 & 0 & 0 \\ 0 & -\frac{\Omega}{\sqrt{2}} & 0 & -E_Z + P_T & 0 & 0 \\ 0 & -\sqrt{2}t + P_S & 0 & 0 & -\epsilon + U - V_- + P_{SR} & 0 \\ 0 & -\sqrt{2}t + P_S^\dagger & 0 & 0 & 0 & \epsilon + U - V_- + P_{SL} \end{pmatrix} + H_{\text{ph}}. \tag{3.12}$$

Here P_T, P_S, $P_S^\dagger$, P_{SL}, and P_{SR} are the matrix elements of the electron-phonon interaction, t is the tunnel coupling, U is the on-site repulsion,

$V_\pm = \langle \Psi_\pm | H_C | \Psi_\pm \rangle$, $E_Z = g\mu_B |\boldsymbol{B}|$,

$$\Omega = g\mu_B \Big(\langle \Phi_L | (\boldsymbol{r}_{\mathrm{SOI}} \times \boldsymbol{B})_z | \Phi_L \rangle - \langle \Phi_R | (\boldsymbol{r}_{\mathrm{SOI}} \times \boldsymbol{B})_z | \Phi_R \rangle \Big), \tag{3.13}$$

and $\delta b_B = 2\langle (1,1)S | H_{\mathrm{hyp}} | (1,1)T_0 \rangle$ (see also Appendix 3.B). We note that the energy in Eq. (3.12) was globally shifted by $\langle (1,1)T_0 | \big(H_0^{(1)} + H_0^{(2)} + H_C \big) | (1,1)T_0 \rangle$. Furthermore, we mention that the state $|(2,0)S\rangle$ is very well decoupled when ϵ is large and positive. In Eq. (3.12), $|(2,0)S\rangle$ is mainly included for illustration purposes, allowing also for large and negative ϵ and for an estimate of the exchange energy at $\epsilon \simeq 0$.

In order to decouple the qubit subspace $\{|(1,1)S\rangle, |(1,1)T_0\rangle\}$, we first apply a unitary transformation to $\widetilde{H}$ that diagonalizes $\widetilde{H} - \sum_j H_{\mathrm{el-ph}}^{(j)}$ exactly. Then we perform a third-order Schrieffer-Wolff transformation that provides corrections up to the third power in the electron-phonon coupling, which is sufficient for the analysis of one- and two-phonon processes. The resulting effective Hamiltonian can be written as $H_{\mathrm{q}} + H_{\mathrm{q-ph}}(\tau) + H_{\mathrm{ph}}$ in the interaction representation, where the time is denoted by τ to avoid confusion with the tunnel coupling. Introducing the effective magnetic fields $\boldsymbol{B}_{\mathbf{eff}}$ and $\boldsymbol{\delta B}(\tau)$ and defining $\boldsymbol{\sigma'}$ as the vector of Pauli matrices for the S-T_0 qubit,

$$H_{\mathrm{q}} = \frac{1}{2} g\mu_B \boldsymbol{B}_{\mathbf{eff}} \cdot \boldsymbol{\sigma'} \tag{3.14}$$

describes the qubit and

$$H_{\mathrm{q-ph}}(\tau) = \frac{1}{2} g\mu_B \boldsymbol{\delta B}(\tau) \cdot \boldsymbol{\sigma'} \tag{3.15}$$

describes the interaction between the qubit and the phonons. The time dependence results from

$$H_{\mathrm{q-ph}}(\tau) = e^{iH_{\mathrm{ph}}\tau/\hbar} H_{\mathrm{q-ph}} e^{-iH_{\mathrm{ph}}\tau/\hbar}. \tag{3.16}$$

For convenience, we define the basis of $\boldsymbol{\sigma'}$ such that $B_{\mathrm{eff},x} = 0 = B_{\mathrm{eff},y}$. Following Refs. [86, 96], the decoherence time (T_2), the relaxation time (T_1), and the dephasing contribution (T_φ) to T_2 of the qubit can then be calculated via the Bloch-Redfield theory (see also Appendix 3.E), which yields

$$\frac{1}{T_2} = \frac{1}{2T_1} + \frac{1}{T_\varphi}, \tag{3.17}$$

$$\frac{1}{T_1} = J^+_{xx}(\omega_Z) + J^+_{yy}(\omega_Z), \tag{3.18}$$

$$\frac{1}{T_\varphi} = J^+_{zz}(0), \tag{3.19}$$

where $\hbar\omega_Z = J_{\text{tot}} = |g\mu_B \boldsymbol{B}_{\text{eff}}|$ and

$$J^+_{ii}(\omega) = \frac{g^2\mu_B^2}{2\hbar^2}\int_{-\infty}^{\infty} \cos(\omega\tau)\langle\delta B_i(0)\delta B_i(\tau)\rangle d\tau. \tag{3.20}$$

The correlator $\langle\delta B_i(0)\delta B_i(\tau)\rangle$ is evaluated for a phonon bath in thermal equilibrium and depends strongly on the temperature T.

Input parameters

The material properties of GaAs are $g = -0.4$, $m_{\text{eff}} = 6.1\times10^{-32}$ kg, $\epsilon_r \simeq 13$, $\rho = 5.32\,\text{g/cm}^3$, $v_l \simeq 5.1\times10^3$ m/s and $v_t \simeq 3.0\times10^3$ m/s (see also Appendix 3.B)[97, 98, 99], $h_{14} \simeq -0.16$ As/m^2[98, 99, 100], and $\Xi \approx -8$ eV [101, 102]. In agreement with $\omega_0/(2\pi) = 30$ GHz [10], we set $l_c = \sqrt{\hbar/(m_{\text{eff}}\omega_0)} \simeq 96$ nm, which is the confinement length of the QDs due to harmonic confining potential in the x-y plane. For all basis states, the orbital part along the z axis is described by a Fang-Howard wave function [103] of width $3a_z = 6$ nm (see Appendix 3.A). Unless stated otherwise, we set $l_R = 2\ \mu\text{m}$ and $l_D = 1\ \mu\text{m}$ [104, 105, 106], where l_D is consistent with the assumed a_z (see also Appendix 3.I) [106]. We note, however, that adapting a_z to l_D is not required, because changing the width of the 2DEG by several nanometers turns out not to affect our results. All calculations are done for $|\boldsymbol{B}| = 0.7$ T [7, 40], $\delta b_B = -0.14\ \mu$eV, in good agreement with, e.g., Refs. [7, 10], and an interdot distance of $2a = 400$ nm. For Figs. 3.1–3.5 (large ϵ), we use $U = 1$ meV, $t = 7.25\ \mu$eV, and $V_+ = 40\ \mu$eV [94]. We choose here $V_- = 39.78\ \mu$eV such that the resulting energy splitting $J_{\text{tot}}(\epsilon)$ between the qubit states is mostly determined by the hyperfine coupling at $\epsilon \to 0$, as commonly realized experimentally [10, 39]. The detuning ϵ is then set such that $0 < U - V_\pm - \epsilon < \hbar\omega_0$ and $J_{\text{tot}} = 1.43\ \mu$eV, and we note that this splitting is within the range studied in Ref. [10].

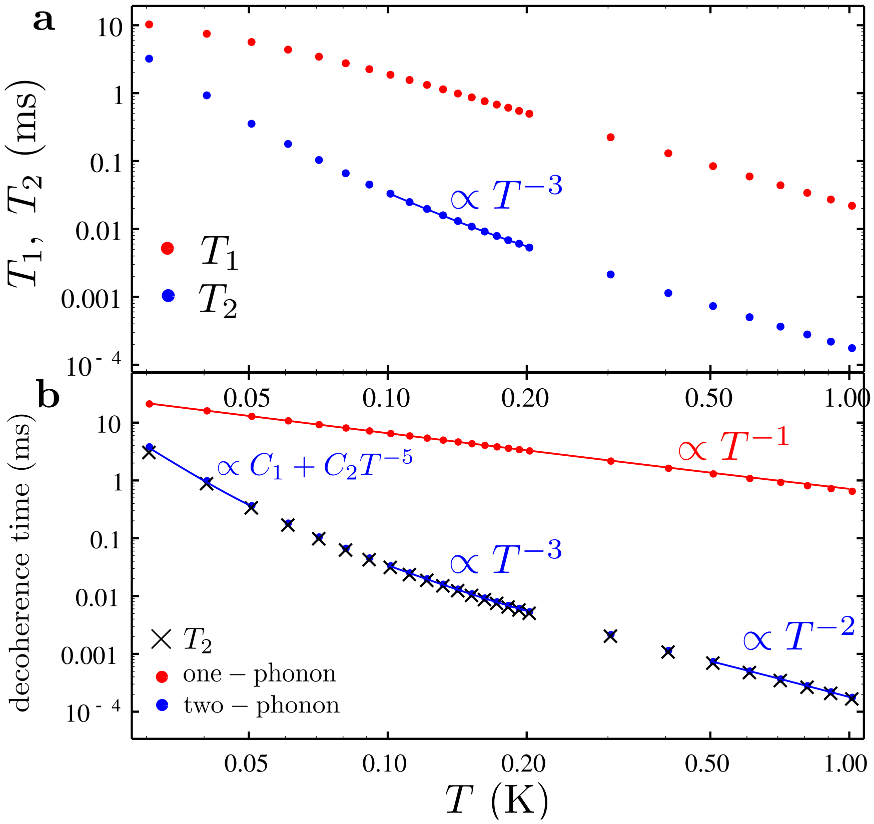

Figure 3.2: (a) Temperature dependence of the decoherence time (T_2, blue) and relaxation time (T_1, red) for the parameters in the text. The solid line corresponds to a power-law fit to T_2 for 0.1 K $\leq T \leq$ 0.2 K, which yields $T_2 \propto T^{-3}$ and good agreement with recent experiments [10]. We note that $T_2 \ll T_1$. (b) The decoherence time due to one-phonon ($1/\Gamma_2^{1\mathrm{p}}$) and two-phonon processes ($1/\Gamma_2^{2\mathrm{p}}$) and the full decoherence time $T_2 = 1/\Gamma_2 = 1/(\Gamma_2^{1\mathrm{p}} + \Gamma_2^{2\mathrm{p}})$ as a function of temperature. We note that $1/\Gamma_2^{2\mathrm{p}}$ changes its behaviour from $\propto C_1 + C_2T^{-5}$ to $\propto T^{-2}$, where C_1 and C_2 are constants, whereas $1/\Gamma_2^{1\mathrm{p}} \propto T^{-1}$ for the range of T considered here.

Temperature dependence

Figures 3.1–3.3 consider $\boldsymbol{B}$ applied along the x axis that connects the two QDs, assuming that the x axis coincides with the crystallographic $[110]$ direction. The geometry $x \parallel [110]$ is realized in most experiments [46, 48, 49], particularly because GaAs cleaves nicely along [110]. In stark contrast to previous theoretical studies of phonon-limited lifetimes, where $T_2 = 2T_1$ [76, 86, 107, 108, 109], Fig. 3.2(a) reveals $T_2 \ll T_1$ at $30\ \mathrm{mK} \leq T \leq 1\ \mathrm{K}$ considered here, which implies $T_\varphi \ll T_1$. In the discussion below we therefore focus on the details of the temperature dependence of $\Gamma_2 = 1/T_2$. We note, however, that the contributions to Γ_2 and $\Gamma_1 = 1/T_1$ from one-phonon processes scale similarly with T, and analogously for two-phonon processes. Defining Γ_2^{1p} (Γ_2^{2p}) as the decoherence rate due to one-phonon (two-phonon) processes, Fig. 3.2(b) illustrates $\Gamma_2^{\mathrm{2p}} \gg \Gamma_2^{\mathrm{1p}}$, and so $\Gamma_2 = \Gamma_2^{\mathrm{1p}} + \Gamma_2^{\mathrm{2p}} \simeq \Gamma_2^{\mathrm{2p}}$. In the considered range of temperatures, we find $\Gamma_2^{\mathrm{1p}} \propto T$. This behavior results from the fact that $\hbar\omega_Z/(k_B T) < 1$ for our parameters, where k_B is the Boltzmann constant. Therefore, the dominant terms in the formula for Γ_2^{1p} are proportional to Bose-Einstein distributions defined as

$$n_B(\omega) = \frac{1}{e^{\hbar\omega/(k_B T)} - 1} \tag{3.21}$$

and may all be expanded according to $n_B(\omega) \simeq k_B T/(\hbar\omega)$, keeping in mind that the $n_B(\omega)$ contributing to Γ_2^{1p} are evaluated at $\omega = \omega_Z$ because of energy conservation. The time $1/\Gamma_2^{\mathrm{2p}}$ due to two-phonon processes smoothly changes its behaviour from $C_1 + C_2 T^{-5}$ at $T \sim 40\ \mathrm{mK}$ to T^{-2} with increasing temperature, where C_n are constants. This transition is explained by the fact that, in the continuum limit, the rate corresponds to an integral over the phonon wave vector $\boldsymbol{q}$, where the convergence of this integral is guaranteed by the combination of the Bose-Einstein distribution and the Gaussian suppression that results from averaging over the electron wave functions. More precisely, the decay rate is obtained by integrating over the wave vectors of the two involved phonons. Due to conservation of the total energy, however, considering only one wave vector $\boldsymbol{q}$ is sufficient for this qualitative discussion. For Γ_2^{2p}, we find that the dominating terms decay with $\boldsymbol{q}$ due to factors of type

$$f_s(\boldsymbol{q}) = e^{-(q_x^2+q_y^2)l_c^2} n_B(\omega_{\boldsymbol{q}s}) \left[n_B(\omega_{\boldsymbol{q}s}) + 1 \right], \tag{3.22}$$

where q_x and q_y are the projections of $\boldsymbol{q}$ onto the x and y axis, respectively, and $\hbar\omega_{\boldsymbol{q}s} = \hbar v_s |\boldsymbol{q}|$ is the phonon energy. Whether the Bose-Einstein part or the Gaussian part from $f_s(\boldsymbol{q})$ provides the convergence of the integral depends on l_c, $v_s \in \{v_l, v_t\}$, and mainly T, as the latter can be changed significantly. When the Gaussian part $\exp[-(q_x^2 + q_y^2)l_c^2]$ cuts the integral, $\Gamma_2^{\mathrm{2p}} \propto T^2$ due to the expansion $n_B(n_B + 1) \simeq (k_B T)^2/(\hbar\omega_{\boldsymbol{q}s})^2$ that applies in this case. When $n_B(n_B + 1)$ affects the convergence of the integral, terms with higher powers of T occur. The resulting temperature dependence is rather complex, but is usually well described by

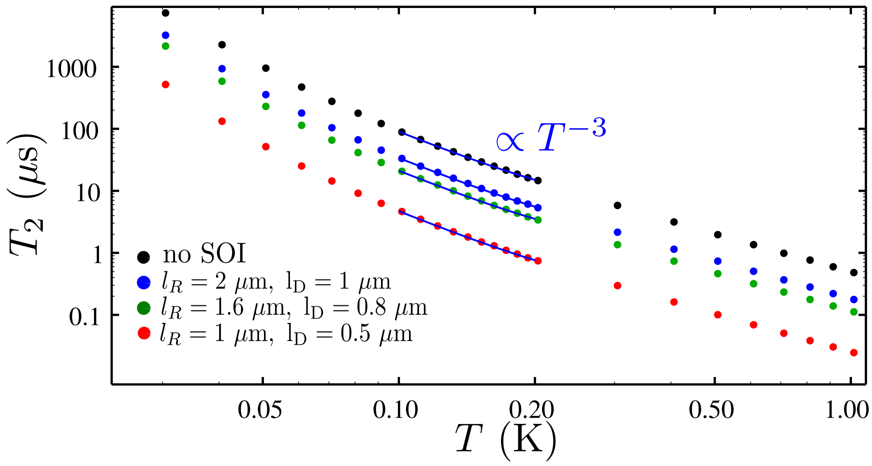

Figure 3.3: Dependence of the decoherence time T_2 on the temperature for the parameters in the text and different spin-orbit lengths. Keeping the splitting J_{tot} between the qubit states constant, the values chosen for the detuning ϵ are 0.896 meV (black), 0.912 meV (blue), 0.918 meV (green), and 0.933 meV (red), increasing with increasing SOI. Within the range $T = 100$–200 mK, $T_2 \propto T^{-3}$ in all cases. We note that the best quantitative agreement with the experiment [10] is obtained for the strongest SOI (red), where $l_R = 1\ \mu$m and $l_D = 0.5\ \mu$m.

$1/\Gamma_2^{\text{2p}} = C_m + C_n T^{-\nu}$ with $\nu \geq 2$ for different ranges of T [see Fig. 3.2(b)]. The temperature ranges for the different regimes are determined by the details of the setup and the sample. For the parameters considered here, a power-law approximation $T_2 \propto T^{\eta}$ for $T = 100$–200 mK yields $\eta \simeq -3$ mainly because of the dephasing due to two-phonon processes (see Figs. 3.2 and 3.3), which agrees well with the experimental data of Ref. [10].

Figure 3.3 shows the resulting temperature dependence of T_2 for different spin-orbit lengths. Remarkably, the calculation yields short T_2 even when SOI is completely absent. Keeping $J_{\text{tot}} = 1.43\ \mu$eV fixed by adapting the value of ϵ, one finds that T_2 decreases further with increasing SOI. As seen in Eq. (3.12), $\widetilde{H}_{\text{SOI}}$ couples $|(1,1)S\rangle$ to the triplet states $|(1,1)T_+\rangle$ and $|(1,1)T_-\rangle$. An important consequence of the resulting admixtures is that greater detunings are required in order to realize a desired J_{tot}. In Fig. 3.3, for instance, ϵ increases from 0.896 meV (no SOI) to 0.933 meV ($l_R = 1\ \mu$m, $l_D = 0.5\ \mu$m). As explained below, increasing ϵ decreases the lifetimes because it enhances the effects of $|(0,2)S\rangle$ through reduction of the energy gap (see also Fig. 3.1).

Origin of strong dephasing

The results discussed thus far have revealed two special features of the phonon-mediated lifetimes of S-T_0 qubits in biased DQDs. First, $T_2 \ll T_1$, as seen in Fig. 3.2(a). Second, the strong decay does not require SOI, as seen in Fig. 3.3. These features have not been observed in previous calculations for, e.g., spin qubits formed by single-electron [86, 104] or single-hole [107, 108] or two-electron [89] states in GaAs QDs, hole-spin qubits in Ge/Si nanowire QDs[76], or electron-spin qubits in graphene QDs [109]. Therefore, we discuss the dominant decay mechanism for S-T_0 qubits in DQDs in further detail and provide an intuitive explanation for our results.

Assuming again a large, positive detuning ϵ, with $0 < U - V_\pm - \epsilon < \hbar\omega_0$, and setting $\Omega = 0$ (no SOI), the states $|(1,1)T_+\rangle$, $|(1,1)T_-\rangle$, and $|(2,0)S\rangle$ of Eq. (3.12) are practically decoupled from the qubit. The relevant dynamics are then very well described by

$$\widetilde{H} = \begin{pmatrix} 0 & \frac{\delta b_B}{2} & 0 \\ \frac{\delta b_B}{2} & V_+ - V_- & -\sqrt{2}t + P_S^\dagger \\ 0 & -\sqrt{2}t + P_S & -\epsilon + U - V_- + \widetilde{P} \end{pmatrix} + H_{\text{ph}}, \tag{3.23}$$

with $|(1,1)T_0\rangle$, $|(1,1)S\rangle$, and $|(0,2)S\rangle$ as the basis states and

$$\widetilde{P} = P_{SR} - P_T. \tag{3.24}$$

In the absence of SOI, the hyperfine interaction (δb_B) is the only mechanism that couples the spin states and enables relaxation of the S-T_0 qubit. We note that even when Ω is nonzero the relaxation times T_1 are largely determined by the hyperfine coupling instead of the SOI for the parameters considered in this work. At sufficiently large temperatures, where $T_2 \ll T_1$, δb_B is negligible in the calculation of T_2, leading to pure dephasing, $T_2 = T_\varphi$. In addition, the matrix element P_S turns out to be negligible for our parameters. Following Appendix 3.G, we finally obtain

$$\frac{1}{T_2} = \frac{1}{T_\varphi} = \frac{2t^4}{\hbar^2 (\Delta_S')^6} \int_{-\infty}^{\infty} \langle \widetilde{P}^2(0) \widetilde{P}^2(\tau) \rangle d\tau \tag{3.25}$$

from this simple model, where

$$\Delta_S' = \sqrt{(U - V_+ - \epsilon)^2 + 8t^2} \tag{3.26}$$

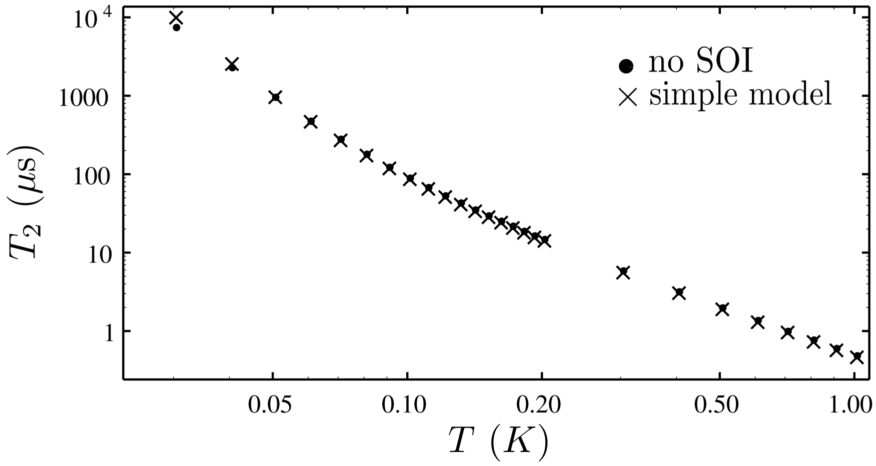

Figure 3.4: Decoherence time T_2 as a function of temperature from two different models. The dotted line is also shown in Fig. 3.3 and was calculated via Eq. (3.12), using the parameters in the text with $\Omega = 0$ (no SOI) and $\epsilon = 0.896$ meV. The crosses result from Eq. (3.25), using exactly the same parameters. We note that the associated J_{tot} differ only slightly. The remarkable agreement demonstrates that the simple model of Sec. 3.3 accounts for the dominant decay mechanism. At $T \lesssim 50$ mK, the curves start to deviate because relaxation is no longer negligible. When the hyperfine coupling in Eq. (3.23) is not omitted, excellent agreement is obtained also at low temperatures.

corresponds to the energy difference between the eigenstates of type $|(1,1)S\rangle$ and $|(0,2)S\rangle$ (using $\delta_B = 0$). We note that terms of type $a^\dagger_{\boldsymbol{q}s}a_{\boldsymbol{q}s}$ and $a_{\boldsymbol{q}s}a^\dagger_{\boldsymbol{q}s}$ must be removed from $\widetilde{P}^2$ in Eq. (3.25), as the Bloch-Redfield theory requires $\langle \boldsymbol{\delta B}(\tau)\rangle$ to vanish (see also Appendix 3.G) [110]. In Fig. 3.4, we compare T_2 from Eq. (3.25) with T_2 derived from Eq. (3.12) for $\Omega = 0$ (see also Fig. 3.3), and find excellent agreement at $T \gtrsim 50$ mK where relaxation is negligible.

The above analysis provides further insight and gives explanations for the results observed in this work. First, Eq. (3.25) illustrates that dephasing requires two-phonon processes and cannot be achieved with a single phonon only. As dephasing leaves the energy of the electrons and the phonon bath unchanged, the single phonon would have to fulfill $\omega_{\boldsymbol{q}s} = 0 = |\boldsymbol{q}|$. However, phonons with infinite wavelengths do not affect the lifetimes, which can be explained both via $e^{i\boldsymbol{q}\cdot\boldsymbol{r}} \to 1$ [see Eq. (3.2)] and via the vanishing density of states at $\omega_{\boldsymbol{q}s} \to 0$ for acoustic phonons in bulk. Thus, $\Gamma_2^{\rm 1p} = \Gamma_1^{\rm 1p}/2$ in all our calculations, where $\Gamma_1^{\rm 1p}$ is the relaxation rate due to one-phonon processes. Second, as discussed above, we find that the hyperfine interaction in combination with electron-phonon coupling presents an important source of relaxation in this system [90]. Third, the strong dephasing at large detuning ϵ results from two-phonon processes between states of type $|(1,1)S\rangle$ and $|(0,2)S\rangle$. This mechanism is very effective because the spin state remains unchanged. Therefore, the dephasing requires neither SOI nor hyperfine coupling, and we note that Eq. (3.25) reveals a strong dependence of T_φ on the tunnel coupling t and the splitting Δ'_S. Hence, the short T_φ in the biased DQD can be interpreted as a consequence of the Pauli exclusion principle. When the energy of the right QD is lowered ($\epsilon > 0$), the singlet state of lowest energy changes from $|(1,1)S\rangle$ toward $|(0,2)S\rangle$, since the symmetric orbital part of the wave function allows double-occupancy of the orbital ground state in the right QD. The triplet states, however, remain in the (1,1) charge configuration. While this feature allows tuning of the exchange energy and readout via spin-to-charge conversion on the one hand,[39] it enables strong dephasing via electron-phonon coupling on the other hand: effectively, phonons lead to small fluctuations in ϵ; due to Pauli exclusion, these result in fluctuations of the exchange energy and, thus, in dephasing [111]. This mechanism is highly efficient in biased DQDs, but strongly suppressed in unbiased ones, as we show in Sec. 3.4 and Appendix 3.H.

We note that the two-phonon process that doesn't require SOI or hyperfine interaction, and still leads to dephasing, corresponds to two-phonon Raman process. It was studied for impurity atoms [112, 113, 114, 115], considering also singlet states [113, 114, 115]. This mechanism is used in Ref. [111], where the dephasing of singlet-triplet qubits in the unbiased DQDs is studied. We note that our conclusions are substantially different from the conclusions presented in Ref. [111]. While Ref. [111] finds this Raman process as a dominating source of dephasing, we find that in the case of unbiased DQD it produces negligible dephasing for realistic system parameters (see Appendix 3.H).

Angular dependence

We also calculate the dependence of T_1 and T_2 on the angle between $\boldsymbol{B}$ and the x axis, assuming that $x \parallel [110]$. The results for $T = 100\,\mathrm{mK}$ and $J_{\rm tot} = 1.43\,\mu\mathrm{eV}$ are plotted in Fig. 3.5. Remarkably, the phonon-induced lifetimes of the qubit are maximal when $\boldsymbol{B} \perp x$ and minimal

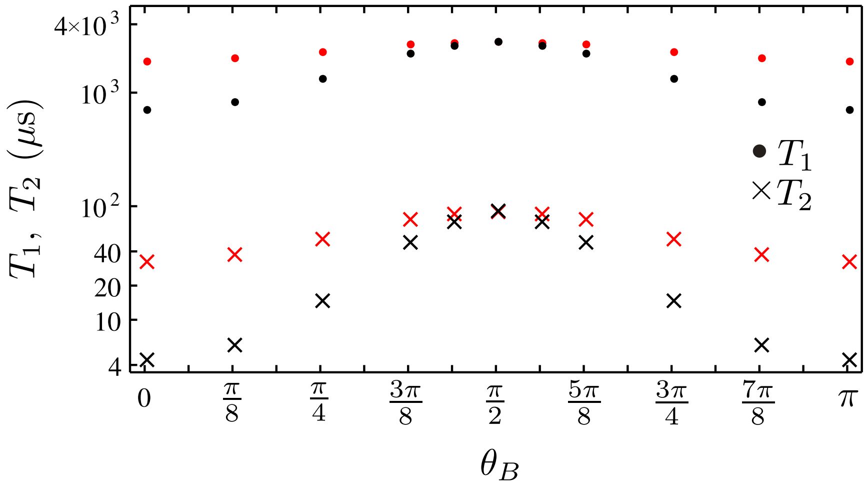

Figure 3.5: Dependence of the relaxation (T_1) and decoherence time (T_2) on the angle θ_B between the in-plane magnetic field $\boldsymbol{B}$ and the x axis that connects the QDs. When $\boldsymbol{B} \perp x$ $(\theta_B = \pi/2)$, both T_1 and T_2 exhibit a maximum. Red (black) corresponds to the spin-orbit lengths $l_R = 2\ \mu\text{m}$ and $l_D = 1\ \mu\text{m}$ ($l_R = 1\ \mu\text{m}$ and $l_D = 0.5\ \mu\text{m}$). For the stronger SOI, the lifetimes increase by almost two orders of magnitude. For details, see text.

when $\boldsymbol{B} \parallel x$. The difference between minimum and maximum increases strongly with the SOI, and for $l_R = 1\ \mu\text{m}$ and $l_D = 0.5\ \mu\text{m}$ we already expect improvements by almost two orders of magnitude. These features can be understood via the matrix elements of the effective SOI [88, 89, 90],

$$\Omega = F_{\text{SOI}}(a, l_c) E_Z \frac{l_D \cos(\theta_B - \theta) + l_R \cos(\theta_B + \theta)}{l_D l_R}, \tag{3.27}$$

where θ_B (θ) is the angle between $\boldsymbol{B}$ (the x axis) and the crystallographic axis [110], and $F_{\text{SOI}}(a, l_c)$ is a function of a and l_c. From this result, we conclude that there always exists an optimal orientation for the in-plane magnetic field for which the effective SOI is suppressed and, thus, for which the phonon-mediated decay of the qubit state is minimal (comparing the lifetimes at fixed J_{tot}). Remarkably, one finds for $x \parallel [110]$ $(\theta = 0)$ that this suppression always occurs when $\boldsymbol{B} \perp x$ $(\theta_B = \pi/2)$, independent of l_R and l_D. In the case where $\Omega = 0$, the finite T_2 in our model results from admixtures with $|(0,2)S\rangle$, as explained in Sec. 3.3. Due to the hyperfine interaction, these admixtures also lead to finite T_1. We wish to emphasize, however, that suppression of the effective SOI only results in a substantial prolongation of the lifetimes when the spin-orbit lengths are rather short, as the dominant decay mechanism in biased DQDs is very effective even at $\Omega = 0$.

3.4 Regime of Small Detuning

All previous results were calculated for a large detuning $\epsilon \sim U - V_\pm$. Now we consider an unbiased DQD, i.e., the region of very small ϵ. The dominant decay mechanism in the biased DQD is strongly suppressed at $\epsilon \simeq 0$, where the basis states $|(2,0)S\rangle$ and $|(0,2)S\rangle$ are both split from $|(1,1)S\rangle$ by a large energy $U - V_+$. Adapting the simple model behind Eq. (3.25) to an unbiased DQD yields

$$\frac{8t^4}{\hbar^2 (U - V_+)^6} \int_{-\infty}^{\infty} \langle \widetilde{P}^2(0) \widetilde{P}^2(\tau) \rangle d\tau \tag{3.28}$$

as the associated dephasing time (see Appendix 3.H for details). Comparing the prefactor with that of Eq. (3.25) results in a remarkable suppression factor below 10^{-4} for the parameters in this work. As explained in Appendix 3.H, this suppression factor may also be estimated via $(\Delta'_S)^4/(U - V_+)^4$ for fixed J_{tot}, where Δ'_S is the splitting between the eigenstates of type $|(1,1)S\rangle$ and $|(0,2)S\rangle$ at large ϵ and $U - V_+$ is the abovementioned splitting at $\epsilon \simeq 0$.

Consequently, the lifetimes T_1 and T_2 in the unbiased DQD are no longer limited by $|(2,0)S\rangle$ or $|(0,2)S\rangle$, but by states with an excited orbital part (see Fig. 3.1). We therefore extend the subspace by the basis states $|(1^*,1)S\rangle$, $|(1^*,1)T_0\rangle$, $|(1^*,1)T_+\rangle$, and $|(1^*,1)T_-\rangle$, and proceed analogously to the case of large detuning (see Appendixes 3.A and 3.C for details). The asterisk denotes that the electron is in the first excited state, leading to an energy gap of $\hbar\omega_0$ compared to the states without asterisk. Setting $\boldsymbol{B} \parallel x \parallel [110]$, the orbital excitation is taken along the x axis, because states with the excitation along y turn out to have negligible effects on the qubit lifetimes. From symmetry considerations, states with the excited electron in the right QD should only provide quantitative corrections of the lifetimes by factors on the order of 2 and are therefore neglected in this analysis. The resulting temperature dependence of T_2, $1/\Gamma_2^{\mathrm{1p}}$, and $1/\Gamma_2^{\mathrm{2p}}$ is shown in Fig. 3.6. The plotted example illustrates that two-phonon processes affect T_2 only at rather high temperatures when ϵ is small, leading to $T_2 \propto T^{-1}$ for a wide range of T due to single-phonon

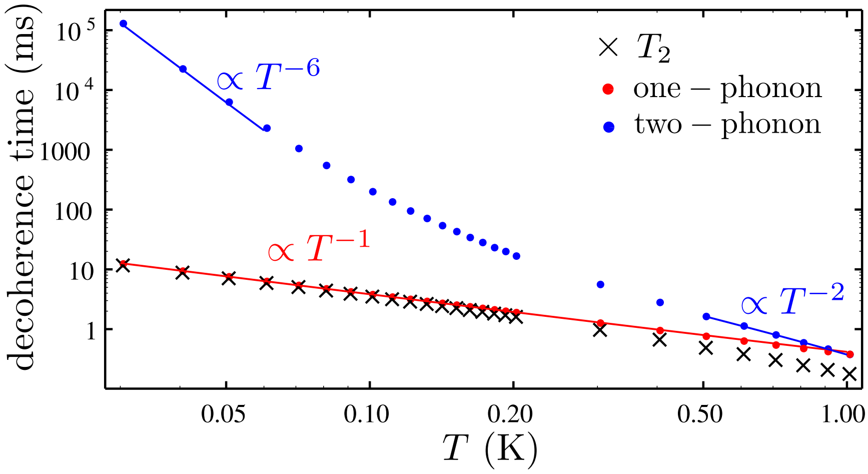

Figure 3.6: Temperature dependence of the decoherence time (T_2) and its one-phonon $(1/\Gamma_2^{1p})$ and two-phonon $(1/\Gamma_2^{2p})$ parts for the detuning $\epsilon \simeq 0$, where excited states are taken into account. For this plot $U = 1$ meV, $V_+ = 50\ \mu$eV, $V_- = 49.5\ \mu$eV, $t = 24\ \mu$eV, $J_{\text{tot}} = 1.41\ \mu$eV, and the other paramters as described in the text. We note that $T_2 \simeq 2T_1$.

processes. In stark contrast to the biased DQD, we find $T_2 \simeq 2T_1$. Remarkably, the absolute value of T_2 is of the order of milliseconds, which exceeds the T_2 at large ϵ by 2–3 orders of magnitude. For $\boldsymbol{B} \perp x$, $x \parallel [110]$, and typical sample temperatures $T \sim 0.1$ K, we find that the lifetimes can be enhanced even further.

3.5 Conclusions and outlook

In conclusion, we showed that one- and two-phonon processes can be major sources of relaxation and decoherence for S-T_0 qubits in DQDs. Our theory provides a possible explanation for the experimental data of Ref. [10], and we predict that the phonon-induced lifetimes are prolonged by orders of magnitude at small detunings and, when the SOI is strong, at certain orientations of the magnetic field. Our results may also allow substantial prolongation of the relaxation time recently measured in resonant exchange qubits [116].

While the model developed in this work applies to a wide range of host materials, the resulting lifetimes depend on the input parameters and, thus, on the setup and the heterostructure. By separately neglecting the deformation potential coupling ($\Xi = 0$) and the piezoelectric coupling ($h_{14} = 0$), we find that the qubit lifetimes of Figs. 3.2–3.6 for GaAs DQDs are limited by the piezoelectric electron-phonon interaction, the latter providing much greater decay rates than the deformation potential coupling. Consequently, the phonon-limited lifetimes of singlet-triplet qubits may be long in group-IV materials such as Ge or Si [81, 117, 118], where the piezoelectric effect is absent due to bulk inversion symmetry.

Essentially, there are two different schemes for manipulating singlet-triplet qubits in DQDs electrically. The first and commonly realized approach is based on biased DQDs and uses the detuning to control the exchange energy [39]. Alternatively, the exchange energy can be controlled by tuning the tunnel barrier [3] rather than the detuning. Our results suggest that the second approach is advantageous, as it applies to unbiased DQDs for which the phonon-mediated decay of the qubit state is strongly suppressed. In addition, one finds $dJ_{\mathrm{tot}}/d\epsilon \propto \epsilon$ at very small detunings ϵ [50], which implies that not only $dJ_{\mathrm{tot}}/d\epsilon \simeq 0$ but also $\langle dJ_{\mathrm{tot}}/d\epsilon \rangle \simeq 0$ at $\epsilon \simeq 0$, where $\langle \cdots \rangle$ now stands for the average over some random fluctuations of ϵ. Therefore, singlet-triplet qubits in unbiased DQDs are also protected against electrical noise. The latter, for instance, turned out to be a major obstacle for the implementation of high-fidelity controlled-phase gates between S-T_0 qubits [40]. Keeping in mind that two-qubit gates for singlet-triplet qubits may also be realized with unbiased DQDs [41], we conclude that operation at $\epsilon \simeq 0$ with a tunable tunnel barrier is a promising alternative to the commonly realized schemes that require nonzero detuning. As single-qubit gates for S-T_0 qubits correspond to two-qubit gates for single-electron spin qubits, the regime $\epsilon \simeq 0$ is also beneficial for many other encoding schemes.

3.6 Acknowledgments

We thank Peter Stano, Fabio L. Pedrocchi, Mircea Trif, James R. Wootton, Robert Zielke, Hendrik Bluhm, and Amir Yacoby for helpful discussions and acknowledge support from the Swiss NF, NCCR QSIT, S^{3}NANO, and IARPA.

3.A Basis States

We consider a GaAs/AlGaAs heterostructure that contains a two-dimensional electron gas (2DEG). Electric gates on the top of the sample induce a double quantum dot (DQD) potential that confines electrons and enables the implementation of a singlet-triplet qubit. Assuming that this spin qubit is based on low-energy states of two electrons in the DQD, we consider the four states of lowest energy,

$$\begin{aligned}
|(1,1)S\rangle &= |\Psi_+\rangle|S\rangle, && (3.29)\\
|(1,1)T_+\rangle &= |\Psi_-\rangle|T_+\rangle, && (3.30)\\
|(1,1)T_0\rangle &= |\Psi_-\rangle|T_0\rangle, && (3.31)\\
|(1,1)T_-\rangle &= |\Psi_-\rangle|T_-\rangle, && (3.32)
\end{aligned}$$

two states with a doubly occupied quantum dot (QD),

$$\begin{aligned}
|(0,2)S\rangle &= |\Psi_R\rangle|S\rangle, && (3.33)\\
|(2,0)S\rangle &= |\Psi_L\rangle|S\rangle, && (3.34)
\end{aligned}$$

and four additional states that feature one electron in a first excited orbital state,

$$\begin{aligned}
|(1^*,1)S\rangle &= |\Psi_+^e\rangle|S\rangle, && (3.35)\\
|(1^*,1)T_+\rangle &= |\Psi_-^e\rangle|T_+\rangle, && (3.36)\\
|(1^*,1)T_0\rangle &= |\Psi_-^e\rangle|T_0\rangle, && (3.37)\\
|(1^*,1)T_-\rangle &= |\Psi_-^e\rangle|T_-\rangle, && (3.38)
\end{aligned}$$

as the basis in this problem. In the notation used above, the first and second index in parentheses corresponds to the occupation number of the left and right QD, respectively. The asterisk denotes that the electron in the QD is in the first excited state. The spin part of the wave functions consists of the singlet $|S\rangle$ and the triplets $|T_0\rangle$, $|T_+\rangle$, and $|T_-\rangle$,

$$\begin{aligned}
|S\rangle &= \frac{|\uparrow\downarrow\rangle - |\downarrow\uparrow\rangle}{\sqrt{2}}, && (3.39)\\
|T_0\rangle &= \frac{|\uparrow\downarrow\rangle + |\downarrow\uparrow\rangle}{\sqrt{2}}, && (3.40)\\
|T_+\rangle &= |\uparrow\uparrow\rangle, && (3.41)\\
|T_-\rangle &= |\downarrow\downarrow\rangle, && (3.42)
\end{aligned}$$

where ↑ (↓) corresponds to an electron spin oriented along (against) the externally applied magnetic field, see Appendix 3.B.

As the two minima in the DQD potential may be approximated by the confining potential of a 2D harmonic oscillator, the one-particle wave functions for ground and first excited states can be constructed from the eigenstates of the harmonic oscillators.[50] Defining the growth axis of the heterostructure as the z axis, we consider harmonic confinement potentials around $(x, y) = (\pm a, 0)$ with $l_c = \sqrt{\hbar/(m_{\text{eff}}\omega_0)}$ as the confinement length in the QDs. The x axis connects the two QDs, pointing from the left to the right one. The interdot distance is $L = 2a$, m_{eff} is the effective mass of electrons in GaAs, and $\hbar\omega_0$ is the orbital level spacing in each QD. With these definitions, the orbital parts of the 2D harmonic oscillator wave functions (ground, excited along x, excited along y) can be written as

$$\phi_{L,R}(x,y) = \frac{1}{\sqrt{\pi}l_c} e^{-[(x\pm a)^2+y^2]/(2l_c^2)}, \tag{3.43}$$

$$\phi^x_{L,R}(x,y) = \sqrt{\frac{2}{\pi l_c^4}}(x \pm a) e^{-[(x\pm a)^2+y^2]/(2l_c^2)}, \tag{3.44}$$

$$\phi^y_{L,R}(x,y) = \sqrt{\frac{2}{\pi l_c^4}} y e^{-[(x\pm a)^2+y^2]/(2l_c^2)}. \tag{3.45}$$

The confining potential along the z axis may be considered as a triangular potential of type

$$V(z) = \begin{cases} \infty, & z < 0, \\ Cz, & z > 0, \end{cases} \tag{3.46}$$

where C is a positive constant with units energy/length and $z = 0$ corresponds to the interface between AlGaAs ($z < 0$) and GaAs ($z > 0$). The ground state in such a potential can be approximated by the Fang-Howard wave function [103],

$$\phi_{\text{FH}}(z) = \theta(z)\frac{z}{\sqrt{2a_z^3}} e^{-z/(2a_z)}, \tag{3.47}$$

with a_z as a positive length and

$$\theta(z) = \begin{cases} 0, & z < 0, \\ 1, & z > 0, \end{cases} \tag{3.48}$$

as the Heaviside step function. The Fang-Howard wave function from Eq. (3.47) is normalized and fulfills

$$\langle \phi_{\text{FH}} | z | \phi_{\text{FH}} \rangle = 3a_z, \tag{3.49}$$

which may be interpreted as the width of the 2DEG.

Following Refs. [94, 50, 119] for constructing wave functions in the DQD potential, we define overlaps between the harmonic oscillator wave functions,

$$\begin{aligned} s &= \langle\phi_L|\phi_R\rangle = e^{-\frac{a^2}{l_c^2}}, && (3.50)\\ s_x &= \langle\phi_L^x|\phi_R^x\rangle = s\left(1-\frac{2a^2}{l_c^2}\right), && (3.51)\\ s_y &= \langle\phi_L^y|\phi_R^y\rangle = s, && (3.52) \end{aligned}$$

and

$$\begin{aligned} g &= \frac{1-\sqrt{1-s^2}}{s}, && (3.53)\\ g_x &= \frac{1-\sqrt{1-s_x^2}}{s_x}, && (3.54)\\ g_y &= \frac{1-\sqrt{1-s_y^2}}{s_y} = g. && (3.55) \end{aligned}$$

Then the normalized orbital parts of the one-particle wave functions for the DQD are

$$\begin{aligned} \Phi_{L,R}(\boldsymbol{r}) &= \frac{\phi_{L,R}(x,y) - g\phi_{R,L}(x,y)}{\sqrt{1-2sg+g^2}}\phi_{\mathrm{FH}}(z), && (3.56)\\ \Phi_{L,R}^{e,x}(\boldsymbol{r}) &= \frac{\phi_{L,R}^x(x,y) - g_x\phi_{R,L}^x(x,y)}{\sqrt{1-2s_xg_x+g_x^2}}\phi_{\mathrm{FH}}(z), && (3.57)\\ \Phi_{L,R}^{e,y}(\boldsymbol{r}) &= \frac{\phi_{L,R}^y(x,y) - g\phi_{R,L}^y(x,y)}{\sqrt{1-2sg+g^2}}\phi_{\mathrm{FH}}(z). && (3.58) \end{aligned}$$

We note that these six states form an orthonormal set of basis states to a very good accuracy. The only nonzero scalar products among different states are $\langle\Phi_L|\Phi_L^{e,x}\rangle$, $\langle\Phi_R|\Phi_R^{e,x}\rangle$, $\langle\Phi_L|\Phi_R^{e,x}\rangle$, and $\langle\Phi_R|\Phi_L^{e,x}\rangle$. Even though there is a nonzero overlap, the absolute values of these scalar products are small ($\sim$0.01–0.1 depending on the parameters of the DQD), which indicates that Eqs. (3.56–3.58) present a very good approximation for an orthonormal basis. It is, however, important to note that we set $\langle\Phi_L|\Phi_L^{e,x}\rangle$, $\langle\Phi_R|\Phi_R^{e,x}\rangle$, $\langle\Phi_L|\Phi_R^{e,x}\rangle$, and $\langle\Phi_R|\Phi_L^{e,x}\rangle$ equal to zero when calculating the matrix elements of the effective Hamiltonian later on, in order to avoid artefacts from the finite overlap of these basis states.

Given the six basis states for the orbital part of single electrons, we can construct the two-particle wave functions [50, 94]

$$\Psi_{\pm}(\boldsymbol{r}_1, \boldsymbol{r}_2) = \frac{\Phi_L(\boldsymbol{r}_1)\Phi_R(\boldsymbol{r}_2) \pm \Phi_R(\boldsymbol{r}_1)\Phi_L(\boldsymbol{r}_2)}{\sqrt{2}}, \tag{3.59}$$

$$\Psi_{\pm}^{e,\nu}(\boldsymbol{r}_1, \boldsymbol{r}_2) = \frac{\Phi_L^{e,\nu}(\boldsymbol{r}_1)\Phi_R(\boldsymbol{r}_2) \pm \Phi_R(\boldsymbol{r}_1)\Phi_L^{e,\nu}(\boldsymbol{r}_2)}{\sqrt{2}}, \tag{3.60}$$

$$\Psi_{L,R}(\boldsymbol{r}_1, \boldsymbol{r}_2) = \Phi_{L,R}(\boldsymbol{r}_1)\Phi_{L,R}(\boldsymbol{r}_2), \tag{3.61}$$

where $\nu \in \{x, y\}$. The calculations for Fig. 3.6 were done with the orbital excitation along the x axis only, $\Psi_{\pm}^{e} = \Psi_{\pm}^{e,x}$, because the rates resulting from $\Psi_{\pm}^{e,y}$ are much smaller than those from $\Psi_{\pm}^{e,x}$ in this setup. For some special configurations, such as $\boldsymbol{B} \parallel y$ and $x \parallel [110]$, where $\boldsymbol{B}$ is the external magnetic field, the calculations for $\Psi_{\pm}^{e} = \Psi_{\pm}^{e,y}$ lead to lifetimes similar to or even shorter than those for $\Psi_{\pm}^{e} = \Psi_{\pm}^{e,x}$, and so states with the excitation along the y axis should be taken into account in these special cases. States of type $(1, 1^*)$ with the excited electron in the right QD will change the results only by factors around 2, and therefore were not included for simplicity.

3.B Hamiltonian

The Hamiltonian of the considered system is

$$\begin{aligned} H &= \sum_{j=1,2} \left(H_0^{(j)} + H_Z^{(j)} + H_{\mathrm{SOI}}^{(j)} + H_{\mathrm{hyp}}^{(j)} + H_{\mathrm{el-ph}}^{(j)} \right) \\ &\quad + H_C + H_{\mathrm{ph}}, \end{aligned} \tag{3.62}$$

where the index j denotes the electron, H_0 takes into account the motion of the electron in the double dot potential, H_Z is the Zeeman term, H_{SOI} is the spin-orbit interaction (SOI), H_{hyp} is the hyperfine coupling, $H_{\mathrm{el-ph}}$ is the electron-phonon interaction, H_C is the Coulomb repulsion, and H_{ph} is the Hamiltonian of the phonon bath. Below, we discuss the contributions to H in further detail.

Hamiltonian H_0

Due to $a_z \ll l_c$, the wave function along the z axis is the same for all basis states in our model. The one-particle Hamiltonian H_0 can therefore be written as an effective 2D Hamiltonian

$$H_0 = \frac{p_x^2 + p_y^2}{2m_{\text{eff}}} + V(x,y), \tag{3.63}$$

where p_x (p_y) is the momentum along the x (y) axis and $V(x,y)$ is the confining potential in the transverse directions. The potential $V(x,y)$ is provided by the electric gates and features a finite barrier between the two QDs. It also accounts for electric fields applied along the DQD axis that effectively shift the electron energy in the left QD by the detuning ϵ compared to the right QD.

Coulomb repulsion

The Hamiltonian that describes the Coulomb interaction between the two electrons is

$$H_C = \frac{1}{4\pi\epsilon_0\epsilon_r}\frac{e^2}{|\boldsymbol{r}_1 - \boldsymbol{r}_2|}, \tag{3.64}$$

where e is the elementary positive charge, ϵ_0 is the vacuum permittivity, and ϵ_r is the relative permittivity of GaAs.

Zeeman term

We consider an in-plane magnetic field $\boldsymbol{B} = |\boldsymbol{B}|\boldsymbol{e_B} = B\boldsymbol{e_B}$ with arbitrary orientation in the x-y plane. Here and in the following, $\boldsymbol{e_k}$ ($\boldsymbol{e}_\eta$) stands for the unit vector along the direction of some vector $\boldsymbol{k}$ (axis η). As the 2DEG is only a few nanometers wide, orbital effects due to an in-plane magnetic field are negligible. The Hamiltonian for the Zeeman coupling reads

$$H_Z = \frac{E_Z}{2}\sigma_B, \tag{3.65}$$

where $E_Z = g\mu_B B$ is the Zeeman energy, g is the in-plane g factor, μ_B is the Bohr magneton, $B = |\boldsymbol{B}|$ is the magnetic field strength, and

$$\sigma_B = \boldsymbol{\sigma}\cdot\boldsymbol{e_B}, \tag{3.66}$$

with $\boldsymbol{\sigma}$ as the vector of Pauli matrices, denotes the Pauli operator for the electron spin along the magnetic field.

Spin-orbit interaction

We assume that the heterostructure was grown along the [001] direction, referred to as both the z and z' direction. Consequently, the SOI due to Rashba and Dresselhaus SOI reads

$$H_{\mathrm{SOI}} = \alpha\left(p_{x'}\sigma_{y'} - p_{y'}\sigma_{x'}\right) + \beta\left(p_{y'}\sigma_{y'} - p_{x'}\sigma_{x'}\right) \tag{3.67}$$

for a single electron, where the axes x' and y' correspond to the main crystallographic axes [100] and [010], respectively.

Using the antihermitian operator

$$S_1 = i\frac{m_{\mathrm{eff}}}{\hbar}\left[\alpha\left(x'\sigma_{y'} - y'\sigma_{x'}\right) + \beta\left(y'\sigma_{y'} - x'\sigma_{x'}\right)\right], \tag{3.68}$$

which fulfills the commutation relation

$$[S_1, H_0] = S_1 H_0 - H_0 S_1 = -H_{\mathrm{SOI}}, \tag{3.69}$$

we can remove the SOI to lowest order via a unitary (Schrieffer-Wolff) transformation [12, 85, 86, 87, 88, 89, 90],

$$\begin{aligned}\widetilde{H} &= e^{S} H e^{-S} = e^{\left(\sum_j S_1^{(j)} + \dots\right)} H e^{-\left(\sum_j S_1^{(j)} + \dots\right)} \\ &\simeq \sum_{j=1,2}\left(H_0^{(j)} + H_Z^{(j)} + H_{\mathrm{hyp}}^{(j)} + H_{\mathrm{el-ph}}^{(j)}\right) + H_C + H_{\mathrm{ph}} \\ &\quad + \sum_{j=1,2}\left([S_1^{(j)}, H_Z^{(j)}] + \frac{1}{2}[S_1^{(j)}, H_{\mathrm{SOI}}^{(j)}]\right).\end{aligned} \tag{3.70}$$

The perturbation theory applies when both the SOI and the Zeeman coupling are weak compared to the confinement (spin-orbit length $\gg$ confinement length; Zeeman splitting $\ll$ orbital level splitting), which is well fulfilled in the system under study. Exploiting the commutation relations $[\sigma_{x'}, \sigma_{y'}] = 2i\sigma_{z'}$ (and analogously for cyclic permutations) of the Pauli matrices, one finds

$$[S_1, H_Z] = g\mu_B\left(\boldsymbol{r}_{\mathrm{SOI}} \times \boldsymbol{B}\right) \cdot \boldsymbol{\sigma}, \tag{3.71}$$

where we defined the SOI-dependent vector operator

$$\boldsymbol{r}_{\mathrm{SOI}} = \left(\frac{y'}{l_R} + \frac{x'}{l_D}\right)\boldsymbol{e}_{[100]} + \left(-\frac{x'}{l_R} - \frac{y'}{l_D}\right)\boldsymbol{e}_{[010]}. \tag{3.72}$$

The unit vector along the $[100]$ axis, i.e., the x' direction, is denoted by $\boldsymbol{e}_{[100]} = \boldsymbol{e}_{x'}$, and analogously for all other crystallographic directions. The spin-orbit lengths l_R and l_D are defined as

$$l_R = \frac{\hbar}{m_{\text{eff}}\alpha}, \tag{3.73}$$

$$l_D = \frac{\hbar}{m_{\text{eff}}\beta}. \tag{3.74}$$

The contribution due to $[S_1, H_{\text{SOI}}]/2$ is less important when B is sufficiently large, and considering $B \sim 0.7$ T [7, 40] we therefore omit it in our model. Nevertheless, we provide the result for completeness [87],

$$\begin{aligned}\frac{1}{2}[S_1, H_{\text{SOI}}] &= -m_{\text{eff}}\left(\alpha^2+\beta^2\right) \\ &\quad +\frac{m_{\text{eff}}}{\hbar}\left(\beta^2-\alpha^2\right) l_{z'}\sigma_{z'}.\end{aligned} \tag{3.75}$$

Here the operator $l_{z'} = (x'p_{y'} - y'p_{x'})$ corresponds to the angular momentum along the axis of strong confinement. Again, orbital effects (canonical momentum $\neq$ kinetic momentum) are negligible when the magnetic field is applied in-plane.

Finally, we mention that corrections of type $[S_1, H_{\text{hyp}}]$ were neglected in Eq. (3.70), because H_Z is assumed to be much larger than the hyperfine coupling H_{hyp} that we discuss next.

Hyperfine interaction

The hyperfine interaction between the electron and the nuclear spins can be described in terms of an effective magnetic field. The latter can be split into a sum field, which is present in both QDs, and a gradient field, which accounts for the difference in the hyperfine field between the dots. As the sum field is usually small compared to the external magnetic field, and, moreover, may largely be accounted for by H_Z, we use H_{hyp} to quantify the gradient field between the dots. Hence, this Hamiltonian reads

$$H_{\text{hyp}} = \frac{\boldsymbol{\delta b}\cdot\boldsymbol{\sigma}}{4}\left(\mathcal{P}_L - \mathcal{P}_R\right), \tag{3.76}$$

where $\boldsymbol{\delta b}$ arises from the hyperfine field gradient between the QDs. The operators $\mathcal{P}_L$ and $\mathcal{P}_R$ are projectors for the left and right QD, respectively, and can be written as

$$\mathcal{P}_L = |\Phi_L\rangle\langle\Phi_L| + |\Phi_L^{e,x}\rangle\langle\Phi_L^{e,x}| + |\Phi_L^{e,y}\rangle\langle\Phi_L^{e,y}|, \tag{3.77}$$

$$\mathcal{P}_R = |\Phi_R\rangle\langle\Phi_R| + |\Phi_R^{e,x}\rangle\langle\Phi_R^{e,x}| + |\Phi_R^{e,y}\rangle\langle\Phi_R^{e,y}|, \tag{3.78}$$

for the basis states defined in Appendix 3.A.

We note that

$$\langle(1,1)S|H_{\mathrm{hyp}}|(1,1)T_0\rangle = \frac{\delta b_B}{2}, \tag{3.79}$$

where

$$\delta b_B = \boldsymbol{\delta b} \cdot \boldsymbol{e_B} \tag{3.80}$$

is the component of $\boldsymbol{\delta b}$ along the external magnetic field $\boldsymbol{B}$. Because it turns out that all other matrix elements of H_{hyp} within the basis of Appendix 3.A are negligible for the lifetimes of the qubit, we approximate the hyperfine coupling by

$$H_{\mathrm{hyp}} \simeq \frac{\delta b_B}{2}|(1,1)S\rangle\langle(1,1)T_0| + \mathrm{h.c.}, \tag{3.81}$$

with the hermitian conjugate abbreviated as "h.c.". We set $\delta b_B = -0.14\ \mu\mathrm{eV}$ in our calculations, in good agreement with Refs. [7, 10].

Electron-phonon coupling

The electron-phonon interaction

$$H_{\mathrm{el-ph}} = H_{\mathrm{dp}} + H_{\mathrm{pe}} \tag{3.82}$$

comprises the deformation potential coupling H_{dp} and the piezoelectric coupling H_{pe}. Both mechanisms can be derived from the displacement operator, which we therefore recall first. Most of the information summarized in this appendix on electron-phonon coupling is described in great detail in Refs. [97, 98, 101, 120, 121, 122, 123], and we refer to these for further information.

Displacement operator

Acoustic phonons in an isotropic crystal (bulk) lead to the displacement operator

$$\boldsymbol{u} = \sum_{\boldsymbol{q},s} \boldsymbol{e}_{\boldsymbol{q}s} \left(c_{\boldsymbol{q}s} e^{i\boldsymbol{q}\cdot\boldsymbol{r}} a_{\boldsymbol{q}s} + c^*_{\boldsymbol{q}s} e^{-i\boldsymbol{q}\cdot\boldsymbol{r}} a^\dagger_{\boldsymbol{q}s} \right), \tag{3.83}$$

where $c_{\boldsymbol{q}s}$ is an arbitrary coefficient with normalization condition $|c_{\boldsymbol{q}s}|^2 = \hbar/(2\rho V \omega_{\boldsymbol{q}s})$, ρ and V are the density and volume of the crystal, and $\omega_{\boldsymbol{q}s}$ is the angular frequency of the acoustic phonon of type s with wave vector $\boldsymbol{q}$. For the longitudinal mode $s = l$, the dispersion relation at small $q = |\boldsymbol{q}|$

is $\omega_{\boldsymbol{q}l} = q\sqrt{(\lambda+2\mu)/\rho} = qv_l$, while for the transverse modes $s = t_1$ and $s = t_2$ one finds $\omega_{\boldsymbol{q}t_1} = \omega_{\boldsymbol{q}t_2} = \omega_{\boldsymbol{q}t} = q\sqrt{\mu/\rho} = qv_t$, where λ and μ are the Lamé parameters of the material and v_l (v_t) is the speed of sound for longitudinal (transverse) waves [97]. The operators $a^\dagger_{\boldsymbol{q}s}$ and $a_{\boldsymbol{q}s}$ create and annihilate a corresponding phonon, and fulfill the commutation relations $[a^\dagger_{\boldsymbol{q}s}, a^\dagger_{\boldsymbol{q}'s'}] = 0$, $[a_{\boldsymbol{q}s}, a_{\boldsymbol{q}'s'}] = 0$, and $[a_{\boldsymbol{q}s}, a^\dagger_{\boldsymbol{q}'s'}] = \delta_{\boldsymbol{q},\boldsymbol{q}'}\delta_{s,s'}$, with $\delta_{\boldsymbol{q},\boldsymbol{q}'}$ and $\delta_{s,s'}$ as Kronecker deltas. For each wave vector $\boldsymbol{q}$, the three real-valued polarization vectors $\boldsymbol{e}_{\boldsymbol{q}s}$ form an orthonormal basis with $\boldsymbol{e}_{\boldsymbol{q}l} \parallel \boldsymbol{q}$. The summation over $\boldsymbol{q}$ runs over all wave vectors within the first Brillouin zone.

With a suitable choice of the polarization vectors $\boldsymbol{e}_{\boldsymbol{q}s}$, the displacement operator from Eq. (3.83) can be simplified further. We choose these vectors in such a way that the relations

$$\begin{aligned} \boldsymbol{e}_{-\boldsymbol{q}l} &= -\boldsymbol{e}_{\boldsymbol{q}l}, && (3.84) \\ \boldsymbol{e}_{-\boldsymbol{q}t_1} &= -\boldsymbol{e}_{\boldsymbol{q}t_1}, && (3.85) \\ \boldsymbol{e}_{-\boldsymbol{q}t_2} &= \boldsymbol{e}_{\boldsymbol{q}t_2}, && (3.86) \end{aligned}$$

are fulfilled. The advantages of this definition become obvious later on, when we write down the Hamiltonian for the electron-phonon coupling. In short terms, this choice allows one to define $\boldsymbol{e}_{\boldsymbol{q}l} = \boldsymbol{q}/q$ and to represent the vectors $\boldsymbol{e}_{\boldsymbol{q}s}$ via a simple right-handed basis. Setting $c_{\boldsymbol{q}s} = \sqrt{\hbar/(2\rho V\omega_{\boldsymbol{q}s})}$, and making use of Eqs. (3.84) to (3.86) and of the property $\omega_{-\boldsymbol{q}s} = \omega_{\boldsymbol{q}s}$, the displacement operator can be written in the convenient form

$$\boldsymbol{u} = \sum_{\boldsymbol{q},s} \sqrt{\frac{\hbar}{2\rho V\omega_{\boldsymbol{q}s}}}\boldsymbol{e}_{\boldsymbol{q}s}\left(a_{\boldsymbol{q}s} \mp_s a^\dagger_{-\boldsymbol{q}s}\right)e^{i\boldsymbol{q}\cdot\boldsymbol{r}}, \tag{3.87}$$

where

$$\mp_s = \begin{cases} - & \text{for } s = l, t_1, \\ + & \text{for } s = t_2. \end{cases} \tag{3.88}$$

This representation of the displacement operator, Eq. (3.87), will now be used to derive the Hamiltonian for the electron-phonon coupling. We note that the time dependence $\boldsymbol{u} \to \boldsymbol{u}(\tau)$ and $H_{\text{el-ph}} \to H_{\text{el-ph}}(\tau)$ in the interaction picture (see Appendix 3.E) is simply obtained via $a_{\boldsymbol{q}s} \to a_{\boldsymbol{q}s}(\tau) = a_{\boldsymbol{q}s}e^{-i\omega_{\boldsymbol{q}s}\tau}$ and $a^\dagger_{\boldsymbol{q}s} \to a^\dagger_{\boldsymbol{q}s}(\tau) = a^\dagger_{\boldsymbol{q}s}e^{i\omega_{\boldsymbol{q}s}\tau}$.

It is worth mentioning how we choose the values for the speeds of sound in GaAs. The three elastic stiffness coefficients for GaAs are $c_{11} = 118$, $c_{12} = 53.5$, and $c_{44} = 59.4$, each in units of 10^9 N/m^2. These values were taken from Ref. [97] and are in very good agreement with those in, e.g., Refs. [98, 99]. It makes sense to approximate these coefficients by $\tilde{c}_{11}$, $\tilde{c}_{12}$, and $\tilde{c}_{44}$, respectively, for which the condition $\tilde{c}_{11} = \tilde{c}_{12} + 2\tilde{c}_{44}$ of an isotropic material is fulfilled. By postulating that the relative deviation for each of the three constants should be the same, we find $\lambda = \tilde{c}_{12} = 43.5 \times 10^9\,\mathrm{N/m}^2$ and $\mu = \tilde{c}_{44} = 48.3 \times 10^9\,\mathrm{N/m}^2$, corresponding to a relative deviation of 18.7%. The resulting sound velocities in the isotropic approximation are $v_l = \sqrt{\tilde{c}_{11}/\rho} = 5.1 \times 10^3\,\mathrm{m/s}$ and $v_t = \sqrt{\tilde{c}_{44}/\rho} = 3.0 \times 10^3\,\mathrm{m/s}$. We note that basically the same values are obtained by simply averaging over the speeds of sound along the [100], [110], and [111] directions (longitudinal or transverse waves, respectively), as listed, for instance, in Refs. [98, 99].

Deformation potential coupling

The first coupling mechanism is the deformation potential coupling. In the presence of strain, the energy of the conduction band changes. For GaAs, a cubic semiconductor with the conduction band minimum at the Γ point, the shift of the conduction band edge is determined by the simple Hamiltonian

$$H_{\mathrm{dp}} = \Xi \nabla \cdot \boldsymbol{u} = \Xi(\epsilon_{xx} + \epsilon_{yy} + \epsilon_{zz}), \tag{3.89}$$

where Ξ is the hydrostatic deformation potential, ∇ is the Nabla operator, and ϵ_{ij} are the strain tensor elements, which are related to the displacement via

$$\epsilon_{ij} = \frac{1}{2}\left(\frac{\partial u_i}{\partial x_j} + \frac{\partial u_j}{\partial x_i}\right). \tag{3.90}$$

The trace of the strain tensor, $\nabla \cdot \boldsymbol{u} = \epsilon_{xx} + \epsilon_{yy} + \epsilon_{zz}$, corresponds to the relative change in the volume. One finds $\Xi \approx -8$ eV for GaAs [101, 102], and so compression increases the energy of the conduction band edge. Exploiting $\nabla e^{i\boldsymbol{q}\cdot\boldsymbol{r}} = i\boldsymbol{q}e^{i\boldsymbol{q}\cdot\boldsymbol{r}}$ and defining $\boldsymbol{e}_{\boldsymbol{q}l} = \boldsymbol{q}/q$, substitution of Eq. (3.87) into (3.89) yields

$$H_{\mathrm{dp}} = i\Xi \sum_{\boldsymbol{q}} \sqrt{\frac{\hbar}{2\rho V \omega_{\boldsymbol{q}l}}}\, q \left(a_{\boldsymbol{q}l} - a^{\dagger}_{-\boldsymbol{q}l}\right) e^{i\boldsymbol{q}\cdot\boldsymbol{r}}. \tag{3.91}$$

We note that only the longitudinal mode contributes to the deformation potential coupling. This is different for the piezoelectric electron-phonon interaction that we derive next.

Piezoelectric coupling

In crystals without inversion symmetry, lattice vibrations (i.e., phonons) result in a finite polarization density $\boldsymbol{P}_p^{\text{phon}}$ and, consequently, lead to an effective electric field $\boldsymbol{E}_p$. The latter is characterized by the equation

$$0 = \epsilon_0 \boldsymbol{E}_p + \boldsymbol{P}_p^{\text{diel}} + \boldsymbol{P}_p^{\text{phon}} = \epsilon_0 \epsilon_r \boldsymbol{E}_p + \boldsymbol{P}_p^{\text{phon}}, \tag{3.92}$$

where we set the electric displacement on the left-hand side to zero due to the absence of free charges in this mechanism. The vector $\boldsymbol{P}_p^{\text{diel}} = \epsilon_0(\epsilon_r - 1)\boldsymbol{E}_p$ is the polarization density induced by the field $\boldsymbol{E}_p$, ϵ_0 is the vacuum permittivity, and ϵ_r is the relative permittivity of the material ($\epsilon_r \simeq 13$ in GaAs). In contrast to $\boldsymbol{P}_p^{\text{diel}}$, the term $\boldsymbol{P}_p^{\text{phon}}$ results directly from the strain that is caused by the lattice vibrations. The polarization density $\boldsymbol{P}_p^{\text{phon}}$ is related to the strain tensor elements via

$$P_{p,i}^{\text{phon}} = \sum_{j,k} h_{ijk} \epsilon_{jk}, \tag{3.93}$$

where the h_{ijk} are the elements of the third-rank piezoelectric tensor. In zinc blende structures such as GaAs, the h_{ijk} take on a rather simple form,

$$h_{ijk} = h_{14}|\epsilon_{ijk}| = \begin{cases} h_{14} & \text{for } |\epsilon_{ijk}| = 1, \\ 0 & \text{for } |\epsilon_{ijk}| = 0. \end{cases} \tag{3.94}$$

Here ϵ_{ijk} is the Levi-Civita symbol, and the x_i, x_j, and x_k related to the indices i, j, and k, respectively, correspond to the main crystallographic axes.

We now proceed to calculate the electric field $\boldsymbol{E}_p$ via the relation [122]

$$\boldsymbol{E}_p = -\frac{\boldsymbol{P}_p^{\text{phon}}}{\epsilon_0 \epsilon_r}, \tag{3.95}$$

which results directly from Eq. (3.92). In order to improve readability, we use a short-hand notation in the remainder of this subsection for convenience: x, y, and z correspond to the coordinates along the main crystallographic axes, with $\boldsymbol{e}_x$, $\boldsymbol{e}_y$, and $\boldsymbol{e}_z$ as the unit vectors along the $[100]$, $[010]$, and $[001]$ directions, respectively. Substitution of Eqs. (3.87), (3.90), (3.93), and (3.94) into Eq. (3.95) yields

$$\begin{aligned} \boldsymbol{E}_p &= -\frac{i h_{14}}{\epsilon_0 \epsilon_r} \sum_{\boldsymbol{q},s} \begin{pmatrix} q_y e_{\boldsymbol{q}s}^z + q_z e_{\boldsymbol{q}s}^y \\ q_z e_{\boldsymbol{q}s}^x + q_x e_{\boldsymbol{q}s}^z \\ q_x e_{\boldsymbol{q}s}^y + q_y e_{\boldsymbol{q}s}^x \end{pmatrix} \\ &\quad \times \sqrt{\frac{\hbar}{2\rho V \omega_{\boldsymbol{q}s}}} \left(a_{\boldsymbol{q}s} \mp_s a_{-\boldsymbol{q}s}^\dagger \right) e^{i\boldsymbol{q}\cdot\boldsymbol{r}}, \end{aligned} \tag{3.96}$$

where

$$\begin{aligned} \boldsymbol{q} &= q_x \boldsymbol{e}_x + q_y \boldsymbol{e}_y + q_z \boldsymbol{e}_z, && (3.97) \\ \boldsymbol{e}_{\boldsymbol{q}s} &= e^x_{\boldsymbol{q}s} \boldsymbol{e}_x + e^y_{\boldsymbol{q}s} \boldsymbol{e}_y + e^z_{\boldsymbol{q}s} \boldsymbol{e}_z, && (3.98) \end{aligned}$$

and the three components of the vector refer to the basis $\{\boldsymbol{e}_x, \boldsymbol{e}_y, \boldsymbol{e}_z\}$. The phonon-induced electric field $\boldsymbol{E}_p$ can be split into two parts,

$$\boldsymbol{E}_p = \boldsymbol{E}_p^{\|} + \boldsymbol{E}_p^{\perp}, \tag{3.99}$$

where the "longitudinal" part

$$\begin{aligned} \boldsymbol{E}_p^{\|} = -\frac{ih_{14}}{\epsilon_0 \epsilon_r} \sum_{\boldsymbol{q},s} & \frac{2\left(q_x q_y e^z_{\boldsymbol{q}s} + q_y q_z e^x_{\boldsymbol{q}s} + q_z q_x e^y_{\boldsymbol{q}s}\right)}{q^2} \boldsymbol{q} \\ \times & \sqrt{\frac{\hbar}{2\rho V \omega_{\boldsymbol{q}s}}} \left(a_{\boldsymbol{q}s} \mp_s a^\dagger_{-\boldsymbol{q}s}\right) e^{i\boldsymbol{q}\cdot\boldsymbol{r}} \end{aligned} \tag{3.100}$$

contains the contributions parallel to $\boldsymbol{q}$ for each mode, while the "transverse" part $\boldsymbol{E}_p^{\perp} = \boldsymbol{E}_p - \boldsymbol{E}_p^{\|}$ comprises the remaining components perpendicular to $\boldsymbol{q}$. The longitudinal and transverse parts fulfill

$$\begin{aligned} \nabla \times \boldsymbol{E}_p^{\|} &= 0, && (3.101) \\ \nabla \cdot \boldsymbol{E}_p^{\perp} &= 0, && (3.102) \end{aligned}$$

respectively. As a consequence, one can write $\boldsymbol{E}_p^{\|}$ as the gradient of a scalar potential Φ_p, and $\boldsymbol{E}_p^{\perp}$ as the curl of a vector potential $\boldsymbol{A}_p$,

$$\begin{aligned} \boldsymbol{E}_p^{\|} &= -\nabla \Phi_p, && (3.103) \\ \boldsymbol{E}_p^{\perp} &= \nabla \times \boldsymbol{A}_p. && (3.104) \end{aligned}$$

From Eqs. (3.100) and (3.103), one finds

$$\Phi_p = \frac{h_{14}}{\epsilon_0 \epsilon_r} \sum_{\boldsymbol{q},s} f_{\boldsymbol{q}s} \sqrt{\frac{\hbar}{2\rho V \omega_{\boldsymbol{q}s}}} \left(a_{\boldsymbol{q}s} \mp_s a^\dagger_{-\boldsymbol{q}s}\right) e^{i\boldsymbol{q}\cdot\boldsymbol{r}} \tag{3.105}$$

for the scalar potential, where we introduced

$$f_{\boldsymbol{q}s} = \frac{2\left(q_x q_y e^z_{\boldsymbol{q}s} + q_y q_z e^x_{\boldsymbol{q}s} + q_z q_x e^y_{\boldsymbol{q}s}\right)}{q^2}. \tag{3.106}$$

The vector potential $\boldsymbol{A}_p$ and, hence, the transverse part $\boldsymbol{E}_p^\perp$ are usually omitted for the piezoelectric electron-phonon interaction. Reasons for this omission may be inferred from Maxwell's equations.

In accordance with common practice, we neglect the vector potential $\boldsymbol{A}_p$ in the following and consider only the scalar potential Φ_p. Using an explicit representation for the unit vectors $\boldsymbol{e}_{\boldsymbol{q}s}$, the result from Eq. (3.105) can be simplified further. We choose

$$\boldsymbol{e}_{\boldsymbol{q}l} = \frac{\boldsymbol{q}}{q} = \begin{pmatrix} \cos\phi_{\boldsymbol{q}} \sin\theta_{\boldsymbol{q}} \\ \sin\phi_{\boldsymbol{q}} \sin\theta_{\boldsymbol{q}} \\ \cos\theta_{\boldsymbol{q}} \end{pmatrix}, \tag{3.107}$$

$$\boldsymbol{e}_{\boldsymbol{q}t_1} = \begin{pmatrix} \sin\phi_{\boldsymbol{q}} \\ -\cos\phi_{\boldsymbol{q}} \\ 0 \end{pmatrix}, \tag{3.108}$$

$$\boldsymbol{e}_{\boldsymbol{q}t_2} = \begin{pmatrix} \cos\phi_{\boldsymbol{q}} \cos\theta_{\boldsymbol{q}} \\ \sin\phi_{\boldsymbol{q}} \cos\theta_{\boldsymbol{q}} \\ -\sin\theta_{\boldsymbol{q}} \end{pmatrix}, \tag{3.109}$$

in agreement with Eqs. (3.84) to (3.86), where $0 \leq \phi_{\boldsymbol{q}} < 2\pi$ is the azimuthal angle and $0 \leq \theta_{\boldsymbol{q}} < \pi$ is the polar angle of $\boldsymbol{q}$ in spherical coordinates. Again, the vector components in Eqs. (3.107) to (3.109) refer to the basis $\{\boldsymbol{e}_x, \boldsymbol{e}_y, \boldsymbol{e}_z\}$, i.e., to the unit vectors for the main crystallographic directions (note the special definition of x, y, and z in this subsection). Also, we note that the $\{\boldsymbol{e}_{\boldsymbol{q}l}, \boldsymbol{e}_{\boldsymbol{q}t_1}, \boldsymbol{e}_{\boldsymbol{q}t_2}\}$ defined above form a right-handed, orthonormal set of basis vectors for any $\boldsymbol{q}$. With this convenient representation, which is similar to the one chosen in Ref. [123], the expression $f_{\boldsymbol{q}s}$ from Eq. (3.106) simplifies to

$$f_{\boldsymbol{q}l} = 3\cos\theta_{\boldsymbol{q}} \sin^2\theta_{\boldsymbol{q}} \sin(2\phi_{\boldsymbol{q}}), \tag{3.110}$$

$$f_{\boldsymbol{q}t_1} = -\sin(2\theta_{\boldsymbol{q}}) \cos(2\phi_{\boldsymbol{q}}), \tag{3.111}$$

$$f_{\boldsymbol{q}t_2} = -\left(3\sin^2\theta_{\boldsymbol{q}} - 2\right) \sin\theta_{\boldsymbol{q}} \sin(2\phi_{\boldsymbol{q}}), \tag{3.112}$$

where we mention that trigonometric identities allow one to rewrite the above relations in many different ways.

Finally, the potential energy of an electron in the phonon-induced electric field, i.e., the Hamiltonian for the piezoelectric electron-phonon coupling, corresponds to

$$H_{\mathrm{pe}} = -e\Phi_p, \tag{3.113}$$

where $-e$ is the charge of the electron.

Phonon bath

The Hamiltonian for the phonon bath is

$$H_{\mathrm{ph}} = \sum_{\boldsymbol{q},s} \hbar\omega_{\boldsymbol{q}s} \left(a^{\dagger}_{\boldsymbol{q}s} a_{\boldsymbol{q}s} + \frac{1}{2} \right) , \tag{3.114}$$

where the sum runs again over all modes s and all wave vectors $\boldsymbol{q}$ within the first Brillouin zone.

3.C Model Hamiltonian at small detuning

As described in detail in the main text, we study the lifetimes of the singlet-triplet qubit at both small and large detuning ϵ. In this appendix, we explain the details of our model at small detunings, $\epsilon \simeq 0$.

Exchange energy and orbital level spacing

In the unbiased DQD, the energy of $|(0,2)S\rangle$ and $|(2,0)S\rangle$ is much larger than that of $(1^*,1)$-type states with an excited orbital part. This allows us to calculate the lifetimes with an 8×8 matrix [see Eq. (3.121)] that is based on states of type $(1,1)$ and $(1^*,1)$ only. Even though $|(0,2)S\rangle$ and $|(2,0)S\rangle$ are not part of the basis, their presence can be accounted for as described below.

Considering the basis states introduced in Appendix 3.A and shifting the energy globally by $\langle(1,1)T_0|\big(H_0^{(1)} + H_0^{(2)} + H_C\big)|(1,1)T_0\rangle$, the Hamiltonian $H_0^{(1)} + H_0^{(2)} + H_C$ can be approximated via

$$\begin{aligned} H_0^{(1)} + H_0^{(2)} + H_C \;\approx\; & -J_S|(1,1)S\rangle\langle(1,1)S| \\ & +\Delta E \left(|\Psi^e_+\rangle\langle\Psi^e_+| + |\Psi^e_-\rangle\langle\Psi^e_-| \right) , \end{aligned} \tag{3.115}$$

where the exchange energy J_S results from admixtures with $|(0,2)S\rangle$ and $|(2,0)S\rangle$. The energy gap $\Delta E \simeq \hbar\omega_0$ is well described by the level spacing $\hbar\omega_0$ in the left QD and corresponds to the energy difference between the four states of lowest energy in the DQD and the states with excited orbital part.

We note that J_S can be estimated [50, 94, 119] by projecting $H_0^{(1)} + H_0^{(2)} + H_C$ onto the subspace $\{|(2,0)S\rangle, |(0,2)S\rangle, |(1,1)S\rangle\}$ through a projector $\mathcal{P}_{S3}$, which yields the Hamiltonian

$$H_{S3} = \mathcal{P}_{S3} \left(H_0^{(1)} + H_0^{(2)} + H_C \right) \mathcal{P}_{S3} \tag{3.116}$$

with matrix representation

$$H_{S3} = \begin{pmatrix} U - V_- & 0 & -\sqrt{2}t \\ 0 & U - V_- & -\sqrt{2}t \\ -\sqrt{2}t & -\sqrt{2}t & V_+ - V_- \end{pmatrix}. \tag{3.117}$$

Here

$$t = -\langle \Phi_L | H_0 | \Phi_R \rangle - \frac{1}{\sqrt{2}} \langle \Psi_+ | H_C | \Psi_R \rangle \tag{3.118}$$

is the hopping amplitude (also referred to as the tunnel coupling), $U = \langle \Psi_R | H_C | \Psi_R \rangle$ is the on-site repulsion, $V_\pm = \langle \Psi_\pm | H_C | \Psi_\pm \rangle$, and the energy was globally shifted as mentioned before. Diagonalization of H_{S3} results in

$$\begin{aligned} \widetilde{H}_{S3} &= U_{S3}^\dagger H_{S3} U_{S3} \\ &= \begin{pmatrix} U - 2V_- + V_+ + J_S & 0 & 0 \\ 0 & U - V_- & 0 \\ 0 & 0 & -J_S \end{pmatrix}, \end{aligned} \tag{3.119}$$

where U_{S3} is the matrix for the unitary transformation and

$$J_S = \frac{1}{2} \left(\sqrt{16t^2 + (U - V_+)^2} - U - V_+ + 2V_- \right) \tag{3.120}$$

is the resulting exchange splitting between $|(1,1)S\rangle$ and $|(1,1)T_0\rangle$. Considering $\epsilon \simeq 0$, the formulas for J_S and U_{S3} from this estimate allow us to account for admixtures of $|(2,0)S\rangle$ and $|(0,2)S\rangle$ to the qubit state of type $|(1,1)S\rangle$ and, consequently, to study the effects of these admixtures on the phonon-induced lifetimes of the qubit.

Matrix representation

We analyze the qubit lifetimes in an unbiased DQD by projecting the Hamiltonian $\widetilde{H}$, Eq. (3.70), onto the basis $\{|(1,1)S\rangle$, $|(1,1)T_0\rangle$, $|(1,1)T_+\rangle$, $|(1,1)T_-\rangle$, $|(1^*,1)S\rangle$, $|(1^*,1)T_+\rangle$, $|(1^*,1)T_0\rangle$, $|(1^*,1)T_-\rangle\}$. The basis states are described in detail in Appendix 3.A, and the projection yields

$$\widetilde{H} = \begin{pmatrix} -J_S + P_{SS} & \frac{\delta b_B}{2} & \frac{\Omega}{\sqrt{2}} & -\frac{\Omega}{\sqrt{2}} & P^{e}_{cr} & \frac{\Omega_1}{\sqrt{2}} & 0 & -\frac{\Omega_1}{\sqrt{2}} \\ \frac{\delta b_B}{2} & P_T & 0 & 0 & 0 & -\frac{\Omega_1}{\sqrt{2}} & P^{e}_{cr} & -\frac{\Omega_1}{\sqrt{2}} \\ \frac{\Omega}{\sqrt{2}} & 0 & E_Z + P_T & 0 & \frac{\Omega_1}{\sqrt{2}} & P^{e}_{cr} & -\frac{\Omega_1}{\sqrt{2}} & 0 \\ -\frac{\Omega}{\sqrt{2}} & 0 & 0 & -E_Z + P_T & -\frac{\Omega_1}{\sqrt{2}} & 0 & -\frac{\Omega_1}{\sqrt{2}} & P^{e}_{cr} \\ P^{e\dagger}_{cr} & 0 & \frac{\Omega_1}{\sqrt{2}} & -\frac{\Omega_1}{\sqrt{2}} & \Delta E + P^{e} & \frac{\Omega_2}{\sqrt{2}} & 0 & -\frac{\Omega_2}{\sqrt{2}} \\ \frac{\Omega_1}{\sqrt{2}} & -\frac{\Omega_1}{\sqrt{2}} & P^{e\dagger}_{cr} & 0 & \frac{\Omega_2}{\sqrt{2}} & \Delta E + E_Z + P^{e} & -\frac{\Omega_3}{\sqrt{2}} & 0 \\ 0 & P^{e\dagger}_{cr} & -\frac{\Omega_1}{\sqrt{2}} & -\frac{\Omega_1}{\sqrt{2}} & 0 & -\frac{\Omega_3}{\sqrt{2}} & \Delta E + P^{e} & -\frac{\Omega_3}{\sqrt{2}} \\ -\frac{\Omega_1}{\sqrt{2}} & -\frac{\Omega_1}{\sqrt{2}} & 0 & P^{e\dagger}_{cr} & -\frac{\Omega_2}{\sqrt{2}} & 0 & -\frac{\Omega_3}{\sqrt{2}} & \Delta E - E_Z + P^{e} \end{pmatrix} + H_{\mathrm{ph}}. \tag{3.121}$$

Here the Ω with different indices quantify the matrix elements resulting from the SOI. Defining

$$R_{\mathrm{SOI}} = (\boldsymbol{r}_{\mathrm{SOI}} \times \boldsymbol{e_B})_z, \tag{3.122}$$

one obtains

$$\begin{aligned}
\Omega &= E_Z \left(\langle\Phi_L|R_{\mathrm{SOI}}|\Phi_L\rangle - \langle\Phi_R|R_{\mathrm{SOI}}|\Phi_R\rangle\right), && (3.123)\\
\Omega_1 &= E_Z\langle\Phi_L|R_{\mathrm{SOI}}|\Phi_L^{e,\nu}\rangle, && (3.124)\\
\Omega_2 &= E_Z \left(\langle\Phi_L^{e,\nu}|R_{\mathrm{SOI}}|\Phi_L^{e,\nu}\rangle - \langle\Phi_R|R_{\mathrm{SOI}}|\Phi_R\rangle\right), && (3.125)\\
\Omega_3 &= E_Z \left(\langle\Phi_L^{e,\nu}|R_{\mathrm{SOI}}|\Phi_L^{e,\nu}\rangle + \langle\Phi_R|R_{\mathrm{SOI}}|\Phi_R\rangle\right). && (3.126)
\end{aligned}$$

Analogously, the electron-phonon coupling is denoted by P with different labels,

$$\begin{aligned}
P_T &= \langle\Phi_R|H_{\mathrm{el-ph}}|\Phi_R\rangle + \langle\Phi_L|H_{\mathrm{el-ph}}|\Phi_L\rangle, && (3.127)\\
P^e &= \langle\Phi_L^{e,\nu}|H_{\mathrm{el-ph}}|\Phi_L^{e,\nu}\rangle + \langle\Phi_R|H_{\mathrm{el-ph}}|\Phi_R\rangle, && (3.128)\\
P_{cr}^e &= \langle\Phi_L|H_{\mathrm{el-ph}}|\Phi_L^{e,\nu}\rangle. && (3.129)
\end{aligned}$$

The above expressions for Ω_1, Ω_2, Ω_3, P^e, and P_{cr}^e correspond to $\Psi_\pm^e = \Psi_\pm^{e,\nu}$, for which the orbital excitation is chosen along the axis $\nu \in \{x, y\}$.

In order to account for the finite admixtures from the states $|(0,2)S\rangle$ and $|(2,0)S\rangle$, we set the matrix element $\langle(1,1)S|\big(H_{\mathrm{el-ph}}^{(1)} + H_{\mathrm{el-ph}}^{(2)}\big)|(1,1)S\rangle$ of the electron-phonon interaction to P_{SS}. The latter is a linear combination of P_{SL}, P_{SR}, P_S, and $P_S^\dagger$, where

$$\begin{aligned}
P_{SL} &= 2\langle\Phi_L|H_{\mathrm{el-ph}}|\Phi_L\rangle, && (3.130)\\
P_{SR} &= 2\langle\Phi_R|H_{\mathrm{el-ph}}|\Phi_R\rangle, && (3.131)\\
P_S &= \sqrt{2}\langle\Phi_R|H_{\mathrm{el-ph}}|\Phi_L\rangle. && (3.132)
\end{aligned}$$

The coefficients of the linear combination depend on U, V_+, V_-, and t. We find these coefficients by projecting $H_{\mathrm{el-ph}}^{(1)} + H_{\mathrm{el-ph}}^{(2)}$ onto the subspace $\{|(2,0)S\rangle, |(0,2)S\rangle, |(1,1)S\rangle\}$,

$$\mathcal{P}_{S3}(H_{\mathrm{el-ph}}^{(1)} + H_{\mathrm{el-ph}}^{(2)})\mathcal{P}_{S3} = \begin{pmatrix} P_{SL} & 0 & P_S^\dagger \\ 0 & P_{SR} & P_S \\ P_S & P_S^\dagger & P_T \end{pmatrix}, \tag{3.133}$$

which allows calculation of P_{SS} via

$$P_{SS} = \Big(U_{S3}^\dagger \mathcal{P}_{S3}\big(H_{\mathrm{el-ph}}^{(1)} + H_{\mathrm{el-ph}}^{(2)}\big)\mathcal{P}_{S3}U_{S3}\Big)_{33}. \tag{3.134}$$

For further information on the transformation matrix U_{S3}, see Appendix 3.C.

We note, however, that the above-mentioned contributions from $|(2,0)S\rangle$ and $|(0,2)S\rangle$ to P_{SS} turn out to be negligibly small, because setting $P_{SS} = P_T$ does not affect the lifetimes in our calculations. Furthermore, two-phonon processes based on admixtures from $|(2,0)S\rangle$ and $|(0,2)S\rangle$ are strongly suppressed at $\epsilon \simeq 0$ and can be omitted, as we explain in detail in Appendix 3.H. In conclusion, we find for the parameters in this work that the qubit lifetimes in unbiased DQDs are determined by the basis states with excited orbital parts. The corrections from $|(2,0)S\rangle$ and $|(0,2)S\rangle$ are negligible.

3.D Model Hamiltonian at large detuning

When $|\epsilon| \sim U - V_\pm$ such that the energy gap between the qubit and either $|(2,0)S\rangle$ (negative ϵ) or $|(0,2)S\rangle$ (positive ϵ) is smaller than the orbital level spacing, $0 < U - V_\pm - |\epsilon| < \hbar\omega_0$, the effects of higher orbitals on the lifetimes are negligible. In the regime of large detuning, we therefore project $\widetilde{H}$, Eq. (3.70), onto the basis $\{|(1,1)T_0\rangle$, $|(1,1)S\rangle$, $|(1,1)T_+\rangle$, $|(1,1)T_-\rangle$, $|(0,2)S\rangle$, $|(2,0)S\rangle\}$ and investigate the lifetimes via this 6×6 matrix. The explicit form of the matrix is shown in Eq. (3.12) of the main text, and details for all its matrix elements are provided in Appendix 3.C.

3.E Bloch-Redfield theory

Having identified a suitable matrix representation for small and large detunings, we apply a unitary transformation to $\widetilde{H}$ that diagonalizes $\widetilde{H} - \sum_{j=1,2} H_{\mathrm{el-ph}}^{(j)}$ exactly. In order to decouple the qubit subspace $\{|(1,1)S\rangle$, $|(1,1)T_0\rangle\}$ perturbatively from the remaining states, we then perform a third-order Schrieffer-Wolff transformation, leading to corrections up to the third power in the electron-phonon coupling. The perturbation theory applies when the matrix elements for the electron-phonon coupling are smaller than the energy separation between the qubit and the other states.

The resulting effective Hamiltonian $H_{\mathrm{eff}} = H_{\mathrm{q}} + H_{\mathrm{q-ph}} + H_{\mathrm{ph}}$ for the S-T_0 qubit, its interaction with the phonon bath, and the bath itself can be described in terms of a coupled spin-1/2 system and allows application of the Bloch-Redfield theory [86, 96, 110]. Introducing the effective magnetic fields $\boldsymbol{B}_{\text{eff}}$ and $\boldsymbol{\delta B}$, we write the Hamiltonian of the qubit as

$$H_{\text{q}} = \frac{1}{2} g \mu_B \boldsymbol{B}_{\text{eff}} \cdot \boldsymbol{\sigma'}, \tag{3.135}$$

and the Hamiltonian for the interaction between the qubit and the phonon bath reads

$$H_{\text{q-ph}}(\tau) = \frac{1}{2} g \mu_B \boldsymbol{\delta B}(\tau) \cdot \boldsymbol{\sigma'}. \tag{3.136}$$

Here $\boldsymbol{\sigma'}$ is the vector of spin-1/2 Pauli matrices for the S-T_0 qubit, τ is the time, and the time-dependent $H_{\text{q-ph}}(\tau)$ is written in the interaction representation,

$$H_{\text{q-ph}}(\tau) = e^{iH_{\text{ph}}\tau/\hbar} H_{\text{q-ph}} e^{-iH_{\text{ph}}\tau/\hbar}. \tag{3.137}$$

Next, following Refs. [86, 96], we define the spectral functions

$$J_{ij}(\omega) = \frac{g^2 \mu_B^2}{2\hbar^2} \int_0^\infty e^{-i\omega\tau} \langle \delta B_i(0) \delta B_j(\tau) \rangle d\tau, \tag{3.138}$$

where the temperature-dependent correlators $\langle \delta B_i(0) \delta B_j(\tau) \rangle$ with $i, j \in \{x, y, z\}$ are calculated for a phonon bath in thermal equilibrium. More precisely, we assume that the density matrix ρ_{ph} that describes the mixed state of the phonon bath is diagonal when represented via standard Fock states for the phonons considered here (i.e., occupation numbers referring to acoustic phonons classified by the wave vectors $\boldsymbol{q}$ and modes s), with the probabilities on the diagonal provided by Boltzmann statistics. The correlator $\langle \delta B_i(0) \delta B_j(\tau) \rangle$ corresponds to the expectation value of the operator $\delta B_i(0) \delta B_j(\tau)$ and, thus, is equal to the trace of $\rho_{\text{ph}} \delta B_i(0) \delta B_j(\tau)$. In particular, one obtains $\langle a^\dagger_{\boldsymbol{q}s} a_{\boldsymbol{q'}s'} \rangle = \delta_{\boldsymbol{q},\boldsymbol{q'}} \delta_{s,s'} n_B(\omega_{\boldsymbol{q}s})$, where

$$n_B(\omega) = \frac{1}{e^{\hbar\omega/(k_B T)} - 1} \tag{3.139}$$

is the Bose-Einstein distribution, k_B is the Boltzmann constant, and T is the temperature.

Using the formulas (C16) and (C25)–(C27) from Ref. [96], it is possible to express the lifetimes of the qubit in terms of the above-mentioned spectral functions. For convenience, we define the basis of $\boldsymbol{\sigma'}$ such that only the z component of the effective magnetic field $\boldsymbol{B}_{\text{eff}}$ is nonzero. In this case, the lifetimes depend solely on the quantities

$$\begin{aligned} J^+_{ii}(\omega) &= \text{Re}[J_{ii}(\omega) + J_{ii}(-\omega)] \\ &= \frac{g^2 \mu_B^2}{2\hbar^2} \int_{-\infty}^{\infty} \cos(\omega\tau) \langle \delta B_i(0) \delta B_i(\tau) \rangle d\tau. \end{aligned} \tag{3.140}$$

The last equality holds because the $\delta B_i(\tau)$ are hermitian and the correlators are time-translational invariant. We finally calculate the relaxation time T_1 of the qubit via

$$\frac{1}{T_1} = J_{xx}^{+}(\omega_Z) + J_{yy}^{+}(\omega_Z), \tag{3.141}$$

where $\hbar\omega_Z = |g\mu_B \boldsymbol{B}_{\mathbf{eff}}|$ is the effective Zeeman splitting. The time T_φ that accounts for pure dephasing is obtained through

$$\frac{1}{T_\varphi} = J_{zz}^{+}(0), \tag{3.142}$$

and the decoherence time T_2 can then be expressed in terms of T_1 and T_φ,

$$\frac{1}{T_2} = \frac{1}{2T_1} + \frac{1}{T_\varphi}. \tag{3.143}$$

Considering one- and two-phonon processes in our calculations, the third-order contribution to $\delta B_i(0)$ $[\delta B_i(\tau)]$ enters the correlator $\langle \delta B_i(0)\delta B_i(\tau)\rangle$ in Eq. (3.140) together with the first-order contribution to $\delta B_i(\tau)$ $[\delta B_i(0)]$. As a consequence, the third-order terms in $\boldsymbol{\delta B}$ cannot contribute to the dephasing rate $1/T_\varphi$ (see also Appendix 3.G). Furthermore, we expect only a negligible effect on the relaxation rate $1/T_1$, as the rates that arise from third-order corrections can be considered small compared to those from single-phonon processes that are based solely on the first-order terms. For simplicity, the third-order contributions to $\boldsymbol{\delta B}$ are therefore omitted in the calculations for Figs. 3.2–3.6.

3.F Continuum Limit

For the investigation of the phonon-induced lifetimes of the qubit, we consider the continuum limit and replace the summation over the phonon wave vectors $\boldsymbol{q}$ by an integral. Furthermore, the low temperatures discussed here allow integration up to infinite q, because the effects resulting from terms with wave vectors outside the first Brillouin zone are clearly negligible. We therefore substitute

$$\sum_{\boldsymbol{q}} \rightarrow \frac{V}{(2\pi)^3} \int_0^\infty dq q^2 \int_0^\pi d\theta_{\boldsymbol{q}} \sin\theta_{\boldsymbol{q}} \int_0^{2\pi} d\phi_{\boldsymbol{q}} \tag{3.144}$$

in our calculations. For details of the electron-phonon interaction, see Appendix 3.B.

3.G Simple model for dephasing at large detuning

As discussed in Sec. 3.3 of the main text, the relevant dynamics at $0 < U - V_\pm - \epsilon < \hbar\omega_0$ and $\Omega = 0$ are very well described by the Hamiltonian

$$\widetilde{H} = \begin{pmatrix} 0 & \frac{\delta b_B}{2} & 0 \\ \frac{\delta b_B}{2} & V_+ - V_- & -\sqrt{2}t + P_S^\dagger \\ 0 & -\sqrt{2}t + P_S & V_+ - V_- + \Delta_S + \widetilde{P} \end{pmatrix} + H_{\mathrm{ph}} \tag{3.145}$$

with basis states $|(1,1)T_0\rangle$, $|(1,1)S\rangle$, and $|(0,2)S\rangle$. Compared to Eq. (3.12), we omitted here the decoupled states $|(1,1)T_+\rangle$, $|(1,1)T_-\rangle$, and $|(2,0)S\rangle$, subtracted P_T from the diagonal (global shift, no effect on the lifetimes), and introduced

$$\widetilde{P} = P_{SR} - P_T \tag{3.146}$$

as a matrix element for the electron-phonon coupling and

$$\Delta_S = U - V_+ - \epsilon \tag{3.147}$$

as the bare splitting between $|(1,1)S\rangle$ and $|(0,2)S\rangle$.

The hyperfine coupling, δ_B, is the only mechanism in Eq. (3.145) that couples the spin states and, hence, is crucial for the relaxation of the S-T_0 qubit. In fact, we find for the parameters in this work that the relaxation times T_1 are mainly determined by the hyperfine coupling rather than the SOI. In order to derive a simple model for the short decoherence times [$T_2 \ll T_1$, Fig. 3.2(a)], we neglect δ_B in the following, resulting in pure dephasing, and so $T_2 = T_\varphi$. Furthermore, we find that the matrix element P_S is negligible for our parameter range. Defining

$$\widetilde{H} = H_{\mathrm{s}} + H_{\mathrm{s-ph}} + H_{\mathrm{ph}} \tag{3.148}$$

and omitting δ_B and P_S, one obtains

$$H_{\mathrm{s}} = \begin{pmatrix} 0 & 0 & 0 \\ 0 & V_+ - V_- & -\sqrt{2}t \\ 0 & -\sqrt{2}t & V_+ - V_- + \Delta_S \end{pmatrix} \tag{3.149}$$

for the part that describes the electronic system, and

$$H_{\mathrm{s-ph}} = \begin{pmatrix} 0 & 0 & 0 \\ 0 & 0 & 0 \\ 0 & 0 & \widetilde{P} \end{pmatrix} \tag{3.150}$$

for the interaction with the phonon bath.

The Hamiltonians H_s and $H_\mathrm{s-ph}$ can be rewritten in a different basis $\{|(1,1)T_0\rangle, |(1,1)S'\rangle, |(0,2)S'\rangle\}$ as

$$H_\mathrm{s} = \begin{pmatrix} 0 & 0 & 0 \\ 0 & -J_\mathrm{tot} & 0 \\ 0 & 0 & -J_\mathrm{tot} + \Delta'_S \end{pmatrix} \tag{3.151}$$

and

$$H_\mathrm{s-ph} = \widetilde{P} \begin{pmatrix} 0 & 0 & 0 \\ 0 & v_{s'd}^2 & v_{s'd}v_{d'd} \\ 0 & v_{s'd}v_{d'd} & v_{d'd}^2 \end{pmatrix}, \tag{3.152}$$

where

$$\Delta'_S = \sqrt{\Delta_S^2 + 8t^2} \tag{3.153}$$

and

$$J_\mathrm{tot} = V_- - V_+ + \frac{\Delta'_S - \Delta_S}{2}. \tag{3.154}$$

The basis states

$$|(1,1)S'\rangle = v_{s's}|(1,1)S\rangle + v_{s'd}|(0,2)S\rangle, \tag{3.155}$$

$$|(0,2)S'\rangle = v_{d's}|(1,1)S\rangle + v_{d'd}|(0,2)S\rangle, \tag{3.156}$$

are normalized eigenstates of H_s. The notation $|(1,1)S'\rangle$ and $|(0,2)S'\rangle$ is justified because we consider $\Delta_S > 0$, and so $|v_{s's}|^2 > 1/2$ and $|v_{d'd}|^2 > 1/2$. In Eq. (3.152), $v_{s'd}$ and $v_{d'd}$ are assumed to be real. A suitable choice for the coefficients is, e.g.,

$$v_{s's} = \frac{\Delta_S + \Delta'_S}{D_+}, \tag{3.157}$$

$$v_{s'd} = \frac{2\sqrt{2}t}{D_+}, \tag{3.158}$$

$$v_{d's} = \frac{\Delta_S - \Delta'_S}{D_-}, \tag{3.159}$$

$$v_{d'd} = \frac{2\sqrt{2}t}{D_-}, \tag{3.160}$$

where the denominator

$$D_\pm = \sqrt{(\Delta_S \pm \Delta'_S)^2 + 8t^2} \tag{3.161}$$

ensures normalization.

Following the steps explained in Appendix 3.E, one finds

$$g\mu_B B_{\text{eff},z} = J_{\text{tot}} \tag{3.162}$$

and

$$\begin{aligned} g\mu_B \delta B_z &= -v_{s'd}^2 \widetilde{P} + \frac{v_{s'd}^2 v_{d'd}^2}{\Delta_S'} \widetilde{P}^2 \\ &\quad + \frac{v_{s'd}^2 v_{d'd}^2 \left(v_{s'd}^2 - v_{d'd}^2\right)}{(\Delta_S')^2} \widetilde{P}^3 \end{aligned} \tag{3.163}$$

from the third-order Schrieffer-Wolff transformation. We recall that $\delta B_x = 0 = \delta B_y$ due to omission of the hyperfine coupling, and so $T_2 = T_\varphi$ (pure dephasing). Furthermore, we note that the Bloch-Redfield theory requires $\langle \boldsymbol{\delta B}(\tau) \rangle$ to vanish [110]. Therefore, terms of type $a_{\boldsymbol{q}s}^\dagger a_{\boldsymbol{q}s}$ and $a_{\boldsymbol{q}s} a_{\boldsymbol{q}s}^\dagger$ must be removed from the second-order contributions to $\boldsymbol{\delta B}$ and, consequently, from the part $\propto \widetilde{P}^2$ in Eq. (3.163). The terms removed from $\boldsymbol{\delta B}$ can be considered as minor corrections to $\boldsymbol{B}_{\textbf{eff}}$, with $a_{\boldsymbol{q}s}^\dagger a_{\boldsymbol{q}s} \to n_B(\omega_{\boldsymbol{q}s})$ and $a_{\boldsymbol{q}s} a_{\boldsymbol{q}s}^\dagger \to n_B(\omega_{\boldsymbol{q}s}) + 1$, where $n_B(\omega)$ is the Bose-Einstein distribution, Eq. (3.139). In this work, we simply neglect these corrections to $\boldsymbol{B}_{\textbf{eff}}$ because of their smallness.

The decoherence time $T_2 = T_\varphi$ is calculated via

$$\frac{1}{T_2} = \frac{g^2 \mu_B^2}{2\hbar^2} \int_{-\infty}^{\infty} \langle \delta B_z(0) \delta B_z(\tau) \rangle d\tau, \tag{3.164}$$

see Appendix 3.E. Remarkably, the only nonzero contribution after insertion of Eq. (3.163) into Eq. (3.164) is

$$\frac{1}{T_2} = \frac{v_{s'd}^4 v_{d'd}^4}{2\hbar^2 (\Delta_S')^2} \int_{-\infty}^{\infty} \langle \widetilde{P}^2(0) \widetilde{P}^2(\tau) \rangle d\tau. \tag{3.165}$$

In particular, one finds that single-phonon processes cannot lead to dephasing,

$$\int_{-\infty}^{\infty} \langle \widetilde{P}(0) \widetilde{P}(\tau) \rangle d\tau = 0. \tag{3.166}$$

As there is no energy transfer between the electrons and the phonon bath (evaluation of $J_{zz}^+(\omega)$ at $\omega = 0$), the left-hand side of Eq. (3.166) can only be nonzero for a phonon with $\omega_{\boldsymbol{q}s} = 0 = q$, for which, however, the expression vanishes as well. An analogous explanation applies to

$$\int_{-\infty}^{\infty} \langle \widetilde{P}^3(0) \widetilde{P}(\tau) \rangle d\tau = 0 = \int_{-\infty}^{\infty} \langle \widetilde{P}(0) \widetilde{P}^3(\tau) \rangle d\tau. \tag{3.167}$$

Consequently, the dephasing in our model results purely from two-phonon processes that are based on the second-order contributions to δB_z.

Finally, using Eqs. (3.158) and (3.160) in Eq. (3.165) yields

$$\frac{1}{T_2} = \frac{2t^4}{\hbar^2(\Delta'_S)^6}\int_{-\infty}^{\infty}\langle \widetilde{P}^2(0)\widetilde{P}^2(\tau)\rangle d\tau. \tag{3.168}$$

We note that in the case of $|t| \ll \Delta_S$ and negligibly small $V_+ - V_-$, one finds $J_{\mathrm{tot}} \simeq 2t^2/\Delta'_S$ in this model and

$$\frac{2t^4}{\hbar^2(\Delta'_S)^6} \simeq \frac{J_{\mathrm{tot}}^2}{2\hbar^2(\Delta'_S)^4} \tag{3.169}$$

for the prefactor.

3.H Dephasing via singlet states at small detuning

In order to estimate the dephasing due to the states $|(2,0)S\rangle$ and $|(0,2)S\rangle$ in an unbiased DQD, $\epsilon \simeq 0$, we study a model similar to that of Appendix 3.G. Using $|(2,0)S\rangle$, $|(0,2)S\rangle$, $|(1,1)S\rangle$, and $|(1,1)T_0\rangle$ as the basis states, we consider

$$H_{\mathrm{s}} = \begin{pmatrix} U - V_- & 0 & -\sqrt{2}t & 0 \\ 0 & U - V_- & -\sqrt{2}t & 0 \\ -\sqrt{2}t & -\sqrt{2}t & V_+ - V_- & 0 \\ 0 & 0 & 0 & 0 \end{pmatrix} \tag{3.170}$$

as the Hamiltonian for the electronic system and

$$H_{\mathrm{s-ph}} = \begin{pmatrix} -\widetilde{P} & 0 & 0 & 0 \\ 0 & \widetilde{P} & 0 & 0 \\ 0 & 0 & 0 & 0 \\ 0 & 0 & 0 & 0 \end{pmatrix} \tag{3.171}$$

as the electron-phonon interaction. Again, we removed here P_T from the diagonal and neglected the off-diagonal matrix elements P_S and $P_S^\dagger$. Furthermore, we exploited the relation

$$P_{SL} - P_T = -(P_{SR} - P_T) = -\widetilde{P}. \tag{3.172}$$

This relation is based on the properties

$$\begin{aligned}\langle\Phi_L|\cos(\boldsymbol{q}\cdot\boldsymbol{r})|\Phi_L\rangle &= \langle\Phi_R|\cos(\boldsymbol{q}\cdot\boldsymbol{r})|\Phi_R\rangle, && (3.173)\\ \langle\Phi_L|\sin(\boldsymbol{q}\cdot\boldsymbol{r})|\Phi_L\rangle &= -\langle\Phi_R|\sin(\boldsymbol{q}\cdot\boldsymbol{r})|\Phi_R\rangle. && (3.174)\end{aligned}$$

Using the states $|\Phi_{L,R}\rangle$ defined in Appendix 3.A, Eq. (3.56), it is straightforward to show that these equations apply to our calculations (at least in very good approximation, given the small width of the 2DEG). Proceeding analogously to Appendix 3.G and exploiting $|t| \ll U - V_+$, the calculation of $T_2 = T_\varphi$ with Eqs. (3.170) and (3.171) yields

$$\frac{1}{T_2} = \frac{8t^4}{\hbar^2(U-V_+)^6}\int_{-\infty}^{\infty}\langle\widetilde{P}^2(0)\widetilde{P}^2(\tau)\rangle d\tau, \tag{3.175}$$

which is formally equivalent to Eq. (3.168).

Operation of the qubit at $\epsilon \simeq 0$ requires control over the tunnel coupling t, which can be achieved by changing the tunnel barrier of the DQD with electric gates.[3] Consequently, the value of t at $\epsilon \simeq 0$ is usually different from that at large ϵ. As a simple estimate, using $|t| \ll U - V_+$ and assuming that $V_+ - V_-$ and δ_B are negligible, one finds $J_{\mathrm{tot}} \simeq 4t^2/(U-V_+)$ through Taylor expansion of J_S, Eq. (3.120). Analogously, one obtains

$$\frac{8t^4}{\hbar^2(U-V_+)^6} \simeq \frac{J_{\mathrm{tot}}^2}{2\hbar^2(U-V_+)^4} \tag{3.176}$$

for the prefactor in Eq. (3.175). Considering J_{tot} to be the same in the biased and unbiased DQD, comparison with Eq. (3.169) yields a suppression factor on the order of $(\Delta_S')^4/(U-V_+)^4$. For the parameters in this work, the associated dephasing times at $\epsilon \simeq 0$ are therefore several orders of magnitude longer than those at large ϵ. The strong suppression allows omission of this mechanism in our model for an unbiased DQD described in Appendix 3.C.

The matrix elements P_S and $P_S^\dagger$ of the electron-phonon interaction provide a direct coupling between the state $|(1,1)S\rangle$ and the states $|(0,2)S\rangle$ and $|(2,0)S\rangle$. Consequently, these matrix elements enable dephasing via two-phonon processes even at $t = 0$. In the case of large detuning ϵ, the effect of P_S and $P_S^\dagger$ on the dephasing time T_φ (and on the lifetimes in general) turns out to be negligible. At $\epsilon \simeq 0$, this two-phonon-based contribution to T_φ is suppressed even further, by a factor on the order of $4\Delta_S^2/(U-V_+)^2$, and can therefore be neglected in the calculation with excited orbital states (see Appendix 3.C).

Table 3.1: Input parameters used for the calculations in the main text.

Parameter	Value	References
ϵ_r	13	
ρ	5.32 g/cm^3	
v_l	5.1×10^3 m/s	[97, 98, 99], Appendix 3.B
v_t	3.0×10^3 m/s	[97, 98, 99], Appendix 3.B
Ξ	-8 eV	[101, 102]
h_{14}	-0.16 As/m^2	[98, 99, 100]
g	-0.4	
B	0.7 T	[7, 40]
m_{eff}	6.1×10^{-32} kg	
$\Delta E = \hbar\omega_0$	$124\ \mu$eV	[10]
l_D	$1,\ 0.8,\ 0.5\ \mu$m	[104, 105, 106], Appendix 3.I
l_R	$2,\ 1.6,\ 1\ \mu$m	
$3a_z$	6 nm	Appendix 3.I
$L = 2a$	400 nm	
δb_B	$-0.14\ \mu$eV	[7, 10]
U	1 meV	[94]
V_+	$40,\ 50\ \mu$eV	[94]
V_-	$39.78,\ 49.5\ \mu$eV	[94], Appendix 3.I
t	$7.25,\ 24\ \mu$eV	[94], Appendix 3.I

3.I Summary of input parameters

Table 3.1 lists the values that were used for the results discussed in the main text. We note that the results are independent of the sample volume V, because the volume cancels out in the calculation.

It is worth mentioning that the values $l_D \sim$ 0.5–1 μm [104, 105, 106] for the Dresselhaus SOI are consistent with the assumed width of the 2DEG. Neglecting orbital effects, the general form of the Dresselhaus SOI for an electron in GaAs is

$$H_D = b_{41}^{6c6c} \left[\left(k_{y'}^2 - k_{z'}^2 \right) k_{x'} \sigma_{x'} + \text{ c.p.} \right], \tag{3.177}$$

where $\hbar k_i$ is the momentum along the i axis, σ_i is the corresponding Pauli operator for spin 1/2, the axes x', y', and z' are the main crystallographic axes [100], [010], and [001], respectively, "c.p." stands for cyclic permutations, and $b_{41}^{6c6c} \simeq 28$ Å^{3}eV [106]. For our 2DEG with strong confinement along the [001] direction (z axis), the Dresselhaus SOI can be well approximated by

$$H_D \simeq b_{41}^{6c6c} \langle \phi_{\mathrm{FH}} | k_z^2 | \phi_{\mathrm{FH}} \rangle \left(k_{y'} \sigma_{y'} - k_{x'} \sigma_{x'} \right), \tag{3.178}$$

where $z' = z$ and $\phi_{\mathrm{FH}}(z)$ is the Fang-Howard wave function of Eq. (3.47). Using $\langle \phi_{\mathrm{FH}} | k_z^2 | \phi_{\mathrm{FH}} \rangle = 1/(4a_z^2)$, one finds

$$l_D \simeq \frac{4\hbar^2 a_z^2}{m_{\mathrm{eff}} b_{41}^{6c6c}} \tag{3.179}$$

from comparison with Eqs. (3.67) and (3.74). With $m_{\mathrm{eff}} = 0.067 m_{\mathrm{el}}$ [106] as the effective electron mass in GaAs and m_{el} as the bare electron mass, evaluation of Eq. (3.179) with $3a_z = 6$ nm yields $l_D \simeq 0.65\ \mu$m, in good agreement with the values used in the calculation.

The splitting between the eigenstates of type $|(1,1)S\rangle$ and $|(1,1)T_0\rangle$ after diagonalization is denoted by $J_{\mathrm{tot}} = \hbar\omega_Z$. When $J_{\mathrm{tot}} \gg |\delta b_B|$, the spin states of these eigenstates are $|S\rangle$ and $|T_0\rangle$ with high accuracy, and the state of the S-T_0 qubit precesses around the z axis of the Bloch sphere. When the splitting is provided by the hyperfine coupling δb_B instead of the exchange interaction, the eigenstates are of type $|\uparrow\downarrow\rangle$ and $|\downarrow\uparrow\rangle$, leading to precessions around the x axis. In experiments, $J_{\mathrm{tot}} \gg |\delta b_B|$ is commonly realized for a biased DQD (large detuning) and the hyperfine coupling dominates in the unbiased case [10, 39]. In order to account for this feature, we set the parameters in Sec. 3.3 such that J_{tot} at $\epsilon \simeq 0$ would be largely provided by δb_B. Using U, V_+, V_-, and t approximately as in Ref. [94], we do this by adapting t (or V_-) such that $J_S \ll |\delta b_B|$, where J_S is the bare exchange splitting at $\epsilon = 0$, Eq. (3.120). The lifetimes in Figs. 3.2–3.5 were calculated with $U = 1$ meV, $V_+ = 40\ \mu$eV, $V_- = 39.78\ \mu$eV, and $t = 7.25\ \mu$eV, for which $J_S \ll |\delta b_B|$ is fulfilled. The detuning $\epsilon \sim 0.9$ meV in these calculations was chosen such that $J_{\mathrm{tot}} = 1.43\ \mu$eV, and we note that the excited states are negligible due to $0 < U - V_\pm - \epsilon < \hbar\omega_0$. In Fig. 3.6, where we consider operation at small detuning, the parameters $U = 1$ meV, $V_+ = 50\ \mu$eV, and $V_- = 49.5\ \mu$eV are similar to before. However, in order to achieve $J_{\mathrm{tot}} = 1.41\ \mu$eV at $\epsilon \simeq 0$, we use a larger tunnel coupling $t = 24\ \mu$eV. Experimentally, this can be realized by tuning the tunnel barrier of the DQD electrically [3].

CHAPTER 4

Phonon-assisted decay of singlet-triplet qubits in Si/SiGe quantum dots

Adapted from:
Viktoriia Kornich, Christoph Kloeffel, and Daniel Loss
"Phonon-assisted relaxation and decoherence of singlet-triplet qubits in Si/SiGe quantum dots",
ArXiv:1511.07369 (2016).

We study theoretically the phonon-induced relaxation and decoherence of spin states of two electrons in a lateral double quantum dot in a SiGe/Si/SiGe heterostructure. We consider two types of singlet-triplet spin qubits and calculate their relaxation and the decoherence times, in particular as a function of level hybridization, temperature, magnetic field, spin orbit interaction, and detuning between the quantum dots, using Bloch-Redfield theory. We show that the magnetic field gradient, which is usually applied to operate the spin qubit, may reduce the relaxation time by more than an order of magnitude. Using this insight, we identify an optimal regime where the magnetic field gradient does not affect the relaxation time significantly, and we propose regimes of longest decay times. We take into account the effects of one-phonon and two-phonon processes and suggest how our theory can be tested experimentally. The spin lifetimes we find here for Si-based quantum dots are significantly longer than the ones reported for their GaAs counterparts.

4.1 Introduction

Following the development in theory and experiment investigating the behavior of electron spin states in single and double quantum dots in Si [81, 84, 117, 118, 124, 125, 126, 127, 128, 129, 130, 131, 132, 133, 134, 135, 136], we study a lateral double quantum dot (DQD) built in a Si/SiGe heterostructure and occupied by two electrons. We consider the relaxation and decoherence of the two-electron spin states due to phonons. Given the recent high interest in spin qubits at the S-T_- anticrossing [15, 137], where S is a spin singlet and T_- a spin triplet with magnetic quantum number $m = -1$, we investigate how the relaxation time T_1 and the decoherence time T_2 of such qubits depend on temperature for different kinds of hybridization of the singlet. We derive and analyze the dependence of T_1 and T_2 on the magnetic field gradient, which is usually applied in order to operate the spin qubits [15, 16, 17, 18]. We further study the effects of one-phonon and two-phonon processes and suggest the regimes where our theory can be tested experimentally. We also consider the S-T_0 spin qubit [4, 5, 51] in two regimes: large detuning and small detuning, as it was done in our previous work on DQDs in GaAs/AlGaAs [138]. Here, T_0 is the spin triplet with $m = 0$. We investigate the dependence of T_1 and T_2 on temperature and on different system parameters which were not considered before.

This Chapter is organized as follows. In Sec. 4.2, we present the Hamiltonian of our model and a short description of the Bloch-Redfield theory. In Sec. 4.3, we study the relaxation and decoherence in S-T_--based spin qubits. The case of S-T_0 spin qubits is discussed in Sec. 4.4. Additional decay channels for the studied qubits are listed in Sec. 4.5 and our conclusions follow in Sec. 4.6. Details of the calculation are shown in the Appendix.

4.2 Model

Hamiltonian

We consider lateral DQDs in a Si/SiGe heterostructure grown along the crystallographic direction [001], which we also denote as z. The confinement in the plane perpendicular to z is generated by the gates. The homogeneous magnetic field $\boldsymbol{B}$ is in this plane. An applied magnetic field gradient, which is usually produced via a micromagnet, enables control over the Bloch sphere of the spin qubit even in the absence of hyperfine and spin orbit interactions [15, 16, 17, 18].

The Hamiltonian of the system reads

$$\begin{aligned} \tilde{H} &= \sum_{j=1,2} \left(H_0^{(j)} + H_Z^{(j)} + \tilde{H}_{SOI}^{(j)} + H_b^{(j)} + H_{el-ph}^{(j)} \right) \\ &\quad + H_C + H_{ph}, \end{aligned} \tag{4.1}$$

where j labels the electrons, H_0 comprises the kinetic and potential energy of an electron in a DQD potential, H_Z is the Zeeman term due to the external magnetic field, $\tilde{H}_{SOI}$ is the spin orbit interaction after a suitable transformation that accounts for the effect of higher-energy states [12, 85, 86, 87, 88], H_b is the term that describes the effect of the applied magnetic field gradient, H_{el-ph} is the electron-phonon interaction, H_C is the Coulomb repulsion, and H_{ph} is the Hamiltonian of the phonon bath. The details and definitions of Eq. (4.1) are presented in Ref. [138] (Sec. II and Appendix B), except for the applied magnetic field gradient and the electron-phonon interaction Hamiltonian which we provide below in general form for one electron.

The applied magnetic field gradient acts on electrons similarly to the stabilized nuclear polarization in GaAs DQDs that produces a different Overhauser field for each QD. The Hamiltonian is therefore of the same form as for the hyperfine interaction and reads

$$H_b = \frac{\boldsymbol{b} \cdot \boldsymbol{\sigma}}{4} (\mathcal{P}_L - \mathcal{P}_R), \tag{4.2}$$

where $\boldsymbol{b}$ appears due to the magnetic field gradient between the QDs, $\boldsymbol{\sigma}$ is the vector of spin 1/2 Pauli matrices for the electron spin, and $\mathcal{P}_L$ and $\mathcal{P}_R$ are projectors for the left and right QD, respectively [138].

Now we consider the electron-phonon interaction in Si. In contrast to GaAs, only the deformation potential electron-phonon interaction is present in Si. Another important difference is that the band minimum in bulk Si is sixfold degenerate. However, because of the strain in SiGe/Si/SiGe quantum wells this sixfold degeneracy is broken and there are only two degenerate valleys of lowest energy [81]. The confinement lifts the last degeneracy [81, 82]. Therefore, following Refs. [139, 140], the electron-phonon Hamiltonian for our system reads

$$H_{el-ph} = \Xi_d \operatorname{Tr} \boldsymbol{\varepsilon} + \Xi_u \hat{\boldsymbol{l}} \cdot \boldsymbol{\varepsilon} \cdot \hat{\boldsymbol{l}}. \tag{4.3}$$

Here, $\hat{\boldsymbol{l}}$ is a unit vector along the direction of the lowest-energy valley, in our case [001], $\boldsymbol{\varepsilon}$ is a strain tensor defined as

$$\varepsilon_{ij} = \frac{1}{2}\left(\frac{\partial u_i}{\partial r_j} + \frac{\partial u_j}{\partial r_i}\right), \tag{4.4}$$

where i, j denote the spatial components, $\boldsymbol{r}$ is the position in the material, and $\boldsymbol{u}$ is the displacement operator. The trace of the strain tensor is $\mathrm{Tr}\,\boldsymbol{\varepsilon}$. As we consider the valley in the [001] direction, in the end the electron-phonon Hamiltonian reads

$$H_{el-ph} = \Xi_d \mathrm{Tr}\,\boldsymbol{\varepsilon} + \Xi_u \varepsilon_{zz}. \tag{4.5}$$

The displacement operator can be represented in the form [138]

$$\boldsymbol{u} = \sum_{\boldsymbol{q},s} \sqrt{\frac{\hbar}{2\rho V q v_s}} \boldsymbol{e}_{\boldsymbol{q}s} \left(a_{\boldsymbol{q}s} \mp_s a^\dagger_{-\boldsymbol{q}s}\right) e^{i\boldsymbol{q}\cdot\boldsymbol{r}}, \tag{4.6}$$

where $s \in \{l, t_1, t_2\}$ stands for the longitudinal and transverse acoustic modes, $\boldsymbol{q}$ is a wave vector within the first Brillouin zone, and $q = |\boldsymbol{q}|$. We choose the normalized polarization vectors such that $\boldsymbol{e}_{\boldsymbol{q}l} = \boldsymbol{q}/q$, $\boldsymbol{e}_{-\boldsymbol{q}t_1} = -\boldsymbol{e}_{\boldsymbol{q}t_1}$, $\boldsymbol{e}_{-\boldsymbol{q}t_2} = \boldsymbol{e}_{\boldsymbol{q}t_2}$, and so $\mp_l = - = \mp_{t_1}$ and $\mp_{t_2} = +$. A phonon with properties $\boldsymbol{q}$ and s is annihilated and created by the operators $a_{\boldsymbol{q}s}$ and $a^\dagger_{\boldsymbol{q}s}$, respectively. For further calculations we use the density $\rho = 2.33$ g/cm^3, the deformation potential constants [140] $\Xi_d = 5$ eV and $\Xi_u = 8.77$ eV, and the averaged sound velocities [97, 98] $v_l = 9 \times 10^3$ m/s, $v_{t_1} = v_{t_2} = 5.4 \times 10^3$ m/s. Later on, when we calculate the qubit lifetimes, we can use the continuum limit and we integrate to infinite q for covenience, as terms with $\boldsymbol{q}$ outside the first Brillouin zone do not affect our results for the temperatures considered here. The sample volume V will cancel out in the analysis.

In this section we consider the Hamiltonian [Eq. (4.1)] in the basis $|(1,1)T_0\rangle$, $|(1,1)S\rangle$, $|(1,1)T_+\rangle$, $|(1,1)T_-\rangle$, $|(0,2)S\rangle$, $|(2,0)S\rangle$, where the first and second indices in parentheses correspond to the occupation number of the left and right QD, respectively, S denotes spin singlet states, and T denotes spin triplet states. As each minimum of the DQD potential in the plane of the 2DEG is well approximated by a 2D harmonic oscillator potential, we use linear combinations of the harmonic oscillator eigenfunctions to describe the in-plane orbital part of the electron state in the DQD potential [50]. For the explicit expressions of wave functions and details see Appendix A of Ref. [138]. Due to the strong confinement of the electrons in the growth direction, it turns out that the wave functions chosen along z hardly affect the phonon-assisted relaxation and decoherence processes that we are interested in. In contrast to Ref. [138], where a triangular potential based on typical GaAs/AlGaAs heterostructures was assumed, we consider a SiGe/Si/SiGe quantum well and approximate it by a hard-wall potential

$$V(z) = \begin{cases} \infty, & z < 0, \\ C, & 0 < z < a_z, \\ \infty, & z > a_z, \end{cases} \tag{4.7}$$

where C is a constant with units of energy and $z = 0,\ a_z$ corresponds to the interface between SiGe ($z < 0,\ z > a_z$) and Si ($0 < z < a_z$). The ground state wave function in such a potential is

$$\phi_z(z) = \sqrt{\frac{2}{a_z}} \sin\left[\frac{\pi z}{a_z}\right], \tag{4.8}$$

with a_z being a positive length that is interpreted as the width of the 2DEG in z direction. We take $a_z = 6$ nm for all numerical calculations in this work. We note that in experiments an electric field is usually applied along the growth direction of Si/SiGe heterostructures, which changes the shape of the assumed quantum well potential from rectangular toward triangular. However, as the electrons are strongly confined along z, the details of the well hardly affect the qubit lifetimes and we find that our results do not change by more than $\sim$10% when the potential becomes completely triangular. As a consequence, our theory is also well applicable to, e.g., lateral Si DQDs formed in Si/SiO$_2$ systems.

The Hamiltonian in our basis reads

$$\tilde{H} = \begin{pmatrix} P_T & \frac{b_B}{2} & 0 & 0 & 0 & 0 \\ \frac{b_B}{2} & V_+ - V_- + P_T & \frac{\Omega}{\sqrt{2}} - \frac{1}{2\sqrt{2}}(b_x + ib_z) & -\frac{\Omega}{\sqrt{2}} + \frac{1}{2\sqrt{2}}(b_x - ib_z) & -\sqrt{2}t + P_S^\dagger & -\sqrt{2}t + P_S \\ 0 & \frac{\Omega}{\sqrt{2}} - \frac{1}{2\sqrt{2}}(b_x - ib_z) & E_Z + P_T & 0 & 0 & 0 \\ 0 & -\frac{\Omega}{\sqrt{2}} + \frac{1}{2\sqrt{2}}(b_x + ib_z) & 0 & -E_Z + P_T & 0 & 0 \\ 0 & -\sqrt{2}t + P_S & 0 & 0 & -\epsilon + U - V_- + P_{SR} & 0 \\ 0 & -\sqrt{2}t + P_S^\dagger & 0 & 0 & 0 & \epsilon + U - V_- + P_{SL} \end{pmatrix} + H_{ph},$$

where t is the tunnel coupling, U is the onsite repulsion, V_+ and V_- are the matrix elements of Coulomb interaction, $E_Z = g\mu_B B$ with $g = 2$ as the Si g-factor is the Zeeman splitting, μ_B is the Bohr magneton, and $B = |\boldsymbol{B}|$. The terms b_x, b_z, and b_B are produced by an applied magnetic field gradient along x, z axes and $\boldsymbol{B}$, respectively, where the three directions for x, z, and $\boldsymbol{B}$ form a right-handed basis. For simplicity, we set $b_z = 0$ in the following, as it can be achieved experimentally using a micromagnet. The electrical bias (detuning) between the dots is denoted by ϵ, where $\epsilon = 0$ is for the unbiased DQD [94].

The electron-phonon matrix elements are

$$\begin{aligned} P_T &= \langle (1,1)S| \sum_{j=1,2} H^{(j)}_{el-ph} |(1,1)S\rangle \qquad (4.9) \\ &= \langle (1,1)T_0| \sum_{j=1,2} H^{(j)}_{el-ph} |(1,1)T_0\rangle, \\ P_S &= \langle (1,1)S| \sum_{j=1,2} H^{(j)}_{el-ph} |(2,0)S\rangle \qquad (4.10) \\ &= \langle (0,2)S| \sum_{j=1,2} H^{(j)}_{el-ph} |(1,1)S\rangle, \\ P_{SR} &= \langle (0,2)S| \sum_{j=1,2} H^{(j)}_{el-ph} |(0,2)S\rangle, \qquad (4.11) \\ P_{SL} &= \langle (2,0)S| \sum_{j=1,2} H^{(j)}_{el-ph} |(2,0)S\rangle. \qquad (4.12) \end{aligned}$$

As evident from the provided equations, these matrix elements have a similar structure but differ due to the integrals for the orbital parts. We note that the matrix elements all commute with each other, even though they still contain the creation and annihilation operators for the phonons.

The matrix element Ω comes from SOI and has the form [88, 138]

$$\Omega = \frac{F(L,l_c) g\mu_B B}{l_R} \cos\eta. \qquad (4.13)$$

The function $F(L,l_c)$ depends on the distance L between the centers of the QDs and the confinement length $l_c = \sqrt{\hbar^2/(m_{\text{eff}}\Delta E)}$, where $m_{\text{eff}} = 1.73 \times 10^{-31}$ kg is the effective mass of an electron in Si and ΔE is the orbital level spacing in each QD. We note that l_c determines the Gaussian decay of the wave functions and $F(L,l_c) \approx -L$ when the dots are only weakly coupled. The Rashba length $l_R = \hbar/(m_{\text{eff}}\alpha)$ is related to the SOI amplitude α in the Rashba Hamiltonian, and η is the angle between $\boldsymbol{B}$ and the axis that connects the two QDs.

Bloch-Redfield theory

To calculate the relaxation time T_1 and decoherence time T_2 we use the Bloch-Redfield theory [86, 96], which describes the dynamics of the qubit interacting with the bath of phonons. In the following we will consider S-T_- and S-T_0 qubits. To decouple the qubit subspace from the other states, we first apply a unitary transformation to $\widetilde{H}$ that diagonalizes $\tilde{H} - H^{(1)}_{el-ph} - H^{(2)}_{el-ph}$, where (1) and (2) label the first and second electron, respectively. The transformation matrix for this first step is found numerically. Depending on the qubit under study (S-T_0 or S-T_-), we then we perform a Schrieffer-Wolff transformation up to the third order to take into account both one-phonon and two-phonon processes. The Schrieffer-Wolff transformation is valid when the matrix elements resulting from electron-phonon coupling are much smaller than the energy difference between the qubit subspace and other states. After the Schrieffer-Wolff transformation, the qubit subspace is well separated from other states, which allows us to study the dynamics in terms of an effective Hamiltonian of the form $H_q + H_{q-ph}(\tau) + H_{ph}$, where H_q is a 2×2 part that contains information about the qubit without phonons and $H_{q-ph}(\tau)$ is the interaction between qubit and phonons at time τ in the interaction representation.

Defining the pseudo-spin vector $\tilde{\boldsymbol{\sigma}}$ as a vector of Pauli matrices $\sigma_{\tilde{x}}, \sigma_{\tilde{y}}, \sigma_{\tilde{z}}$ in the qubit subpace, where $\tilde{x}$, $\tilde{y}$, $\tilde{z}$ are the directions in the pseudo-spin space, we can represent H_q and H_{q-ph} as

$$H_q = B_{\text{eff}}\sigma_{\tilde{z}}, \tag{4.14}$$

$$H_{q-ph} = \delta\boldsymbol{B}(\tau)\cdot\tilde{\boldsymbol{\sigma}}, \tag{4.15}$$

where B_{eff} is a positive energy and $\delta\boldsymbol{B}(\tau)$ contains electron-phonon interaction matrix elements. The expressions for B_{eff} and $\delta\boldsymbol{B}(\tau)$ result from all linear transformations performed before and are newly calculated whenever the input parameters or the qubit type change. Following the theory from Refs. [86, 96], the times T_2 and T_1 are

$$\frac{1}{T_2} = \frac{1}{2T_1} + \frac{1}{T_\varphi}, \tag{4.16}$$

$$\frac{1}{T_1} = J^{+}_{\tilde{x}\tilde{x}}(\Delta_{ST}) + J^{+}_{\tilde{y}\tilde{y}}(\Delta_{ST}), \tag{4.17}$$

$$\frac{1}{T_\varphi} = J^{+}_{\tilde{z}\tilde{z}}(0). \tag{4.18}$$

The quantity Δ_{ST} is defined as $\Delta_{ST} = 2B_{\text{eff}}$, i.e., the energy splitting between qubit states without taking into account electron-phonon interaction, and

$$J^{+}_{ii}(\hbar\omega) = \frac{2}{\hbar^2}\int_{-\infty}^{\infty}\cos(\omega\tau)\langle\delta B_i(0)\delta B_i(\tau)\rangle d\tau. \tag{4.19}$$

The correlator $\langle\delta B_i(0)\delta B_i(\tau)\rangle$ is evaluated for a phonon bath in thermal equilibrium at temperature T. The time T_φ represents the pure dephasing part in the decoherence time T_2.

4.3 S-T_- qubit

Following the interest in building a qubit based on the S-T_- anticrossing [15, 137] we study phonon-induced relaxation and decoherence for the electron spin states at this anticrossing. Because of tunnel coupling, magnetic field gradient, and SOI all the states in our basis are hybridized to some extent. We therefore consider two possible regimes: the state that mainly consists of $|(1,1)T_-\rangle$ (we denote it as $|(1,1)T'_-\rangle$) anticrosses with the state that is mainly $|(0,2)S\rangle$ ($|(0,2)S'\rangle$) or mainly $|(1,1)S\rangle$ ($|(1,1)S'\rangle$). This can also be seen from the spectrum. In Fig. 4.1a we plotted the dependence of the energy of electron states on the detuning ϵ. The green circle highlights the region of anticrossing between $|(1,1)T'_-\rangle$ and $|(0,2)S'\rangle$, which is shown enlarged in Fig. 4.1b. In Fig. 4.2 we choose different parameters and show the anticrossing between $|(1,1)T'_-\rangle$ and $|(1,1)S'\rangle$. When plotting these spectra, the electron-phonon interaction was omitted.

The qubit based on $|(1,1)T'_-\rangle$-$|(0,2)S'\rangle$

Here we study the case shown in Fig. 4.1. We plot the dependence of T_1 and T_2 on temperature T in Fig. 4.3, for which we used the following parameters: $B = 0.4$ T, $t = 10\,\mu$eV, $V_+ = 40\,\mu$eV, $V_- = 39.99\,\mu$eV, $U = 1.2$ meV, $b_x = 2\,\mu$eV, $L = 150$ nm, $l_c = 42.7$ nm (i.e., $\Delta E = 200\,\mu$eV), and $\epsilon = 1.201988$ meV. The region where $|(1,1)T'_-\rangle$ and $|(0,2)S'\rangle$ anticross is typically quite narrow, and therefore such a high precision in ϵ is needed to operate exactly in the anticrossing center. That is the point where, if we take $b_x - 2\Omega = 0$, the energies of $|(0,2)S'\rangle$ and $|(1,1)T'_-\rangle$ are equal, i.e., $|(0,2)S'\rangle$ and $|(1,1)T_-\rangle$ cross. We take $b_B = 0$ to decouple the qubit subspace from $|(1,1)T_0\rangle$ [137].

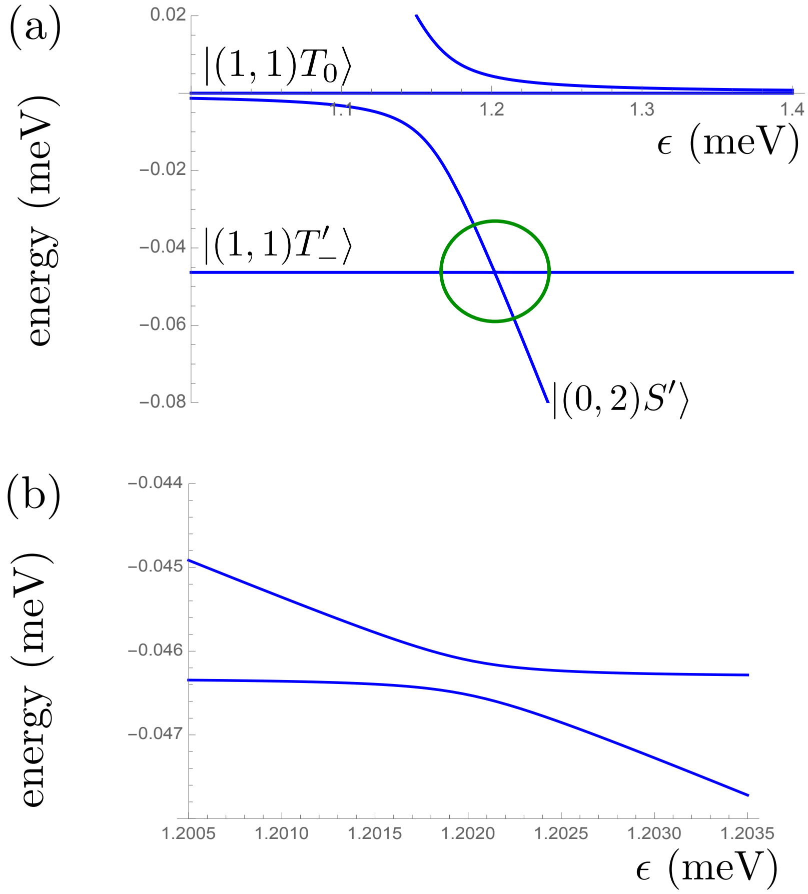

Figure 4.1: (a) The energy spectrum of two-electron states in a double quantum dot as a function of detuning ϵ denoting the energy difference between the two dots. The green circle shows the S-T_- anticrossing, which is shown enlarged in (b). The parameters used are the same as for Fig. 4.3. At the anticrossing, the singlet state is of type $|(0,2)S\rangle$.

As SOI enters in Eq. (4.9) together with b_x, we neglect it assuming $|\Omega| \ll |b_x|$. In lateral SiGe/Si/SiGe QDs, SOI might be due to QD confinement or other applied electric fields, imperfections of the quantum well [141], or interface effects between two semiconductors [142, 143]. According to Ref. [141], the spin-orbit length is $l_R = 73\ \mu$m. Using this value, we get $\Omega = -0.095\ \mu$eV. The SOI due to interface effects between semiconductors is absent if the amount of atomic monolayers of Si is even [144]. However, experimental values for any of the three origins

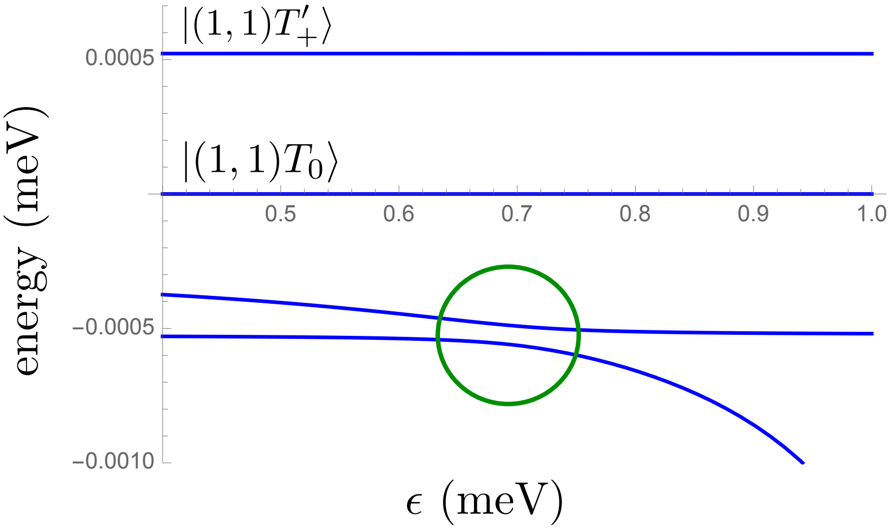

Figure 4.2: The energy spectrum of two-electron states in a double quantum dot as a function of detuning ϵ. The green circle shows the S-T_- anticrossing. The parameters used are the same as for Fig. 4.9. At the anticrossing, the singlet state is of type $|(1,1)S\rangle$.

mentioned above are not known to us for present-day samples.

In Fig. 4.3 we see that $T_2 \simeq 2T_1$, that means the relaxation part dominates over dephasing in T_2 [see Eq. (4.16)]. Up to a temperature of $T = 0.08$ K, both T_1 and T_2 decay slowly and then change their behaviour to a more rapid decay. To explain this change at around $T \simeq 0.08$ K we plot the one-phonon process decoherence rate (Γ_2^{1p}) and two-phonon process decoherence rate (Γ_2^{2p}), see Fig. 4.4. These rates contribute to T_2 as

$$\frac{1}{T_2} \equiv \Gamma_2 = \Gamma_2^{1p} + \Gamma_2^{2p}. \tag{4.20}$$

We note that the one-phonon process can lead only to relaxation, it cannot lead to dephasing [138]. Therefore $\Gamma_2^{1p} = \Gamma_1^{1p}/2$, where Γ_1^{1p} is the one-phonon process relaxation rate. From Fig. 4.4 we can see that $\Gamma_2^{1p} \propto T$ for the whole interval of temperatures. This is so because the dominant terms in Γ_2^{1p} are proportional to a Bose-Einstein distribution,

$$\Gamma_2^{1p} \propto (e^{\frac{\Delta_{ST}}{k_B T}} - 1)^{-1} \simeq \frac{k_B T}{\Delta_{ST}}. \tag{4.21}$$

In our case $\Delta_{ST} \ll k_B T$ for all temperatures under consideration, therefore the second equality in Eq. (4.21) is justified. The two-phonon pro-

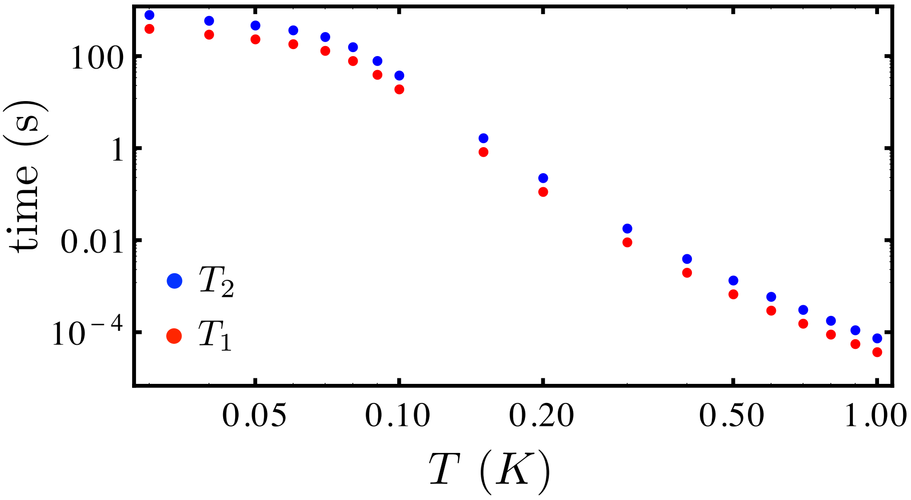

Figure 4.3: The dependence of T_1 (red) and T_2 (blue) on temperature for the parameters listed in Sec. 4.3. The anticrossing is between $|(1,1)T'_-\rangle$ and $|(0,2)S'\rangle$.

cess rate Γ_2^{2p} has a more complicated dependence on temperature. For $0.03\,\mathrm{K} < T < 0.07\,\mathrm{K}$, we find $\Gamma_2^{2p} \propto C_1 + C_2T^9$, where C_1 and C_2 are constants, then it grows more slowly, and for $0.5\,\mathrm{K} < T < 1\,\mathrm{K}$ $\Gamma_2^{2p} \propto T^4$. Consequently, the change in the decay of T_1 and T_2 at $T \simeq 0.08\,\mathrm{K}$ in Fig. 4.3 is due to the fact that for lower temperatures the relaxation happens mainly via one-phonon processes, with rate $\propto T$, and for higher temperatures two-phonon processes dominate with the rate depending on higher powers of T. The crossover between these two regimes occurs at around 0.08 K (see Fig. 4.4).

As the magnetic field gradient is determined by the design of the experimental setup, we also plot the dependence of T_1 and T_2 on b_x, see Fig. 4.5. The parameter values we used are the same as for Fig. 4.3 and $T = 100$ mK. Here again $T_2 \simeq 2T_1$. We can see a plateau up to $b_x \sim 2$ μeV and then a decay for both T_1 and T_2. To explain this behavior we study the dependence of Γ_2^{1p} and Γ_2^{2p} on b_x, see Fig. 4.6. The rate Γ_2^{1p} scales as $\Gamma_2^{1p} \propto C_3 + C_4b_x^4$, where C_3 and C_4 are constants. The rate Γ_2^{2p} does not change noticeably with b_x, and we will comment on this using a simple model in Sec. 4.3. Consequently, as for smaller b_x the rate Γ_2^{2p} dominates, there is a plateau in the regime of small b_x. For $b_x > 3$ μeV the rate Γ_2^{1p} dominates, therefore both T_1 and T_2 decay.

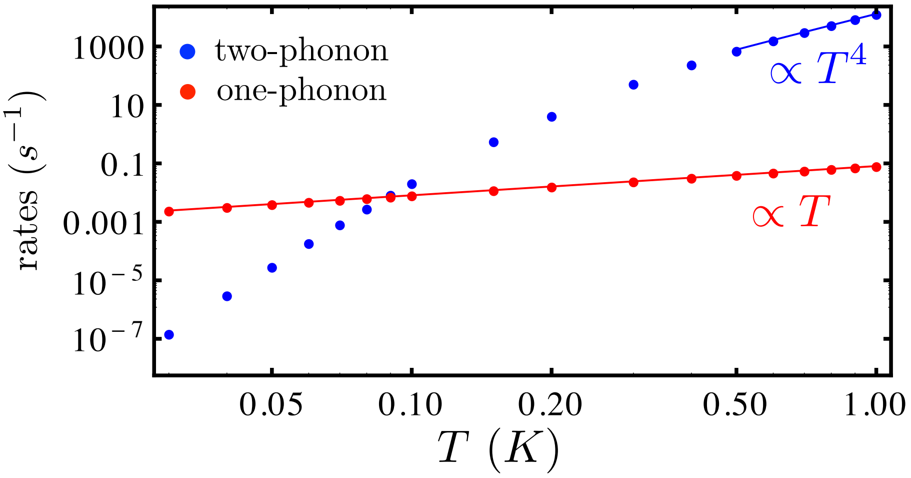

Figure 4.4: The dependence of one-phonon (Γ_2^{1p}, red) and two-phonon (Γ_2^{2p}, blue) components of the decoherence rate $1/T_2 = \Gamma_2^{1p} + \Gamma_2^{2p}$ on temperature. The parameters are the same as in Fig. 4.3.

In Fig. 4.3 we see that phonon-assisted relaxation and decoherence are weak compared to the ones usually reported for GaAs. Nevertheless, we found regimes where T_1 and T_2 are in the millisecond range, so that phonon-assisted relaxation and dephasing may dominate over other sources of decoherence in the sample. This provides an option to test our theory experimentally. We suggest to consider two cases: when the one-phonon process dominates and when the two-phonon process dominates.

To get the one-phonon process dominating, we use the following parameters: $b_x = 10\ \mu$eV, $\epsilon = 1.173$ meV, $T = 100$ mK, and the other parameters are the same as for Fig. 4.3. This means we have a similar spectrum as in Fig. 4.1 and stay in the region to the left from the denoted anticrossing to have a large splitting between the qubit states, which increases the one-phonon relaxation rate. In Fig. 4.7 we plotted the dependence of T_1 on the applied magnetic field B. Here T_1 is mainly determined by the one-phonon process, therefore $T_1 \simeq 1/\Gamma_1^{1p}$. The decay scales as $T_1 \propto B^{-4}$. We note that we do not expect this power-law to be universal for all possible parameter values.

To test experimentally our theory of the two-phonon process, we suggest to change the magnetic field B around the value where we are ex-

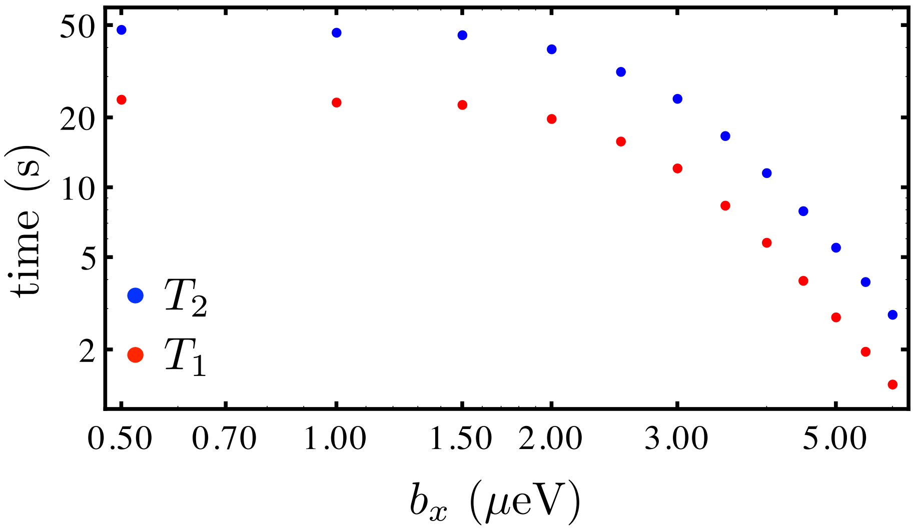

Figure 4.5: The dependence of T_1 (red) and T_2 (blue) on b_x. The temperature for this plot is $T = 100$ mK, and the other parameters are listed in Sec. 4.3. The anticrossing is between $|(1,1)T'_-\rangle$ and $|(0,2)S'\rangle$.

actly in the center of the anticrossing, and to use rather small b_x. We need b_x to be small enough, because at larger b_x the one-phonon process starts to dominate as evident from Fig. 4.6. Therefore, we use $b_x = 1$ μeV, $T = 500$ mK, and the other parameters as for Fig. 4.3. We plot the B dependence of T_2 and T_1 in Fig. 4.8. Here we see a sharp peak for T_2 at $B = 0.4$ T, which is the center of the anticrossing between $|(0,2)S'\rangle$ and $|(1,1)T'\rangle$. Interestingly, dephasing is dominating for $B < 0.395$ T, $B > 0.405$ T, and the peak itself is limited by relaxation. The relaxation time T_1 is limited by two-phonon processes only at $0.375\,\mathrm{T} < B < 0.425$ T. Apart from its usefulness for checking our theory of two-phonon processes the peak in T_2 (or dip in T_1) is a clear indication of the $|(0,2)S'\rangle$ and $|(1,1)T'_-\rangle$ anticrossing center, the point which is most interesting for spin qubit operation [15, 137].

Taking into account that the phonon-induced decoherence still allows for relatively long qubit lifetimes, we suppose that for the present-day samples the main source of decoherence in such a qubit will be charge noise, because the anticrossing region is quite narrow. However, as was discussed in Ref. [15], the charge noise can be substantially reduced using $t \gg E_Z$.

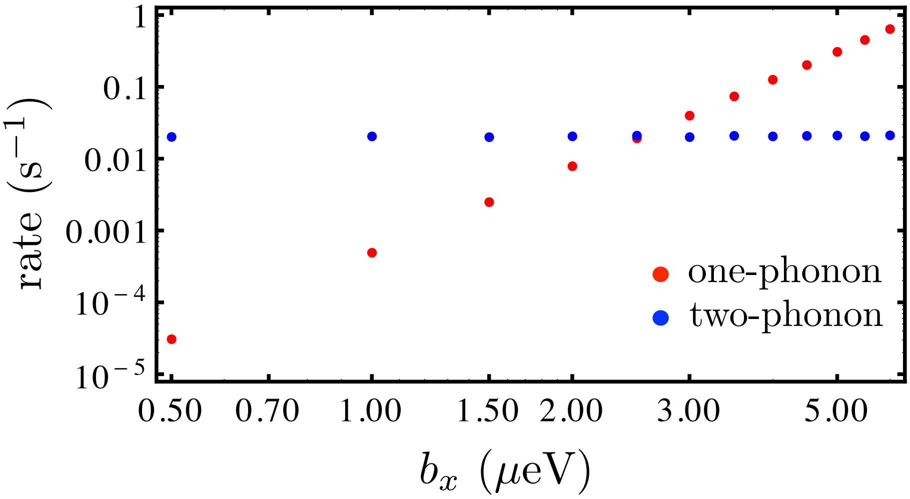

Figure 4.6: The dependence of one-phonon (Γ_2^{1p}) and two-phonon (Γ_2^{2p}) components of the decoherence rate $1/T_2 = \Gamma_2^{1p} + \Gamma_2^{2p}$ on b_x. The parameters are the same as in Fig. 4.5.

Simple model for the qubit based on $|(1,1)T'_-\rangle$-$|(0,2)S'\rangle$

To analyze the results presented above, we propose to consider a simple model, which besides energy separation arguments discussed below is also justified by comparison with our numerical calculations. The states that are closest in energy to our $|(1,1)T'_-\rangle$-$|(0,2)S'\rangle$ qubit subspace are $|(1,1)T_0\rangle$ and $|(1,1)S'\rangle$. However, $|(1,1)T_0\rangle$ is decoupled from the qubit subspace when $b_B = 0$. Therefore we consider the Hamiltonian in the basis $|(1,1)T_-\rangle, |(0,2)S\rangle, |(1,1)S\rangle$:

$$\begin{aligned}\tilde{H} &= \begin{pmatrix} -E_Z & 0 & \frac{1}{2\sqrt{2}}b_x \\ 0 & -\epsilon + U - V_- + \tilde{P} & -\sqrt{2}t + P_S \\ \frac{1}{2\sqrt{2}}b_x & -\sqrt{2}t + P_S^\dagger & V_+ - V_- \end{pmatrix} \\ &+ H_{ph},\end{aligned} \tag{4.22}$$

where $\tilde{P} = P_{SR} - P_T$. Our numerical calculation also showed that P_S and $P_S^\dagger$ can be neglected, therefore we will omit them in this subsection.

First of all we have to find the center of the $|(0,2)S'\rangle$-$|(1,1)T'_-\rangle$ anti-crossing. For that we diagonalize the phonon-independent part of $\tilde{H}$ in

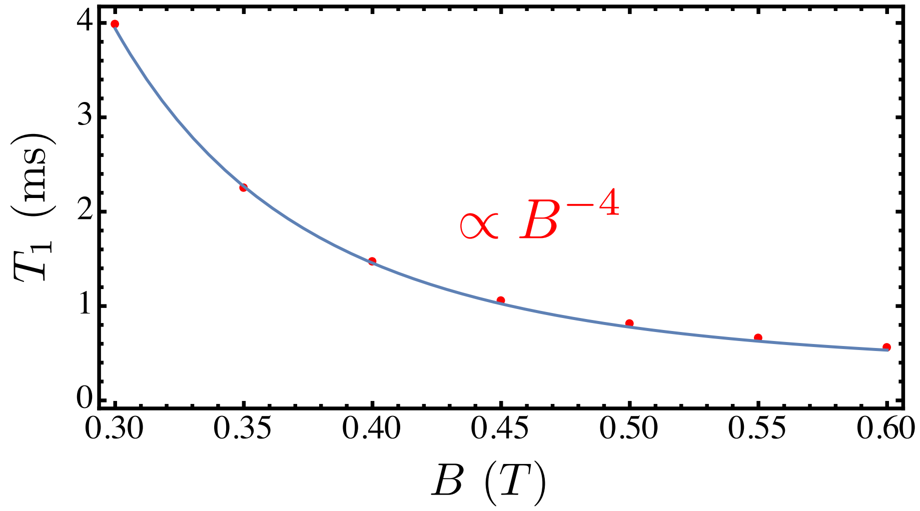

Figure 4.7: The dependence of T_1 on the absolute value B of the magnetic field for $T = 100$ mK and the parameters in the text. The blue line shows a power-law decay $\propto B^{-4}$. The detuning ϵ was chosen near (but not exactly at) the anticrossing between $|(1,1)T'_-\rangle$ and $|(0,2)S'\rangle$.

the basis $|S(0,2)\rangle$, $|S(1,1)\rangle$. This transformation is [94]

$$U_1 = \begin{pmatrix} 1 & 0 & 0 \\ 0 & \cos(\phi/2) & -\sin(\phi/2) \\ 0 & \sin(\phi/2) & \cos(\phi/2) \end{pmatrix}, \tag{4.23}$$

where

$$\cos\phi = \frac{-U + V_+ + \epsilon}{\sqrt{8t^2 + (-U + V_+ + \epsilon)^2}}, \tag{4.24}$$

$$\sin\phi = \frac{2\sqrt{2}t}{\sqrt{8t^2 + (-U + V_+ + \epsilon)^2}}. \tag{4.25}$$

Consequently, the matrix $U_1^\dagger \tilde{H} U_1$ corresponds to the Hamiltonian $\tilde{H}$ written in the basis $\{|(1,1)T_-\rangle, |(0,2)S'\rangle, |(1,1)S'\rangle\}$, if we set $b_x = 0$. The anticrossing center is the point where the energy of $|(1,1)T_-\rangle$ is equal to the energy of $|(0,2)S'\rangle$ (with $b_x = 0$ and $\tilde{P} = 0$). From this condition we find the detuning ϵ at which the anticrossing occurs,

$$\epsilon = E_Z + U - V_- - \frac{2t^2}{E_Z - V_- + V_+}. \tag{4.26}$$

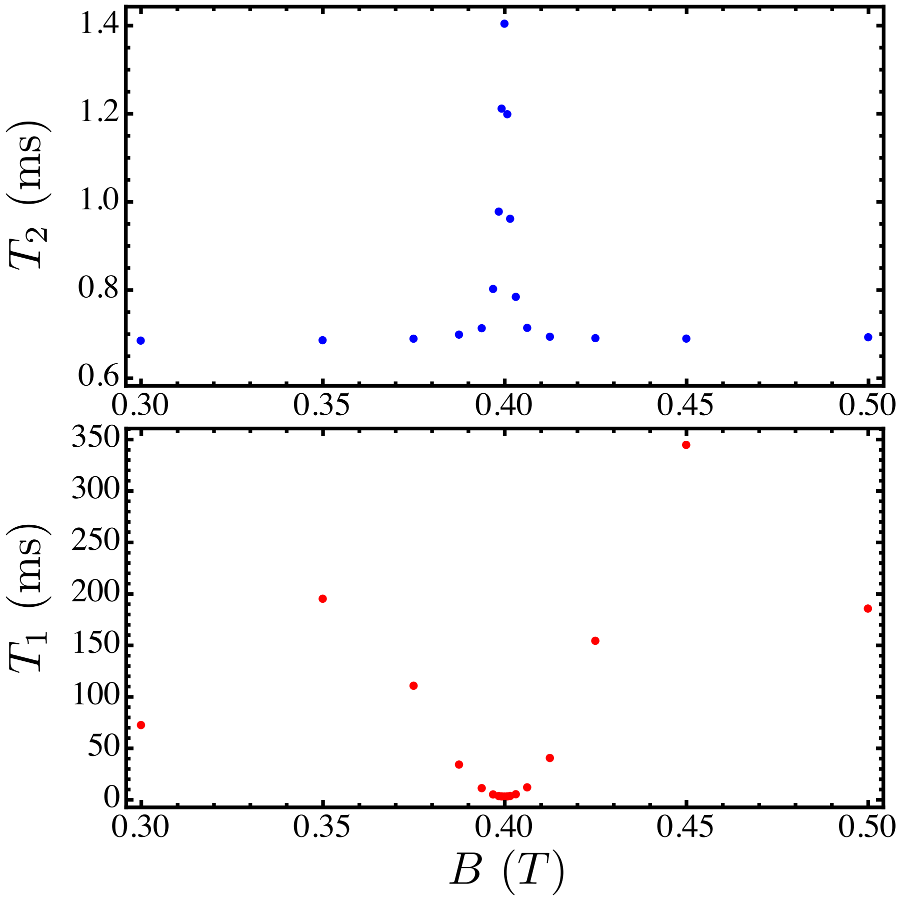

Figure 4.8: The dependence of T_2 and T_1 on the absolute value B of the magnetic field for $T = 500$ mK and the parameters in the text. The center of the anticrossing between $|(1,1)T'_-\rangle$ and $|(0,2)S'\rangle$ is at $B = 0.4$ T. The peak of T_2 at $B = 0.4$ T is limited by T_1, i.e., $T_2 \simeq 2T_1$, whereas the valleys at $B < 0.395$ T, $B > 0.405$ T are dominated by T_φ. In this figure, T_2 is due to two-phonon processes, one-phonon processes are negligible. For T_1, two-phonon processes dominate at 0.375 T $< B < 0.425$ T.

Assuming that $|b_x|$, $|t|$, and $\tilde{P}$ (may, e.g., be estimated via the expectation value of $\tilde{P}^2$) are much smaller than $\Delta = \sqrt{8t^2 + (U - V_+ - \epsilon)^2}$, we perform a Schrieffer-Wolff transformation up to the third order. The resulting Hamiltonian is then split into the part which does not contain phonons, the part with electron-phonon interaction, and H_{ph}. To simplify the analysis we apply to this Hamiltonian a unitary transformation U_2 which exactly diagonalizes the part of the Hamiltonian without phonons,

$$U_2 = \begin{pmatrix} \cos(\Theta/2) & -\sin(\Theta/2) \\ \sin(\Theta/2) & \cos(\Theta/2) \end{pmatrix}, \tag{4.27}$$

where the angle Θ is defined in Appendix 4.A.

After all transformations our Hamiltonian is $H_q + H_{el-ph}(\tau) + H_{ph}$ as it was described in Sec. 4.2. Therefore, in order to understand the results from Sec. 4.3, we present here the expression for $\delta B_{\tilde{z}}(\tau)$ which induces dephasing and the one for $\delta B_{\tilde{x}}(\tau)$ which induces relaxation,

$$\begin{aligned} \delta B_{\tilde{x}}(\tau) &= \frac{1}{128\Delta^3}\left[\tilde{P}(\tau)\cos^2\left[\frac{\phi}{2}\right](G_1\cos\Theta - G_2\sin\Theta)\right. \\ &\quad \left. +\tilde{P}^2(\tau)(G_3\cos\Theta - G_4\sin\Theta)\right], \end{aligned} \tag{4.28}$$

$$\begin{aligned} \delta B_{\tilde{z}}(\tau) &= \frac{1}{128\Delta^3}\left[\tilde{P}(\tau)\cos^2\left[\frac{\phi}{2}\right](G_1\sin\Theta + G_2\cos\Theta)\right. \\ &\quad \left. +\tilde{P}^2(\tau)(G_3\sin\Theta + G_4\cos\Theta)\right]. \end{aligned} \tag{4.29}$$

We note that $\delta B_{\tilde{y}}(\tau) = 0$, and we introduced

$$G_1 = \sqrt{2} b_x \sin\left[\frac{\phi}{2}\right]\left(b_x^2 + 32\Delta^2 - 7b_x^2\cos\phi\right), \tag{4.30}$$

$$G_2 = 4\Delta\left(b_x^2 - 16\Delta^2 - b_x^2\cos\phi\right), \tag{4.31}$$

$$\begin{aligned} G_3 &= 2\sqrt{2} b_x \sin\phi\cos\left[\frac{\phi}{2}\right]\Big(5\tilde{P}(\tau) - 4\Delta \\ &\quad +5\tilde{P}(\tau)\cos[2\phi] + [8\Delta - 6\tilde{P}(\tau)]\cos\phi\Big), \end{aligned} \tag{4.32}$$

$$G_4 = 16\Delta\sin^2\phi\left(\Delta + \tilde{P}(\tau)\cos\phi\right) \tag{4.33}$$

for convenience. Using Eqs. (4.28) and (4.29) we get the expressions for $\delta B_{\tilde{x}}(0)\delta B_{\tilde{x}}(\tau)$ and $\delta B_{\tilde{z}}(0)\delta B_{\tilde{z}}(\tau)$. To simplify them we use the fact that $\Theta \simeq \pi/2$ and $\Delta \gg |b_x|$, and get

$$\begin{aligned} \delta B_{\tilde{x}}(0)\delta B_{\tilde{x}}(\tau) &\simeq \tfrac{1}{64\Delta^2}\Big[16\cos^4\left[\tfrac{\phi}{2}\right]\Delta^2\tilde{P}(0)\tilde{P}(\tau) - \\ &4\cos^2\left[\tfrac{\phi}{2}\right]\cos\phi\sin^2\phi\big[\tilde{P}^3(0)\tilde{P}(\tau) + \tilde{P}(0)\tilde{P}^3(\tau)\big] + \sin^4\phi\tilde{P}^2(0)\tilde{P}^2(\tau)\Big], \end{aligned} \tag{4.34}$$

$$\begin{aligned} \delta B_{\tilde{z}}(0)\delta B_{\tilde{z}}(\tau) &\simeq \tfrac{1}{32\Delta^4}\cos^4\left[\tfrac{\phi}{2}\right]\sin^2\left[\tfrac{\phi}{2}\right]b_x^2 \times \\ &[\cos\phi[5\cos\phi - 3][\tilde{P}^3(0)\tilde{P}(\tau) + \tilde{P}(0)\tilde{P}^3(\tau)] + [2\cos\phi - 1]^2\tilde{P}^2(0)\tilde{P}^2(\tau)]. \end{aligned} \tag{4.35}$$

The first term in the brackets in Eq. (4.34) is responsible for a one-phonon process, and the rest for two-phonon processes. We note that in the numerical calculations in this work we neglected terms of the type $\tilde{P}^3(0)\tilde{P}(\tau)$ and $\tilde{P}(0)\tilde{P}^3(\tau)$. The relaxation mechanism that results from these terms can be interpreted as a higher-order correction to the standard one-phonon process. In the presence of phonons which are neither absorbed nor emitted, one phonon matches the Zeeman energy and ensures energy conservation. Furthermore, analogous to the standard terms of a one-phonon process, such terms do not contribute to dephasing at all [138].

The coefficient of $\tilde{P}^2(0)\tilde{P}^2(\tau)$ in Eq. (4.34) is more than 1000 times larger than the coefficient of the same term in Eq. (4.35) for the parameter values we used for Fig. 4.3. This suggests that two-phonon-based dephasing is negligibly small compared to two-phonon-based relaxation, and explains why in Fig. 4.3 we have $T_2 \simeq 2T_1$. Qualitatively, the presented relaxation via two-phonon processes can be understood as follows. At the anticrossing, the eigenstates of the qubit Hamiltonian are approximately $\left[|(0,2)S'\rangle \pm |(1,1)T_-\rangle\right]/\sqrt{2}$. Two-phonon Raman processes [112, 113, 114, 115] based on the singlet states of the biased DQD [138, 145] efficiently shift the energy of $|(0,2)S'\rangle$, which corresponds to a transverse coupling in the qubit subspace and therefore leads to relaxation.

From Eqs. (4.34) and (4.35) it is evident that the dephasing part depends on b_x strongly, whereas for relaxation b_x enters only with Δ_{ST} in $J^{+}_{\tilde{x}\tilde{x}}(\Delta_{ST})$. The explicit expressions for $\int_{-\infty}^{\infty} \cos(\Delta_{ST}\tau/\hbar)\langle\tilde{P}^2(0)\tilde{P}^2(\tau)\rangle d\tau$ show that Δ_{ST} enters in the dominating terms as $q + \Delta_{ST}/(\hbar v_l)$, where $\hbar q$ is the momentum of a phonon. The integrals over q (continuum limit) can simply be performed from 0 to ∞ and converge because of Bose-Einstein terms or because of the Gaussian terms that result when integrating out the spatial dependence of the electron wave functions combined with oscillations of type $e^{i\boldsymbol{q}\cdot\boldsymbol{r}}$. We note that these Gaussian terms have decayed when the phonon wavelength is (much) smaller than the size of a QD [86, 89, 95]. The main contribution to the rates is provided by the part of the integrals with $q \gg \Delta_{ST}/(\hbar v_l)$ within the range of parameters used for Figs. 4.3 and 4.5. Therefore, for the two-phonon relaxation process, the effect of b_x is negligible, which is seen in Fig. 4.6.

The qubit based on $|(1,1)T'_-\rangle$-$|(1,1)S'\rangle$

Now let us consider the case where the qubit is based on the anticrossing $|(1,1)T'_-\rangle$-$|(1,1)S'\rangle$, as shown in Fig. 4.2. For this, we plot the temperature dependence of T_1 and T_2 (see Fig. 4.9) using the following parameters:

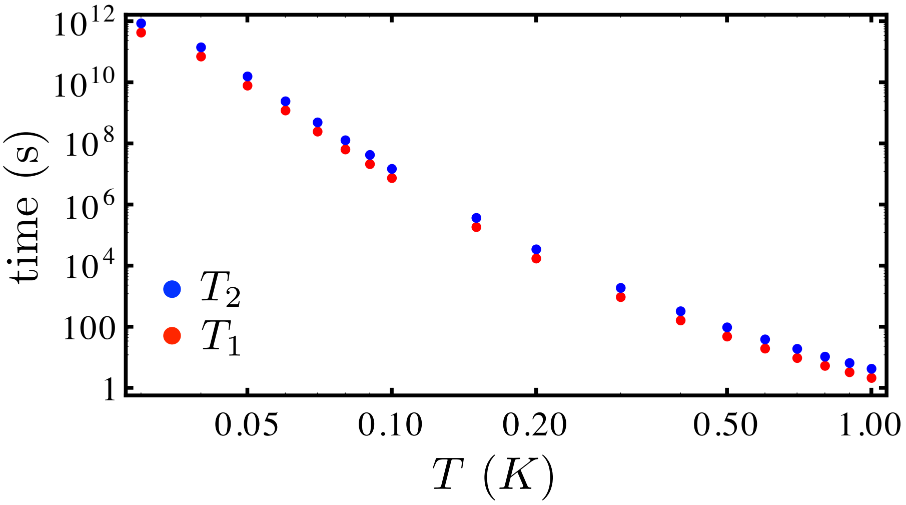

Figure 4.9: The dependence of relaxation time T_1 (red) and T_2 (blue) on temperature. The anticrossing is between $|(1,1)T'_-\rangle$ and $|(1,1)S'\rangle$. For the parameters, see text.

$B = 4.5$ mT, $t = 10$ μeV, $V_+ = 40$ μeV, $V_- = 39.99$ μeV, $U = 1.2$ meV, $b_x = 0.1$ μeV, $L = 150$ nm, $l_c = 42.7$ nm, $\epsilon = 0.68737$ meV. We see that again $T_2 \simeq 2T_1$. In Fig. 4.10 we plotted the dependence of Γ_2^{1p} and Γ_2^{2p} on temperature. The transition where the two-phonon process starts to dominate over the one-phonon process is now at lower temperature than for the case plotted in Fig. 4.4. We note that at 0.03 K $< T < 0.08$ K the power-law for the two-phonon process rate is $\Gamma_2^{2p} \propto C_5 + C_6 T^{10}$, where C_5, C_6 are constants.

Remarkably, from Fig. 4.9 it follows that phonon-induced relaxation and decoherence are extremely slow. However, as we noted before, we neglected the effect of SOI in this calculation. When b_x is very small, it can be that SOI effects are noticeable. Let us assume there is Rashba SOI in our sample. Then, for the values of b_x, E_Z, L, and l_c we use in this subsection, the Rashba SOI length must be $l_R \simeq 1.6$ μm for 2Ω to be of the same absolute value as b_x. We note that in GaAs/AlGaAs heterostructures l_R of the order of 1 μm has been reported [105]. Although we are not aware of precise data for SOI in Si/SiGe-based QDs, we expect it to be weaker (l_R longer) than in GaAs/AlGaAs.

We note that the $|(1,1)T'_-\rangle$-$|(1,1)S'\rangle$-type qubit is also robust against charge noise, because the qubit is operated at the "sweet spot", where

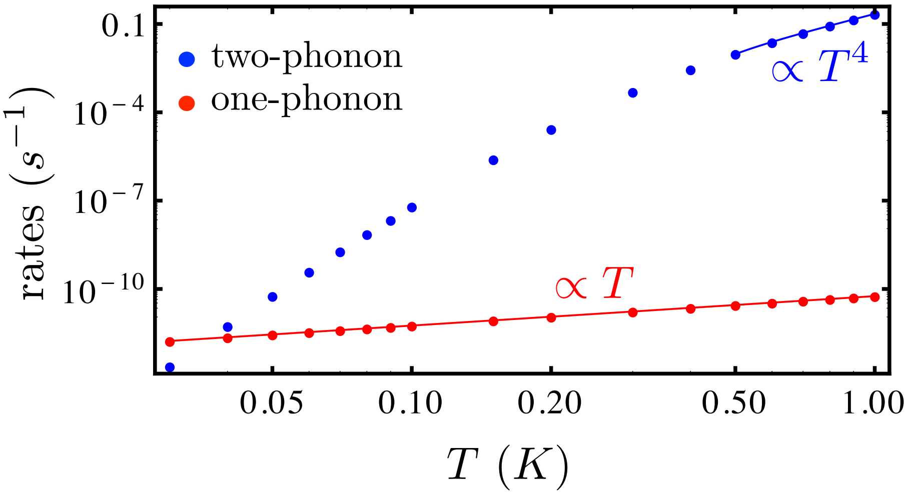

Figure 4.10: The dependence of one-phonon (Γ_2^{1p}) and two-phonon (Γ_2^{2p}) components of the decoherence rate on temperature. The anticrossing is between $|(1,1)T'_-\rangle$ and $|(1,1)S'\rangle$. The parameters are the same as in Fig. 4.9 and are listed in the text.

$\partial\Delta_{ST}/\partial\epsilon \simeq 0$, and the anticrossing region is wide [137].

4.4 S-T_0 qubit

In this section we consider the qubit based on $|(1,1)S'\rangle$-$|(1,1)T'_0\rangle$. There are two cases which we are interested in. The first one is the region of large detuning, where $|(0,2)S'\rangle$ is close to the qubit subspace. The second one is the zero-detuning case, where we have to take excited orbital states into account. We already considered these cases in our previous work on DQDs in GaAs/AlGaAs heterostructures, Ref. [138]. Here we consider a DQD in a SiGe/Si/SiGe quantum well and present the dependence of T_1 and T_2 on different quantities which were not studied in our previous work.

Large detuning

In this subsection we consider the region near the anticrossing of $|(1,1)S'\rangle$ and $|(0,2)S'\rangle$, where the state $|(0,2)S'\rangle$ is sufficiently closer to the qubit subspace than states with excited orbital parts, so that the latter can be omitted. We use the Hamiltonian from Eq. (4.9) and calculate T_1 and T_2 using the theory described in Sec. 4.2. At the end of this subsection we present a simple analytic model and discuss our numerical results.

Dependence on the applied magnetic field gradient

We study the dependence of T_1 and T_2 on the energy b_B associated with the magnetic field gradient. For Fig. 4.11 we used $B = 0.4$ T, $t = 4$ μeV, $V_+ = 40$ μeV, $V_- = 39.99$ μeV, $U = 1.2$ meV, $b_x = 0$, $L = 150$ nm, $l_c = 42.7$ nm, and $\epsilon = 1.144$ meV. The chosen confinement length corresponds to the level splitting $\Delta E = 200$ μeV, which allows us to neglect the effect of the excited states compared to $|(0,2)S'\rangle$ due to the large energy gap. As we took $b_x = 0$, we consider non-zero Rashba SOI. The Rashba SOI length we use is quite short, $l_R = 2$ μm, and we take $\eta = 0$ to make the effect of SOI maximal [see Eq. (4.13)], resulting in $\Omega = -3.48$ μeV. However, our numerical calculation showed that the effect of SOI in this regime of large detuning, even with a rather small l_R and $\eta = 0$, is negligible. For the parameters described above the resulting Δ_{ST} is in the range 1.8 μeV $< \Delta_{ST} < 2.6$ μeV.

From Fig. 4.11 we see that the behavior of T_1 and T_2 is similar at $T = 100$ mK and $T = 500$ mK. We note that in contrast to our previous work for GaAs QDs[138], the relation $T_\varphi \ll T_1$ does not hold for the whole range of parameters. For $b_B < 0.8$ μeV the pure dephasing part T_φ dominates over T_1, bringing T_2 to much lower values than T_1. However, as the magnetic field gradient enhances relaxation processes strongly, T_1 decays rapidly with b_B, becoming of the order of T_2 and even $T_1 < T_2$ for $b_B > 1.6$ μeV. The strong dependence of relaxation on b_B is easy to understand from the Hamiltonian [Eq. (4.9)], because $b_B/2$ is the off-diagonal term between $|(1,1)S\rangle$ and $|(1,1)T_0\rangle$ and the only term that connects $|(1,1)T_0\rangle$ to other states. This means that relaxation occurs only in case $b_B \neq 0$ and strongly depends on the value of b_B. We obtain $T_1 \propto b_B^{-2}$ for $b_B < 1$ μeV in Fig. 4.11 (both a and b).

Dependence on temperature

We also plot the temperature dependence of T_1 and T_2 (Fig. 4.12). For this plot we used $b_B = -1$ μeV and otherwise the same parameters as for Fig. 4.11. The splitting between the qubit states $|(1,1)S'\rangle$ and $|(1,1)T_0'\rangle$ is $\Delta_{ST} \simeq 2$ μeV. From Fig. 4.12 we see that both T_2 and T_1, as expected,

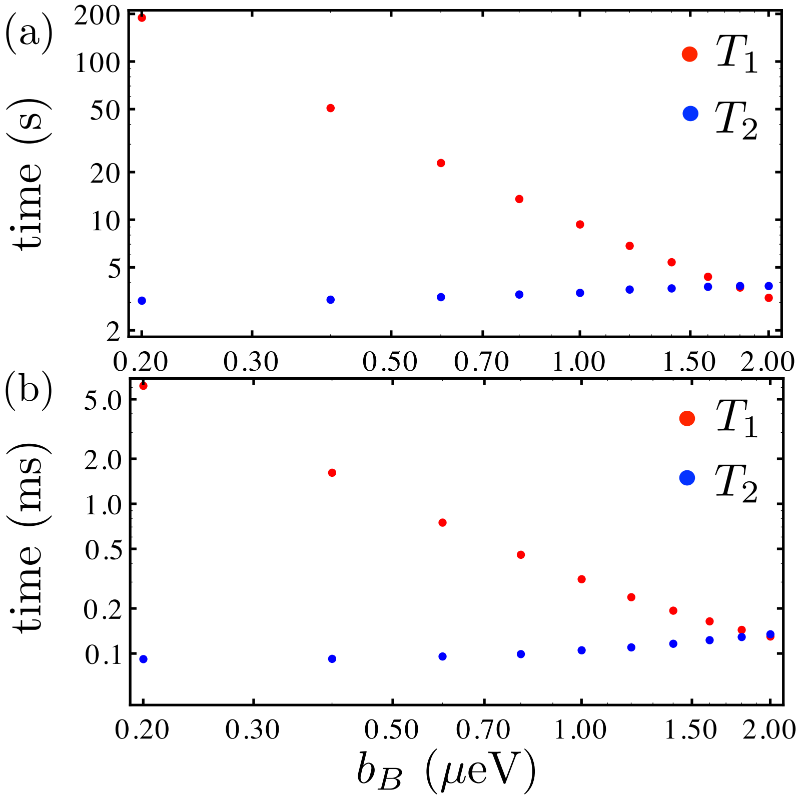

Figure 4.11: (a) The dependence of T_1 (red) and T_2 (blue) on b_B for a S-T_0 qubit at large detuning. The temperature is $T = 100\,\mathrm{mK}$. The decoherence time T_2 is slightly increasing (except for the last point) with increasing b_B, whereas the relaxation time decreases drastically. (b) The same dependence as in (a), but at $T = 500\,\mathrm{mK}$. Other parameters are given in the text.

decrease with temperature. At very low temperatures, i.e., $T < 0.06\,\mathrm{K}$, $T_2 > T_1$, however, then T_2 decays faster than T_1. For $0.5\,\mathrm{K} \leq T \leq 1\,\mathrm{K}$, their power-laws are the same, $\propto T^{-4}$.

To understand why T_2 (similarly for T_1) decays so slowly for $T < 0.06\,\mathrm{K}$ and then faster, we plot the temperature dependence of Γ_2^{1p} and Γ_2^{2p} (see Fig. 4.13). Here we see that for $T \leq 0.05\,\mathrm{K}$ the one-phonon process dominates and $\Gamma_2^{1p} \propto T$, which gives a slow decay of T_1 and T_2 with temperature. The origin of this dependence of Γ_2^{1p} is the same as the one explained in Sec. 4.3. For temperatures $T \geq 0.1\,\mathrm{K}$ the two-phonon process dominates. Therefore, as $\Gamma_2^{2p} \propto T^4$ for $0.5\,\mathrm{K} \leq T \leq 1\,\mathrm{K}$, we see

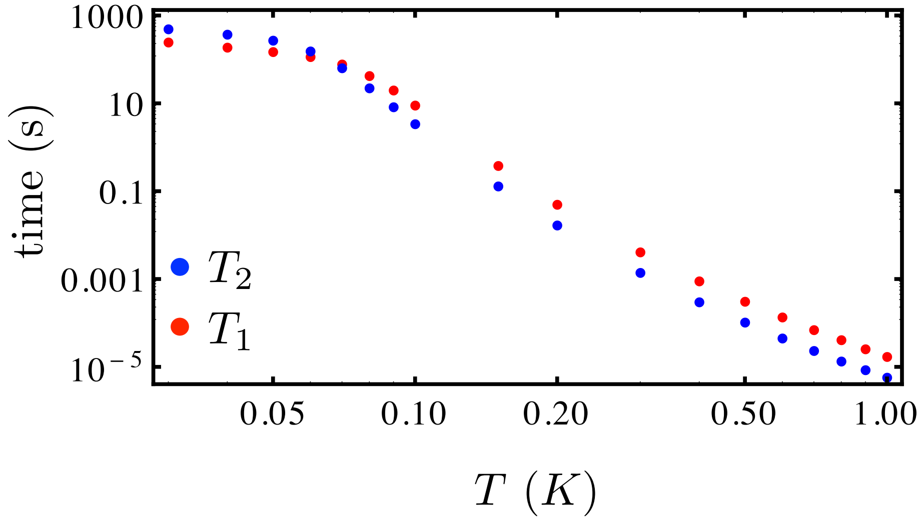

Figure 4.12: The dependence of T_2 (blue) and T_1 (red) on temperature T for a S-T_0 qubit at large detuning ϵ.

the same power-law for $1/T_2$. With a similar analysis for T_1, we find that for 0.5 K $\leq T \leq 1$ K also $1/T_1 \propto T^4$ due to two-phonon processes. Since we have a rather large b_B, the dephasing part T_φ is of the same order as T_1, as was shown in Sec. 4.4. The reason for choosing here a large b_B are the reported values for applied magnetic field gradients in experiments with micromagnets [15, 16, 17, 18].

Dependence on detuning

Here we show that in the anticrossing region even small changes of ϵ affect both T_1 and T_2 strongly. Therefore we present the dependence of T_1 and T_2 on ϵ, see Fig. 4.14, where we used the same parameters as for Fig. 4.11 and took $b_B = -1$ μeV and $T = 100$ mK. In the range of ϵ shown in Fig. 4.14 the splitting Δ_{ST} takes values in the range 1.3 μeV $< \Delta_{ST} <$ 2.7 μeV. We see that even though the change of ϵ is only 30 μeV, the relaxation time and decoherence time both change drastically. The main reason for this behavior is that in this region $|(0,2)S'\rangle$ very quickly drops in energy with ϵ and hence comes closer to the qubit subspace.

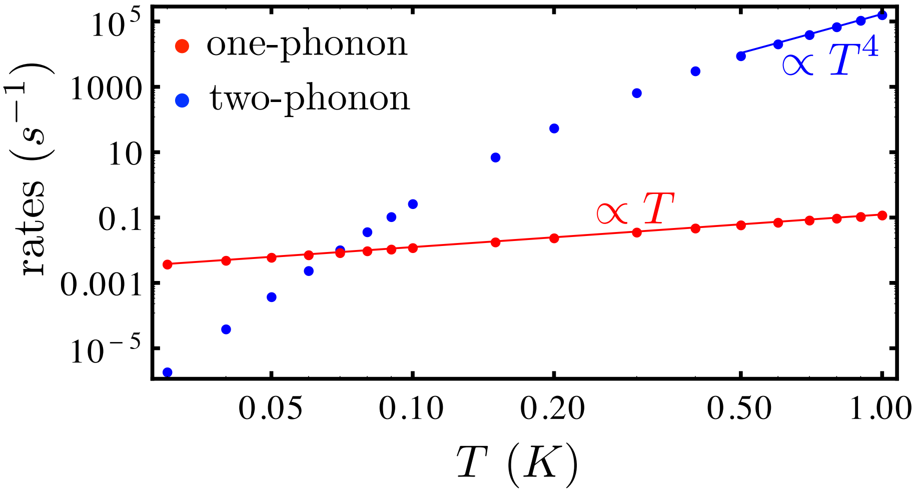

Figure 4.13: The dependence of one-phonon (Γ_2^{1p}) and two-phonon (Γ_2^{2p}) components of the decoherence rate on temperature T. The parameters are the same as for Fig. 4.12 and are provided in the text.

Dependence on tunnel coupling

To find the optimal regime for qubit operation we present the dependence of T_1 and T_2 on the tunnel coupling t between the dots, see Fig. 4.15. For this calculation we used $b_B = -1$ μeV and the other parameters as for Fig. 4.11. The S-T_0 splitting changed with 3 μeV $< t < 8$ μeV in the interval 1.4 μeV $< \Delta_{ST} < 5.9$ μeV. For Fig. 4.15a we used $T = 100$ mK and for Fig. 4.15b $T = 500$ mK.

From Fig. 4.15a we see that both T_1 and T_2 decay with t, however, the forms of their decays are different. The decay of T_2 is close to the power-law $T_2 \propto C_7 + C_8 t^{-4}$, where C_7 and C_8 are constants (the blue line in Fig. 4.15a). In Fig. 4.15b we see that T_2 decays with t. However, T_1 grows with t for $t > 4$ μeV.

To understand this behavior of T_1 we plot the dependence of relaxation rates due to one-phonon (Γ_1^{1p}) and two-phonon processes (Γ_1^{2p}) on t again for 100 mK and 500 mK (see Fig. 4.16). The rates satisfy

$$1/T_1 \equiv \Gamma_1 = \Gamma_1^{1p} + \Gamma_1^{2p}. \tag{4.36}$$

In both Figs. 4.16a (100 mK) and 4.16b (500 mK) the one-phonon rate grows with t, whereas the two-phonon rate slowly decays at $t > 4$ μeV.

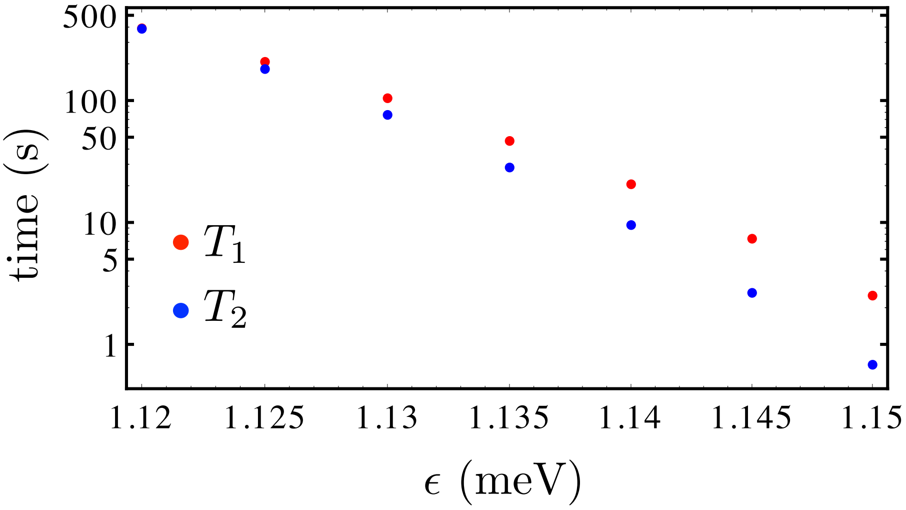

Figure 4.14: The dependence of T_1 (red) and T_2 (blue) on detuning ϵ for a S-T_0 qubit at $T = 100$ mK. Details are described in the text.

The difference in behavior of T_1 in Figs. 4.15 a and b arises from the fact that for the lower temperature, i.e., 100 mK, for $t \geq 6$ μeV the one-phonon relaxation rate dominates, which makes T_1 decrease with t. However, at larger temperature, $T = 500$ mK, the two-phonon process starts to dominate (see Fig. 4.16b), which makes T_1 grow with t.

Simple model for the S-T_0 qubit at large detuning

To understand the dependences on different parameters presented above, we consider a simple model. Similarly to the simple model of Ref. [138], we consider the Hamiltonian

$$\tilde{H} = \begin{pmatrix} 0 & \frac{b_B}{2} & 0 \\ \frac{b_B}{2} & V_+ - V_- & -\sqrt{2}t \\ 0 & -\sqrt{2}t & -\epsilon + U - V_- + \tilde{P} \end{pmatrix} + H_{ph} \qquad (4.37)$$

in the basis $|(1,1)T_0\rangle$, $|(1,1)S\rangle$, and $|(0,2)S\rangle$, because the effect of $|(0,2)S\rangle$ on the qubit lifetimes is dominating. Here $\tilde{P} = P_{SR} - P_T$, and we note that the electron-phonon interaction matrix elements P_S and $P_S^\dagger$ have a negligible effect on T_1 and T_2 and were therefore omitted. To separate

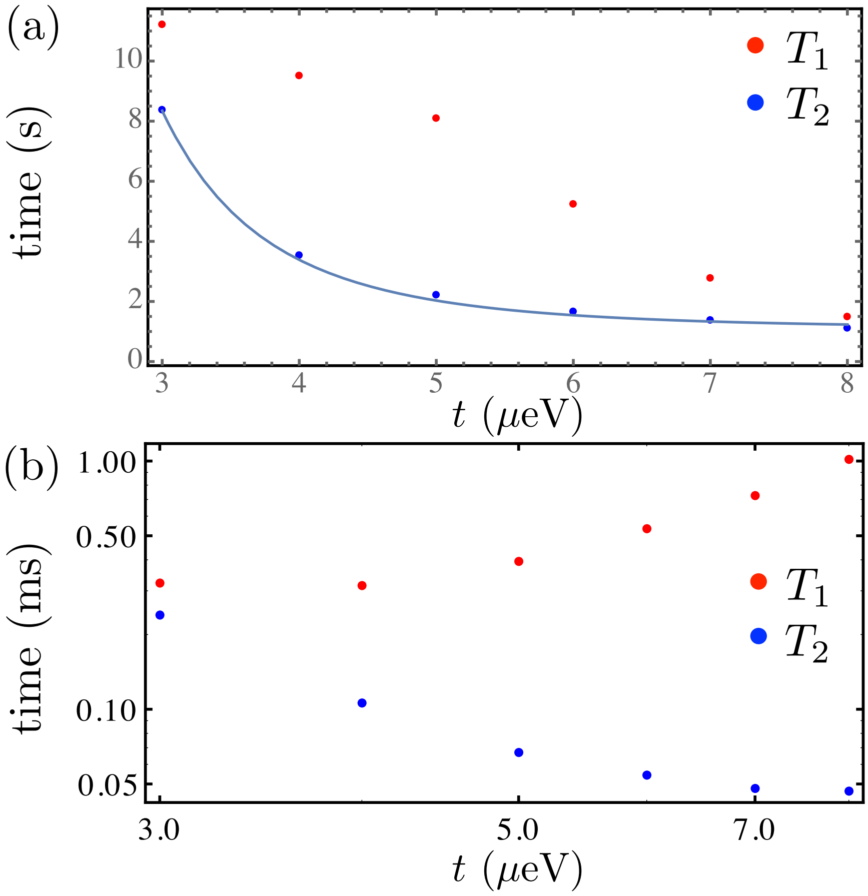

Figure 4.15: (a) The dependence of T_2 (blue) and T_1 (red) on the tunnel coupling t for an S-T_0 qubit in a biased DQD. Here the temperature is 100 mK, for the other parameters see text. The blue line shows the power-law $C_7 + C_8 t^{-4}$. Both T_1 and T_2 decay with t. (b) The same dependence as in (a), but at a higher temperature $T = 500$ mK. Here we see that T_1 grows with t in contrast to (a).

the qubit subspace from $|(0,2)S\rangle$, we perform a second-order Schrieffer-Wolff transformation assuming that $|t|$ and $\tilde{P}$ are small compared to $U - \epsilon - V_+ - |b_B|/2$. Then we apply a unitary transformation to the resulting 2×2 Hamiltonian that diagonalizes the phonon-independent part, as it was done in Sec. 4.3. Consequently, the $\delta B_{\tilde{x}}$ and $\delta B_{\tilde{z}}$ that we derive from the qubit Hamiltonian characterize T_1 and T_φ, respectively [see Eqs. (4.16)–(4.18)]. The parameters we use for our calculation allow us to

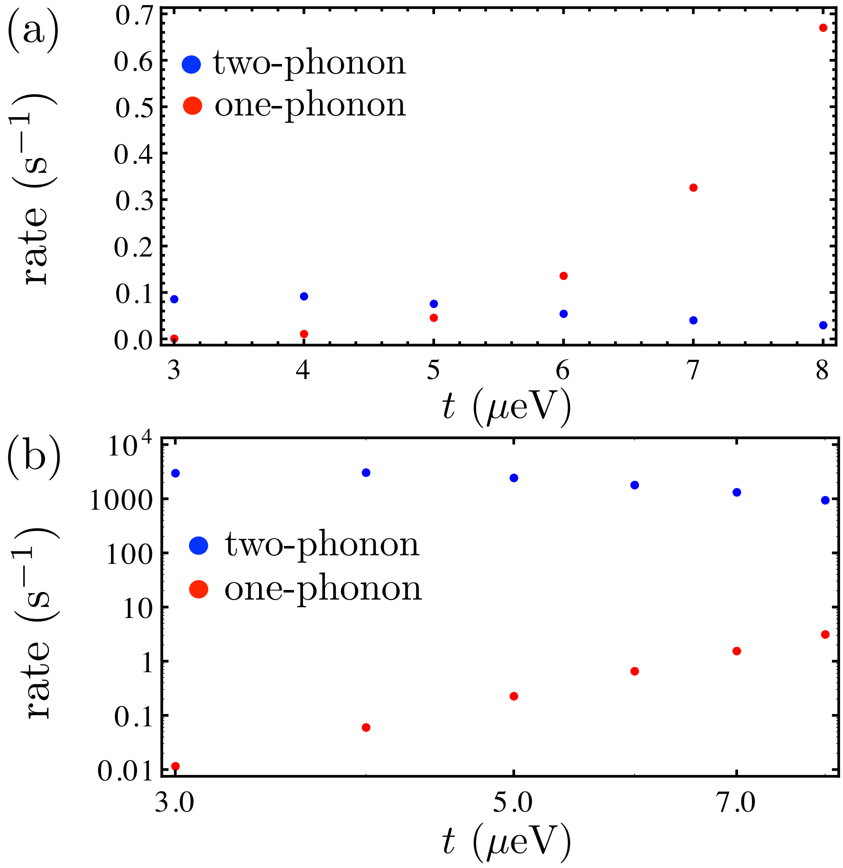

Figure 4.16: (a) The dependence of relaxation rates due to one-phonon processes (Γ_1^{1p}) and two-phonon processes (Γ_1^{2p}) on the tunnel coupling t. Here the temperature is 100 mK. (b) The same dependence as in (a), but the temperature for this plot is $T = 500$ mK. The parameters are the same as for Fig. 4.15.

assume $V_+ \simeq V_-$ and simplify the expressions for $\delta B_{\tilde{x}}$ and $\delta B_{\tilde{z}}$ as follows:

$$\begin{aligned}\delta B_{\tilde{x}}(\tau) &\simeq \frac{1}{G_6}\left[\frac{b_B t^2(b_B^2 t^2 + 2(t^2 G_5^2 + G_5^4 - 4t^4))}{2G_5}\tilde{P}(\tau)\right.\\ &\left. -b_B t^2(G_5^2 - t^2)\tilde{P}^2(\tau)\right], \qquad (4.38)\\ \delta B_{\tilde{z}}(\tau) &\simeq \left[t^2 G_5[4t^2(2t^2 - G_5^2) + b_B^2(2G_5^2 - 3t^2)]\tilde{P}(\tau)\right.\\ &\left. +t^4[b_B^2 + 4(G_5^2 - 2t^2)]\tilde{P}^2(\tau)\right]\frac{1}{2G_5 G_6}, \qquad (4.39)\end{aligned}$$

where we introduced

$$\begin{aligned} G_5 &= U - V_+ - \epsilon, & (4.40) \\ G_6 &= G_5^3 \sqrt{b_B^2 (t^2 - G_5^2)^2 + \frac{t^4 (b_B^2 - 8t^2 + 4G_5^2)^2}{4G_5^2}}. & (4.41) \end{aligned}$$

Using these expressions, we will now discuss the numerical data shown in Sec. 4.4. As a first example, we start with the remarkable decay of T_1 by two orders of magnitude seen in Fig. 4.11. In the dependence of T_1 on b_B the two-phonon process is dominating, especially for smaller b_B and larger temperature (for $b_B = 2\ \mu\text{eV}$ and $T = 100$ mK, $\Gamma_1^{2p}/\Gamma_1^{1p} \simeq 2.7$). To analyze this dependence we therefore consider only two-phonon process terms in $\delta B_{\tilde{x}}$, i.e., the prefactor before $\tilde{P}(\tau)^2$. From Eq. (4.38), we see that the numerator of the prefactor is linear in b_B. The denominator is also a function of b_B, however it is of the form $\sqrt{C_9 b_B^4 + C_{10} b_B^2 + C_{11}}$, where C_9, C_{10}, and C_{11} are constants. Consequently, the power-law $T_1 \propto b_B^{-2}$ holds very well for $b_B < 1\ \mu\text{eV}$ and slightly deviates for larger b_B.

The dependence of T_1 on the detuning ϵ plotted in Fig. 4.14 is more complicated. Our numerical calculations show that in this case the two-phonon process again dominates. To understand the detuning-dependence of T_1 we therefore study the prefactor before $\tilde{P}^2(\tau)$ again. For the range of ϵ presented in Fig. 4.14, the dependence of this prefactor on ϵ is approximately of the type $(U - V_+ - \epsilon)^{-3}$, and consequently $T_1 \propto (U - V_+ - \epsilon)^6$.

The dependence on the tunnel coupling t is very complex. As we see from Figs. 4.15 and 4.16, both one- and two-phonon processes contribute significantly to T_1 and T_2. However, Eqs. (4.38) and (4.39) can be greatly simplified when focusing on certain regimes. For example, we see from Fig. 4.16 that the two-phonon process dominates in T_1 for $T = 500$ mK. If we consider the prefactor before $\tilde{P}^2(\tau)$, we find that the dependence on t is indeed negligible for $t < 7\ \mu\text{eV}$, as seen for Γ_1^{2p} in Fig. 4.16.

Zero detuning

For the case of zero detuning, i.e., $\epsilon \simeq 0$, we have to take into account the first excited orbital states. We will therefore consider our Hamiltonian in the basis $|(1,1)S\rangle$, $|(1,1)T_0\rangle$, $|(1,1)T_+\rangle$, $|(1,1)T_-\rangle$, $|(1^*,1)S\rangle$, $|(1^*,1)T_+\rangle$, $|(1^*,1)T_0\rangle$, $|(1^*,1)T_-\rangle$, where the asterisk indicates that the electron in the QD is in the first excited state [138],

$$\widetilde{H} = \begin{pmatrix} -J_S + P_{SS} & \frac{b_B}{2} & \frac{\Omega}{\sqrt{2}} & -\frac{\Omega}{\sqrt{2}} & P^e_{cr} & \frac{\Omega_1}{\sqrt{2}} & 0 & -\frac{\Omega_1}{\sqrt{2}} \\ \frac{b_B}{2} & P_T & 0 & 0 & 0 & -\frac{\Omega_1}{\sqrt{2}} & P^e_{cr} & -\frac{\Omega_1}{\sqrt{2}} \\ \frac{\Omega}{\sqrt{2}} & 0 & E_Z + P_T & 0 & \frac{\Omega_1}{\sqrt{2}} & P^e_{cr} & -\frac{\Omega_1}{\sqrt{2}} & 0 \\ -\frac{\Omega}{\sqrt{2}} & 0 & 0 & -E_Z + P_T & -\frac{\Omega_1}{\sqrt{2}} & 0 & -\frac{\Omega_1}{\sqrt{2}} & P^e_{cr} \\ P^{e\dagger}_{cr} & 0 & \frac{\Omega_1}{\sqrt{2}} & -\frac{\Omega_1}{\sqrt{2}} & \Delta E + P^e & \frac{\Omega_2}{\sqrt{2}} & 0 & -\frac{\Omega_2}{\sqrt{2}} \\ \frac{\Omega_1}{\sqrt{2}} & -\frac{\Omega_1}{\sqrt{2}} & P^{e\dagger}_{cr} & 0 & \frac{\Omega_2}{\sqrt{2}} & \Delta E + E_Z + P^e & -\frac{\Omega_3}{\sqrt{2}} & 0 \\ 0 & P^{e\dagger}_{cr} & -\frac{\Omega_1}{\sqrt{2}} & -\frac{\Omega_1}{\sqrt{2}} & 0 & -\frac{\Omega_3}{\sqrt{2}} & \Delta E + P^e & -\frac{\Omega_3}{\sqrt{2}} \\ -\frac{\Omega_1}{\sqrt{2}} & -\frac{\Omega_1}{\sqrt{2}} & 0 & P^{e\dagger}_{cr} & -\frac{\Omega_2}{\sqrt{2}} & 0 & -\frac{\Omega_3}{\sqrt{2}} & \Delta E - E_Z + P^e \end{pmatrix} + H_{\text{ph}}. \tag{4.42}$$

Here, the splitting J_S takes into account the hybridization of $|(0,2)S\rangle$ and $|(2,0)S\rangle$ with $|(1,1)S\rangle$ and is defined as

$$J_S = \frac{1}{2}(\sqrt{16t^2 + (U - V_+)^2} - U - V_+ + 2V_-). \tag{4.43}$$

The matrix elements P^e, P^e_{cr}, $P^{e\dagger}_{cr}$ result from the electron-phonon interaction in the same way as was shown in Sec. 4.2, but for the corresponding excited states. The matrix element P_{SS} is a linear combination of electron-phonon interaction matrix elements including the effect of $|(2,0)S\rangle$ and $|(0,2)S\rangle$. The terms $\Omega_1, \Omega_2, \Omega_3$ arise from SOI. The derivation of all these matrix elements is described in detail in Ref. [138], Appendix C.

We then perform an initial unitary transformation, followed by a Schrieffer-Wolff transformation, and apply Bloch-Redfield theory as described in Sec. 4.2 and plot the temperature dependence of T_1 and T_2, see Fig. 4.17. Here we take $B = 0.4$ T, $t = 24$ μeV, $U = 1.2$ meV, $V_+ = 50$ μeV, $V_- = 49.5$ μeV, $\Delta E = 200$ μeV, $L = 150$ nm, $l_R = 2$ μm, and $b_B = -1$ μeV. Consequently, $J_S = 1.5$ μeV and $\Delta_{ST} = 2.5$ μeV. Comparing Fig. 4.17 with Fig. 4.12 we see that the qubit lifetimes are several orders of magnitude longer than in the case of large detuning. This makes the zero detuning regime favorable for S-T_0 qubits, which was also shown for DQDs in GaAs/AlGaAs in our previous work [138].

The calculations for Fig. 4.17 were done with the orbital excitation along the axis that connects the QDs. The decay rates resulting from excitation along the orthogonal direction do not change the qualitative picture, which is sufficient for our consideration. For Fig. 4.17 we chose $\eta = 0$. If we take $\eta = \pi/2$, the rates are either smaller or of the same order as for $\eta = 0$. States of type $(1,1^*)$ with the excited electron in the right QD will change the results only by factors around 2, and therefore were not included for simplicity.

The valley degrees of freedom were neglected in our model because valley splittings around 1 meV were already realized experimentally [82, 83, 84], which is a large gap compared to the orbital level spacing $\Delta E = 200$ μeV. While valley-related effects are strongly suppressed when the valley splitting is large, we note that they can be a significant source of decoherence when the splitting is small [80, 132, 146]. Therefore, setups with a large valley splitting are usually favorable when implementing spin qubits in Si/SiGe heterostructures, which is the case that we focus on in this work.

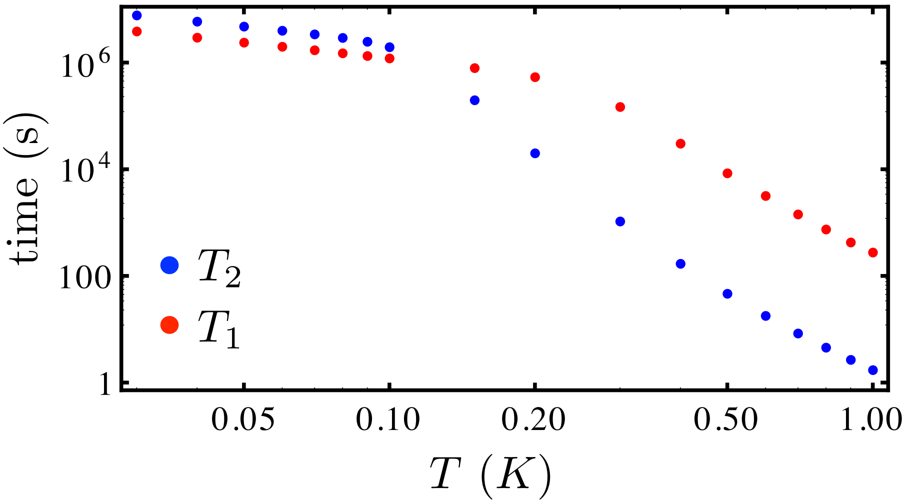

Figure 4.17: The dependence of T_2 and T_1 of a S-T_0 qubit on temperature for the unbiased case $\epsilon \simeq 0$. The parameters are provided in Sec. 4.4.

4.5 Comparison with other decay mechanisms

In our previous calculations for S-T_0 qubits in GaAs DQDs [138], we found that the considered one- and two-phonon processes may very well correspond to the dominant decay channels in an experiment. In contrast, for the Si DQDs studied here, the obtained decay times for singlet-triplet qubits are relatively long, at least for many parameter regimes, and so it is well possible that the experimentally feasible qubit lifetimes will be limited by other mechanisms, some of which we briefly discuss below. Nevertheless, even if other mechanisms turn out to dominate in standard regimes, we identified and proposed ways how our theory can be confirmed experimentally, which would be a desirable contribution to understanding and assessing the role of the discussed one- and two-phonon processes in these Si-based systems.

Among the most relevant noise sources for electrically controllable qubits is charge noise [10, 147, 148], which may be due to charge traps within the heterostructure or noise from the gates. For instance, electrical noise was considered as a major obstacle for the implementation of high-quality two-qubit gates between S-T_0 qubits in GaAs [53]. Theoretical studies suggest that the effects of charge noise in GaAs and Si are similar to a great extent [149, 150]. As evident from, e.g., the pure-dephasing model discussed in Ref. [151], the resulting decay will depend both on the spectral density of the noisy fluctuations in the level splitting of the qubit and on the details of the operation scheme, as suitable pulse sequences for dynamical decoupling may strongly prolong the dephasing time [5, 8, 46, 53, 152, 153]. Furthermore, decoherence due to charge noise can be much suppressed by operating the qubit at a sweet spot, where the level splitting of the qubit is insensitive to electric field fluctuations. This is a particularly advantageous feature of S-T_0 qubits in unbiased DQDs [59, 154] and S-T_- qubits (especially those based on $|(1,1)T'_-\rangle$-$|(1,1)S'\rangle$, see Sec. 4.3) operated at the anticrossing [137].

While we considered here the Bloch-Redfield theory and studied the phonon-assisted relaxation and decoherence that results from one- and two-phonon processes, such as the two-phonon Raman process [112, 113, 114, 115, 145], a spin-boson model was adopted in Ref. [155] in order to describe pure dephasing of S-T_0 qubits in the absence of any real or virtual phonon absorption or emission. In the calculations of Ref. [155], interactions between the electrons and a dissipative phonon reservoir lead to an exponential decay of the qubit coherence, and the associated dephasing time depends strongly on the overlap of the electron wave functions and the decay properties of the phonon bath. In contrast to our model, where the qubit lifetimes in GaAs turned out to be limited by the piezoelectric electron-phonon coupling [138], the lifetimes calculated in Ref. [155] for both Si and GaAs are limited by the deformation potential coupling. Depending on the experimental setup this additional decay channel might dominate, particularly for strongly overlapping quantum dots in Si, and it can be suppressed by moving the two dots farther apart [155].

As mentioned before in Sec. 4.4, valley-related effects can become an important source of decoherence if the energy splitting between valleys is not sufficiently large[80, 132, 146]. Among other things, disorder or interface effects for Si/SiGe and Si/SiO$_2$ can play a significant role here [80, 146, 156, 157, 158, 159]. When the valley splitting is large, however, qubit decoherence due to the valley degrees of freedom is suppressed, and splittings of the order of 1 meV or even more are experimentally feasible [81, 82, 83, 84, 160].

Finally, the coherence of qubits in Si/SiGe heterostructures can be lost due to interaction with the nuclear spins, although the hyperfine-induced dephasing time of 360 ns (no echo pulses) reported for a Si DQD [117] is already one to two orders of magnitude longer than the typical values for GaAs [5, 42, 43, 44]. Ultimately, however, the hyperfine coupling will not present a limiting factor for the qubit lifetimes, since Si and Ge can be grown nuclear-spin-free.

4.6 Conclusions

We considered S-T_- qubits in the anticrossing region for the two cases where the singlet is mainly $|(0,2)S\rangle$ and where it is mainly $|(1,1)S\rangle$. In the latter case, T_1 and T_2 turned out to be much longer than in the former one. We showed that the magnetic field gradient reduces T_1 and T_2 substantially, when it is above a certain value at which the one-phonon process starts to dominate over the two-phonon process. This follows from the fact that the magnetic field gradient provides the splitting in the anticrossing, and therefore the one-phonon process is very sensitive to its change. In contrast, two-phonon-based relaxation does not change noticeably in the range of parameters we use, and two-phonon-based dephasing is very weak even though it does depend on the magnetic field gradient. We proposed regimes where our theory of one- and two-phonon processes may be experimentally tested. Remarkably, T_2 (T_1) has a peak (dip) at the center of the S-T_- anticrossing in the dependence on the applied magnetic field (Fig. 4.8). As the external magnetic field can easily be changed in an experiment, this peak (dip) might be an experimental indication of the center of the anticrossing, which is a regime of interest e.g. for Refs. [15, 137].

We also studied S-T_0 qubits in the regimes which were presented in our previous work on DQDs in GaAs/AlGaAs [138], i.e., at large detuning in the anticrossing region of the singlets and at zero detuning. The key result that small detuning is much more favorable regarding the qubit lifetimes than large detuning is valid here too. We showed that in the anticrossing region even small changes in ϵ may shorten T_1 and T_2 by two orders of magnitude. We note that the relation $T_\varphi \ll T_1$, shown in our previous work for the regime of large detuning, does not hold for the usual parameters of experiments with SiGe/Si/SiGe DQDs because of a rather large applied magnetic field gradient. We showed that the magnetic field gradient can reduce T_1 by orders of magnitude. We demonstrated that the dependence of T_1 on tunnel coupling is qualitatively different for different temperatures, which is explained by the behavior of one- and two-phonon processes. Our study of the effect of various system parameters on T_1 and T_2 shows ways how to prolong the phonon-based decoherence and relaxation times by orders of magnitude.

4.7 Acknowledgments

We thank S. Chesi, T. Otsuka, and K. Takeda for helpful discussions and acknowledge support from the Swiss NF, NCCR QSIT, SiSPIN, and IARPA.

4.A Diagonalization of the Hamiltonian in the S-T_- basis

To diagonalize the part of the Hamiltonian that does not contain phonons after the Schrieffer-Wolff transformation in Sec. 4.3, we use a unitary transformation

$$U_2 = \begin{pmatrix} \cos(\Theta/2) & -\sin(\Theta/2) \\ \sin(\Theta/2) & \cos(\Theta/2) \end{pmatrix}, \tag{4.44}$$

where the angle Θ is defined as

$$\begin{aligned} \cos(\Theta/2) &= \frac{c}{\sqrt{c^2+d^2}}, && (4.45) \\ \sin(\Theta/2) &= \frac{d}{\sqrt{c^2+d^2}}, && (4.46) \end{aligned}$$

and

$$\begin{aligned} c &= \frac{1}{\sin\left[\frac{\phi}{2}\right]\sqrt{2}\Delta(b_x^2 - 32\Delta^2 + b_x^2\cos\phi)} \times && (4.47) \\ &\quad \left(4b_x\Delta^2(1+\cos\phi) - b_x^3\cos^2\left[\frac{\phi}{2}\right]\cos\phi + \right. \\ &\quad \left. + \sqrt{\cos^4\left[\frac{\phi}{2}\right] b_x^2(b_x^2\cos\phi - 8\Delta^2)^2 + 2\Delta^2(b_x^2 - 32\Delta^2 + b_x^2\cos\phi)^2\sin^2\left[\frac{\phi}{2}\right]}\right), \\ d &= 1. && (4.48) \end{aligned}$$

Part II

Ordered state and coherence of the localized spins in semiconductor nanowires

CHAPTER 5

Introduction

Adapted from:
Viktoriia Kornich, Peter Stano, Alexander A. Zyuzin, and Daniel Loss,
"Voltage-induced conversion of helical to uniform nuclear spin polarization in a quantum wire",
Phys. Rev. B **91**, 195423 (2015),
ArXiv:1503.06950 (2015),

Alexander A. Zyuzin, Tobias Meng, Viktoriia Kornich, and Daniel Loss
"Nuclear spin relaxation in Rashba nanowires",
Phys. Rev. B **90**, 195125 (2014),
ArXiv:1407.2582 (2015).

Magnetic structures are promising platforms for many modern devices, e.g. memory [19], sensors [161], and quantum computation hardware [38]. The opportunities to get an ordered magnetic phase in the bulk and low-dimensional systems due to Ruderman-Kittel-Kasuya-Yosida (RKKY) interaction [162, 163, 164, 165] were studied in a number of theoretical and experimental works [21, 22, 23, 24, 25, 26]. The prominent feature of RKKY interaction in 1D systems is the ordering of localized spins into a helix [1, 28].

When the current is driven through the system of electrons and nuclei, the spin polarization can be swapped between the two subsystems through the hyperfine interaction, leading to dynamic nuclear polarization effects [166, 167, 168, 169, 170, 171]. If the polarization of current carrying electrons and localized spins differ, the spin-transfer torque arises

[30, 31], important for dynamics of domain walls [172, 173] and enhancing the tilting of the spiral structure in helimagnets [174]. Closely related is the dynamic nuclear polarization, arising e.g. in helical edge states of topological insulator. The backscattering of helical electrons can be of different origins, such as assisted by phonons [175], magnetic impurities [176], or absence of axial spin symmetry [177]. It was shown that nuclear-assisted backscattering of electrons due to hyperfine interaction induces nuclear polarization when the current is driven through the edge states of topological insulator [178, 179].

The main motivation for our work comes from the recent experiment by Scheller *et al.* [29], where the conductance of a cleaved edge overgrowth GaAs quantum wire was measured. The measurements showed that the conductance of the first mode becomes e^2/h at low temperatures instead of the naively expected $2e^2/h$. This suggests the lifting of electron spin degeneracy. The possible explanation is the presence of a helical nuclear spin polarization that gaps out one subband and thus provides an electron spin selection. Further ways to confirm the presence of the nuclear spin helix were suggested theoretically, by means of nuclear magnetic resonance [180], nuclear spin relaxation [181], and quantum Hall effect anisotropies [182].

Low-dimensional condensed matter systems with strong spin-orbit interaction (SOI) have attracted much attention both theoretically [183, 184, 185, 186, 187] and experimentally [188, 189, 190, 191] for their realization of nontrivial momentum space topology [185]. A particular example of such systems are semiconducting Rashba nanowires in a helical state, in which the Rashba SOI [192], locks the spin of the electron to its direction of motion. In a Rashba nanowire, the helical state can be obtained by tuning the chemical potential into the partial gap at zero momentum induced by a magnetic field. Insulating and superconducting states of helical Rashba wires can host Jackiw-Rebbi [193, 194] and Majorana bound states around topological defects [195].

Not only as a prerequisite for the creation and identification of these exotic bound states, but also on its own right, it is important to gain information about the strength of the SOI, and to detect signatures of the helical state in nanowires. For example, the drop of the conductance of a ballistic conduction channel from $2e^2/h$ to e^2/h as a function of Fermi level can serve as an experimental probe of the helical state [1, 29, 196, 197]. Signatures of the helical state can also be found in the electron spin susceptibility [198]. So far, the SOI in nanowires has been measured only in quantum dots (via transport) [199, 200, 201], where, however, the Rashba

SOI of interest is masked by the one that is induced by the dot confinement potential.

CHAPTER 6

Voltage-induced conversion of helical to uniform nuclear spin polarization in a nanowire

Adapted from:
Viktoriia Kornich, Peter Stano, Alexander A. Zyuzin, and Daniel Loss,
"Voltage-induced conversion of helical to uniform nuclear spin polarization in a quantum wire",
Phys. Rev. B **91**, 195423 (2015),
ArXiv:1503.06950 (2015).

We study the effect of bias voltage on the nuclear spin polarization of a ballistic wire, which contains electrons and nuclei interacting via hyperfine interaction. In equilibrium, the localized nuclear spins are helically polarized due to the electron-mediated Ruderman-Kittel-Kasuya-Yosida (RKKY) interaction. Focusing here on non-equilibrium, we find that an applied bias voltage induces a uniform polarization, from both helically polarized and unpolarized spins available for spin flips. Once a macroscopic uniform polarization in the nuclei is established, the nuclear spin helix rotates with frequency proportional to the uniform polarization. The uniform nuclear spin polarization monotonically increases as a function of both voltage and temperature, reflecting a thermal activation behavior. Our predictions offer specific ways to test experimentally the presence of a nuclear spin helix polarization in semiconducting quantum wires.

6.1 Introduction

In this chapter we propose and study a complementary method to detect nuclear spin helical polarization in the wire. It is based on the effect of bias voltage applied to the wire and therefore straightforward to perform experimentally. We investigate how the bias voltage applied to the wire affects its nuclear spin polarization. We assume that at zero bias and finite temperature, nuclear spins are partially polarized into a helix due to the RKKY interaction. We find that an applied voltage induces a uniform nuclear polarization from both helical and non-polarized nuclear spins available for nuclear spin flips via electrons. Therefore, upon increasing the voltage the helical nuclear polarization drops, while the uniform polarization grows, and the total polarization grows too. For small voltages and increasing temperature, the uniform polarization grows because of thermal activation of electrons, while the helical polarization dramatically drops in magnitude. Once a macroscopic uniform polarization has developed, the remaining nuclear spin helix rotates as a whole around the axis along the uniform polarization. Since the helical polarization affects the conductance of such systems [1, 28, 29, 182], these predicted features are expected to show up in the voltage and temperature dependence of the transport currrent and thus they can be tested experimentally. Recently, cantilever-based magnetic sensing techniques have been reported which enable nuclear spin magnetometry of nanoscale objects such as the nanowires considered here [202, 203]. Such powerful techniques offer promising perspectives for direct experimental tests of the results obtained in this work.

This Chapter is organized as follows. In Sec. 6.2 we present the Hamiltonian of our model. In Sec. 6.3 we describe the properties of the electron bath. The derivation of the Bloch equation for the total nuclear spin in the wire is discussed in Sec. 6.4. The resulting nuclear spin polarization and its dependence on the parameters of the system are presented and discussed in Sec. 6.5. Our conclusions follow in Sec. 6.6. Additional information about our calculation is given in Appendix.

6.2 The model

We consider a one-dimensional electron gas and localized spins in a semiconductor nanowire. We will refer to these localized spins as nuclear spin in the following, however, they can be also of other origins, such as e.g.

magnetic impurities, etc. The electrons and nuclei interact via the hyperfine interaction described by the Hamiltonian

$$H_{hyp} = \frac{1}{2} A \rho_0^{-1} |\psi_\perp(\boldsymbol{R}_\perp)|^2 \delta(r-R) \boldsymbol{\sigma} \cdot \boldsymbol{I}, \tag{6.1}$$

where A is a hyperfine constant of the material, ρ_0 is the nuclear spin density, $\psi_\perp$ is the transverse part of electron wavefunction, r denotes the electron position along the wire, $(R, \boldsymbol{R}_\perp)$ is the position of the nucleus along the wire and in the transverse direction respectively, $\boldsymbol{\sigma}$ is an electron spin operator, and $\boldsymbol{I}$ is a nuclear spin operator (in units of $\hbar$) with the magnitude I. We assume that the transverse part of the electron wavefunction $\psi_\perp(\boldsymbol{R}_\perp)$ is constant in the wire cross-section, $|\psi_\perp(\boldsymbol{R}_\perp)|^2 = 1/C$, where C is the wire crossection area. We parametrize it alternatively by the number of nuclear spins in the cross-section, $N_\perp = C a \rho_0$, with a being the lattice constant. In GaAs $\rho_0 = 8/a^3$, $a = 0.565$ nm, $A = 90$ μeV, $I = 3/2$, and $N_\perp$ is typically of the order of 10^3. Finally, we introduce $N = L/a$ with L the wire length (typically of order microns), which gives $N N_\perp$ as the total number of nuclear spins in the wire.

We note that in the case where the "wire" is not physically separated from the surrounding medium, the extent of the electronic wave function (confined, e.g., electrostatically) in the transverse direction sets the diameter of the wire in our model. In such a case we assume that the localized spins, if present outside the wire volume, are not ordered, meaning the surrounding medium is a paramagnet. Such an environment would provide an additional dissipation channel, but would not change the wire spin order, and thus our conclusions, in any qualitative way.

The total Hamiltonian reads

$$H_{tot} = -\frac{\hbar^2}{2m} \partial_r^2 + H_{hyp}, \tag{6.2}$$

where m is electron effective mass and $\hbar$ is the Planck constant. If the hyperfine interaction, Eq. (6.1), is weak on the energy scale of the electrons, its effects can be treated perturbatively. The condition is quantified by $A \ll \varepsilon_F$, where ε_F is the Fermi energy of the electron system. This condition is well satisfied in the cases we consider here. A Schrieffer-Wolff transformation on H_{tot} perturbatively in H_{hyp}, *i.e.*, in order A/ε_F, results to leading order in an effective interaction between the localized spins, the RKKY interaction [24, 162, 163, 164, 165, 204],

$$H_{RKKY} = \sum_{i,j} \boldsymbol{I}_i \cdot J_{ij} \boldsymbol{I}_j. \tag{6.3}$$

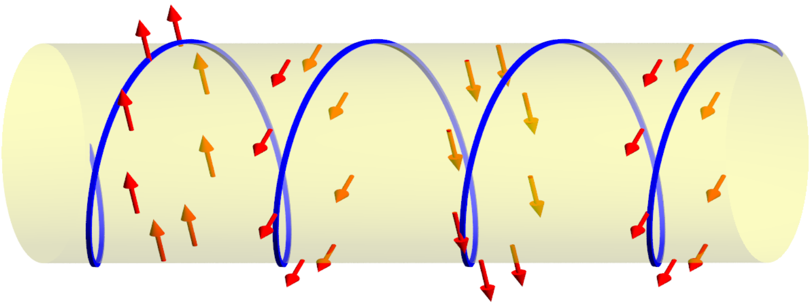

Figure 6.1: A sketch of a conducting wire (yellow cylinder) with itinerant electrons (not shown) that couple to localized nuclear spins (red arrows) via hyperfine interaction. As a result, a helical nuclear polarization emerges below a critical temperature. The blue spiral is a guide to the eye showing the direction of the helical polarization. The helical plane is chosen to be perpendicular to the wire axis (which need not be the case in general).

Here, the indexes i, j label the nuclear spins and the RKKY coupling $J_{ij} = J(|R_i - R_j|)$ is related to the static spin susceptibility of electrons (see Eq. (C1) and below in Ref. [182]), giving rise to the spatially dependent RKKY interaction.

Let us rewrite Eq. (6.3) in the momentum representation, defined through the Fourier transforms $J_q = \sum_{R_i} \exp[-iq(R_i - R_j)] J_{ij}$, with $R_i \in a, 2a, \ldots, Na$, and $\mathbf{I}_q = \sum_i \exp(iqR_i)\mathbf{I}_i$, with $i \in 1, \ldots, NN_\perp$, and in both cases $q \in (2\pi/N) \times \{0, 1, \ldots, N-1\}$. We get

$$H_{RKKY} = \frac{1}{N} \sum_q \mathbf{I}_q \cdot J_q \mathbf{I}_{-q}. \tag{6.4}$$

In one dimension, the RKKY coupling J_q has a sharp minimum at momentum $q = \pm 2k_F$, with $k_F = \sqrt{2m\varepsilon_F}/\hbar$ the electron Fermi wavevector [1, 28]. Consider an approximation in which we neglect all values of J_q with respect to the large (negative) value at this minimum,

$$H_{RKKY} \simeq \frac{1}{N} J_{2k_F} \left(\mathbf{I}_{2k_F} \cdot \mathbf{I}_{-2k_F} + \mathbf{I}_{-2k_F} \cdot \mathbf{I}_{2k_F} \right). \tag{6.5}$$

To understand the spectrum of this Hamiltonian, we introduce linearly transformed spin operators,

$$\boldsymbol{I}_i = \mathcal{R}_{\boldsymbol{u},2k_F R_i} \hat{\boldsymbol{I}}_i, \tag{6.6}$$

with $\mathcal{R}_{\mathbf{u},\phi}$ the matrix corresponding to a rotation by angle ϕ around a unit vector $\mathbf{u}$. Inserting Eq. (6.6) into Eq. (6.5) we get

$$H_{RKKY} \simeq \frac{1}{N} J_{2k_F} \left(\hat{\boldsymbol{I}}^{\perp}_{q=0} \cdot \hat{\boldsymbol{I}}^{\perp}_{q=0} + \mathcal{B}/2 \right), \tag{6.7}$$

where we define the vector components along $\boldsymbol{u}$ as $\hat{I}^u = \hat{\boldsymbol{I}} \cdot \boldsymbol{u}$, and perpendicular to it as $\hat{\boldsymbol{I}}^{\perp} = \hat{\boldsymbol{I}} - \hat{I}^u \boldsymbol{u}$, and we separated the terms bilinear in the spin operators at finite momenta,

$$\mathcal{B} = \sum_{q=\pm 2k_F} [2\hat{I}^u_q \hat{I}^u_{-q} + \hat{\boldsymbol{I}}^{\perp}_{2q} \cdot \hat{\boldsymbol{I}}^{\perp}_{-2q} + i\mathrm{sgn}(q)(\hat{\boldsymbol{I}}^{\perp}_{2q} \times \hat{\boldsymbol{I}}^{\perp}_{-2q}) \cdot \boldsymbol{u}]. \tag{6.8}$$

The first term in the bracket of Eq. (6.7) describes the energy of ferromagnetically coupled spins $\hat{\boldsymbol{I}}_i$: a configuration in which all these spins are collinear, along a vector perpendicular to $\boldsymbol{u}$, gives a minimal possible energy, of value $NN_{\perp}^2 J_{2k_F} I^2$. This configuration corresponds to a classical ground state of Eq. (6.4) as well, as it saturates the energy lower bound obtained using $\sum_q |\boldsymbol{I}_q|^2 = NN_{\perp} \sum_i |\boldsymbol{I}_i|^2$, the Parseval's identity.

Going back to the laboratory frame according to Eq. (6.6), the ground state corresponds to a helical configuration where the nuclear spins are oriented parallel to each other in the wire cross-section, along a direction which rotates in a fixed plane as one moves along the wire with the spatial period equal to a half of the electron Fermi wavelength π/k_F (for illustration, see Fig. 6.1). We shall refer to this plane as the helical plane, with $\boldsymbol{u}$ being its normal unit vector. A unit vector $\boldsymbol{h} \perp \boldsymbol{u}$ gives the direction of the polarization within this plane at position $R = 0$.

Equation (6.7) has full spin rotation-symmetry, as it is just Eq. (6.5) rewritten in a different reference frame. However, through the choice of the definite helicity and the vector $\boldsymbol{u}$, the first term in Eq. (6.7) breaks this symmetry. To restore it, the finite momenta components, Eq. (6.8), necessarily appear. To understand these terms in more detail, we note that choosing a frame with helicity opposite to the ground state helicity would lead to a swap of the roles of $\hat{\boldsymbol{I}}^{\perp}_0$ and $\hat{\boldsymbol{I}}^{\perp}_{\pm 4k_F}$. Second, configurations where both helicities are populated lead to a lower energy gain. For example, choosing both with the same weight, gives in the laboratory frame a spin-density wave, i.e., a cos-like oscillation along a fixed vector, $\boldsymbol{I}_i = \boldsymbol{h} \cos{(2k_F R_i)}$, which gives only half of the energy gain of a helical order. Such oscillating, rather than rotating, configuration corresponds to the first term in Eq. (6.8). We therefore conclude that up to the spin rotational symmetry, which allows for arbitrary directions of $\boldsymbol{u}$, and $\hat{\boldsymbol{I}}^{\perp}$, the ground state with ferromagnetically aligned $\hat{\boldsymbol{I}}_i$ (helically ordered $\boldsymbol{I}_i$) is unique.

If the order is established, the expectation value of $\hat{\boldsymbol{I}}^{\perp}_{q=0}$ is macroscopic, and we parametrize it by a polarization p_h,

$$\langle \hat{\boldsymbol{I}}^{\perp}_{q=0} \rangle = N N_{\perp} I p_h \boldsymbol{h}, \tag{6.9}$$

so that $p_h = 1$ corresponds to a completely ordered state. With this we reduce Eq. (6.5) by the mean field approximation to a Hamiltonian describing a set of non-interacting spins

$$H_{RKKY} \simeq \sum_i \mu_N \boldsymbol{B}_i^N \cdot \boldsymbol{I}_i, \tag{6.10}$$

in the presence of the position-dependent internal field

$$\mu_N \boldsymbol{B}_i^N = 2 p_h N_{\perp} I J_{2k_F} \mathcal{R}_{\boldsymbol{u}, 2k_F R_i} \boldsymbol{h}. \tag{6.11}$$

This concludes a simplified derivation of the reduction of the RKKY Hamiltonian, Eq. (6.3), into a set of non-interacting spins, Eq. (6.10), in an effective (mean) field, Eq. (6.11). A detailed analysis of the applicability of such an approximation was given in Ref. [182], based on the derivation of the spectrum of the full Hamiltonian Eq. (6.3), without employing a mean field ansatz. There it was found that this approximation, in essence neglecting the long wavelength magnons, is well justified for sub-Kelvin temperatures and wire lengths relevant for mesoscopic experiments.

As we consider the limit $A \ll \varepsilon_F$, we adopt the Bohr-Oppenheimer approximation, assuming that electrons react instantaneously to the changes in nuclear spin subsystem. Consequently, we can consider the effect of the nuclear polarization on electrons as an Overhauser field [28]

$$\mu_e \boldsymbol{B}_{Ov} = \frac{Aa}{2N_{\perp}} \sum_j \delta(r - R_j) \langle \boldsymbol{I}_j \rangle, \tag{6.12}$$

where μ_e is an electron magnetic moment. Thus, the electron Hamiltonian is

$$H_{el} = -\frac{\hbar^2}{2m} \partial_r^2 + \mu_e \boldsymbol{B}_{Ov} \cdot \boldsymbol{\sigma}. \tag{6.13}$$

In Eq. (6.13) we do not include electron-electron interactions explicitly. In the following to evaluate the internal field $\boldsymbol{B}_i^N$ we use Eqs. (C4), and (C5) from Ref. [182]. In these equations electron-electron interaction is significant (for example, for the critical temperature of the helical polarization [1, 28, 180, 182]) and therefore is included.

To describe the nuclear polarization in the wire when a bias voltage is applied, we will first investigate the behaviour of one nuclear spin placed in an effective field of all others, Eq. (6.10), and interacting with the bath of electrons described by Eq. (6.13).

6.3 Helical electrons and finite voltage

To find how a nuclear spin is affected by the electrons when the bias voltage is applied, we first consider the properties of the electron bath in the wire. As already mentioned in Sec. 6.2, the electrons are moving in the Overhauser field produced by the nuclear spins [see Eqs. (6.12), (6.13)]. As the nuclear spins form a helix in equilibrium, this particular Overhauser field, denoted by $\boldsymbol{B}_h$, is also helical. Consequently, the electron spectrum is

$$\varepsilon_{\pm} = \frac{\hbar^2(k^2+k_F^2)}{2m} \pm \frac{1}{m}\sqrt{m^2\mu_e^2B_h^2+\hbar^4k^2k_F^2}, \tag{6.14}$$

where k is the electron wavevector, and ε_- and ε_+ denote the lower and upper subbands respectively. They are split by the gap $2\mu_e B_h$ at $k=0$. The corresponding wavefunctions are

$$\Psi_{k,-}(r) = \frac{e^{ikr}}{\sqrt{L}}[e^{-ik_Fr}\cos\frac{\theta_k}{2}|\uparrow\rangle + e^{ik_Fr}\sin\frac{\theta_k}{2}|\downarrow\rangle], \tag{6.15}$$

$$\Psi_{k,+}(r) = \frac{e^{ikr}}{\sqrt{L}}[e^{ik_Fr}\cos\frac{\theta_k}{2}|\downarrow\rangle - e^{-ik_Fr}\sin\frac{\theta_k}{2}|\uparrow\rangle], \tag{6.16}$$

where $\cos\theta_k = \frac{\hbar^2kk_F}{\sqrt{(\hbar^2kk_F)^2+(m\mu_eB_h)^2}}$ and $\sin\theta_k = \frac{-m\mu_eB_h}{\sqrt{(\hbar^2kk_F)^2+(m\mu_eB_h)^2}}$, and $|\uparrow\rangle$, $|\downarrow\rangle$ denote the spin states with spin up and spin down respectively, where $\boldsymbol{u}$ sets the quantization axis. These expressions of the wavefunctions can be simplified since typically the ratio $\Lambda \equiv \mu_eB_{max}/\varepsilon_F \ll 1$, where B_{max} is the maximum Overhauser field when all nuclei are fully polarized along a given direction. For example, for a GaAs quantum wire $\mu_eB_{max} \simeq 68$ μeV, while $\varepsilon_F \simeq 10\,\text{meV}$, which gives $\Lambda \simeq 0.0068$. Consequently, we can use Λ as a small parameter.

We expand Eq. (6.15) in leading order of Λ and for the states within the partial gap we get

$$\Psi_{k,-}(r) \approx \frac{1}{\sqrt{L}} \begin{cases} -e^{i(k-k_F)r}|\xi_R\rangle, & k > 0, \\ \;\; e^{i(k+k_F)r}|\xi_L\rangle, & k < 0, \end{cases} \tag{6.17}$$

where for right-moving electrons ($k > 0$) the spinor is $|\xi_R\rangle = |\uparrow\rangle$, and for left-moving ($k < 0$) it is $|\xi_L\rangle = |\downarrow\rangle$. Therefore, within our approximation the electronic states in the partial gap are helical: the spin is determined by the propagation direction, and is opposite for left-moving and right-moving electrons.

Next, we consider the voltage applied to the wire and define it as the difference between the chemical potentials for the left- and right-moving electrons (see Fig. 6.2). Assuming a ballistic wire, the chemical potential of a given branch is constant in space. With the polarity as assumed in Fig. 6.2, the applied voltage depletes the left (L) branch and increases the population of the right (R) branch. This imbalance in population opens up an additional phase space for the electrons to backscatter - predominantly from R to L. Because of the helical character of the states, such backscattering is accompanied by an electron spin flip (from $|\uparrow\rangle$ to $|\downarrow\rangle$). This, in turn, is enabled by the total spin-conserving hyperfine interaction Eq. (6.1), so that each electron spin flip is compensated by a nuclear spin flip in the opposite direction. In this way a *uniform* nuclear polarization along the $\boldsymbol{u}$ direction is built up. We denote $\boldsymbol{B}_u$ as the Overhauser field corresponding to this uniform polarization.

From Fig. 6.2 one can see that this scattering induced spin polarization works only for the electronic states within the partial gap. Aiming at the helical order detection, applying voltage larger than the partial gap is therefore disadvantageous: it will not increase the spin pumping rate, but it will decrease all polarizations through heating, similarly as high temperature. We can therefore restrict our theory to small voltage, i.e. $eV < 2\mu_e B_h$, where $-e$ is the electron charge, and small temperatures T, *i.e.*, $k_B T < 2\mu_e B_h$. We can then adopt two approximations. First, we neglect the influence from electron states which are not in the partial gap (the upper (+) subband is neglected completely), because their contribution to transport is exponentially small, proportional to $\exp[(-\mu_e B_h + eV/2)/k_B T]$. Second, we use Eq. (6.17) for the electron wavefunctions, which means that we consider Eq. (6.15) in leading order of $k_B T/\varepsilon_F$, eV/ε_F, and Λ. Therefore, for a description of the electron system in terms of a heat bath that causes the relaxation of the nuclear spins, we take into account two branches: left- and right-moving electrons with spins $|\downarrow\rangle$ and $|\uparrow\rangle$, respectively.

The spectrum of electrons moving in the total Ovehauser field $\boldsymbol{B}_h+\boldsymbol{B}_u$ reads

$$\varepsilon_{u,\pm}=\frac{\hbar^2(k^2+k_F^2)}{2m}\pm\sqrt{\mu_e^2B_h^2+\left[\frac{\hbar^2kk_F}{m}-\mu_eB_u\right]^2}, \tag{6.18}$$

see Fig. 6.2. The asymmetry of the spectrum is due to the uniform Overhauser field $\boldsymbol{B}_u$. The corrections to the wave functions, Eq. (6.17), due to $\boldsymbol{B}_u$ are negligible in leading order of Λ. Namely, the presence of the uniform component in the Overhauser field rotates (cants) the spinors $|\xi_{L(R)}\rangle$ away from down (up) direction by a very small angle (for a maximal possible field $B_u=B_{max}$ this angle is for our parameters smaller than 0.1°). Even though the canted up- and down spinors are no longer orthogonal to each other, it does not play any substantial role. Indeed, since the spin flips of electrons are compensated by nuclei, there is no spin conservation (no selection rules) within the two subsystems taken individually.

We note that from Eqs. (6.15) and (6.16) it follows that the electron spins become also polarized, thereby producing a Knight shift acting as an effective magnetic field $\boldsymbol{B}_j^e$ back on the nuclear spins. This Knight shift is defined as $\langle H_{hyp}\rangle_{el}=\mu_N\boldsymbol{B}_j^e\cdot\boldsymbol{I}_j$, where $\langle ...\rangle_{el}$ denotes averaging over the eigenstates of the Hamiltonian in Eq. (6.13) with populations defined by the voltage. In this work, however, we can neglect $\boldsymbol{B}_j^e$ with respect to $\boldsymbol{B}_j^N$ produced by the RKKY interaction [28, 182].

6.4 Bloch Equation for the total nuclear spin in the wire

To investigate the time-dynamics of the nuclear spins, we apply the standard Bloch-Redfield theory to our problem, which is valid for weak coupling between spin system and bath degrees of freedom [86, 205], as is the case here. First, we write down the Bloch equation for the average $\langle\boldsymbol{I}_j\rangle$ of the jth nuclear spin. By applying Eqs. (7)-(11) from Ref. [86] to our Eqs. (6.1), (6.10), and (6.13), we get (for more details see Appendix 6.A)

$$\partial_t\langle\boldsymbol{I}_j\rangle=\boldsymbol{\omega}_j\times\langle\boldsymbol{I}_j\rangle-\boldsymbol{\Gamma}_j\langle\boldsymbol{I}_j\rangle+\boldsymbol{\Upsilon}_j, \tag{6.19}$$

where $\boldsymbol{\omega}_j=\mu_N\boldsymbol{B}_j^N/\hbar$ determines the precession, the relaxation tensor $\boldsymbol{\Gamma}_j$ the decay and the inhomogeneous vector term $\boldsymbol{\Upsilon}_j$ the stationary value of

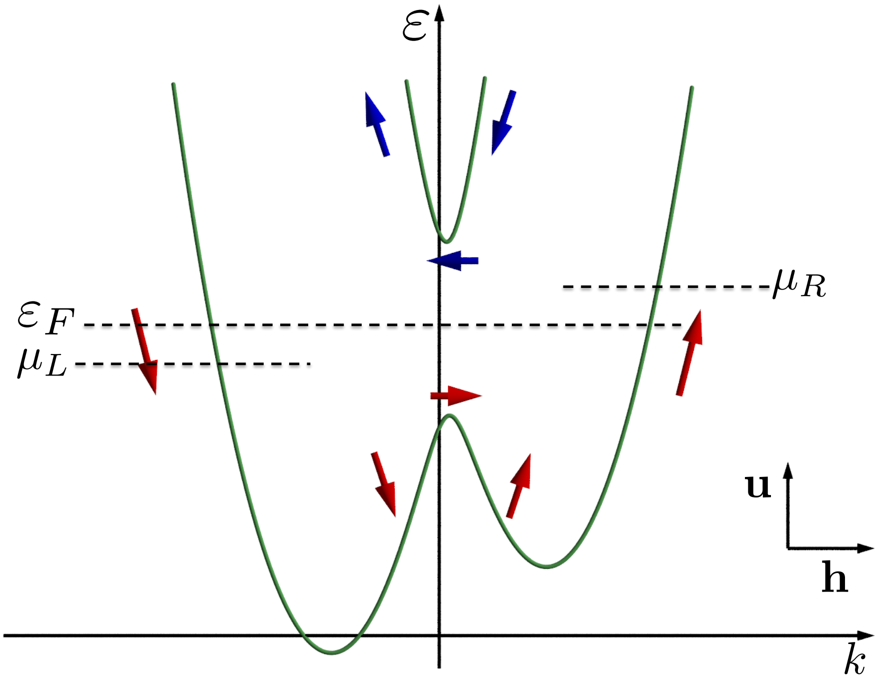

Figure 6.2: Sketch of the energy spectrum given in Eq. (6.18) and the direction of the electron spins in the presence of the helical Overhauser field $\boldsymbol{B_h}$ and the uniform Overhauser field $\boldsymbol{B_u}$ perpendicular to the plane of the helix. Red arrows denote the spin directions of the electrons in the lower subband, and the blue arrows label the spin directions for the upper subband. The coordinate system for the spins is formed by $\boldsymbol{h}$ and $\boldsymbol{u}$ shown in the right lower corner. The chemical potentials for left- and right-movers are denoted as μ_L and μ_R, respectively. The voltage applied to the wire is $eV_{RL} = \mu_R - \mu_L$.

$\langle \boldsymbol{I}_j \rangle$. Both, $\boldsymbol{\Gamma}_j$ and $\boldsymbol{\Upsilon}_j$ are expressed in terms of time correlators (see App. A)

$$\mathcal{J}_{nl}(\omega) = \frac{1}{2\hbar^2} \int_0^\infty e^{-i\omega t} \langle \delta B_n(0) \delta B_l(t) \rangle_{el} dt, \tag{6.20}$$

where t is time, the indexes $n,\ l$ label the components of the effective fluctuating internal field $\delta\boldsymbol{B}$ defined via $H_{hyp} - \langle H_{hyp} \rangle_{el} = \delta\boldsymbol{B} \cdot \boldsymbol{I}_j$. The time-dependence follows from the interaction representation $\delta\boldsymbol{B}(t) = e^{iH_{el}t/\hbar} \delta\boldsymbol{B} e^{-iH_{el}t/\hbar}$. We note that above equations are valid for a spin 1/2. However, it is well-known [110] that the relaxation time of a spin into its stationary value does not depend on the spin length (in Born approximation). Thus, we will assume that our results apply for arbitrary spins.

As follows from Secs. 6.2 and 6.3, we can define the expectation value of a nuclear spin at position $R = 0$ as

$$\langle \boldsymbol{I}_0 \rangle / I = p_h \boldsymbol{h} + p_u \boldsymbol{u}, \tag{6.21}$$

where $0 \leq p_{h,u} \leq 1$ denote the polarizations along the two orthogonal directions $\boldsymbol{h}$ and $\boldsymbol{u}$, respectively.

We also introduce position-independent tensors $\boldsymbol{\Gamma}_0$ and $\boldsymbol{\Upsilon}_0$ in the rotated frame defined by the rotation matrix $\mathcal{R}^{\dagger}_{\boldsymbol{u},2k_F R_j}$, via

$$\begin{aligned} \boldsymbol{\Gamma}_j &= \mathcal{R}_{\boldsymbol{u},2k_F R_j} \boldsymbol{\Gamma}_0 \mathcal{R}^{\dagger}_{\boldsymbol{u},2k_F R_j}, & (6.22) \\ \boldsymbol{\Upsilon}_j &= \mathcal{R}_{\boldsymbol{u},2k_F R_j} \boldsymbol{\Upsilon}_0. & (6.23) \end{aligned}$$

Having Eqs. (6.11), (6.19), (6.22), and (6.23), we can describe the time-evolution of the nuclear spin $\boldsymbol{I}_j$ in the rotated frame.

Eventually we are interested in the dynamics of the total (macroscopic) polarizations, rather than the one of an individual nuclear spin. We therefore introduce the total nuclear spin in the rotated frame $\sum_j \mathcal{R}^{\dagger}_{\boldsymbol{u},2k_F R_j} \langle \boldsymbol{I}_j \rangle \equiv N N_\perp \langle \boldsymbol{I}_0 \rangle$, and write the equation of motion for it using Eqs. (6.11), (6.19), (6.22), and (6.23). We get

$$\partial_t \langle \boldsymbol{I}_0 \rangle = -\Omega (\langle \boldsymbol{I}_0 \rangle \cdot \boldsymbol{h}) \boldsymbol{h} \times \boldsymbol{u} - \boldsymbol{\Gamma}_0 \langle \boldsymbol{I}_0 \rangle + \boldsymbol{\Upsilon}_0, \tag{6.24}$$

where we denoted $\Omega = I p_u |J_{2k_F}|/\hbar$. The first term implies a rotation of the helical direction $\boldsymbol{h}$, around the axis $\boldsymbol{u}$ with frequency Ω. This can be seen by introducing a time-dependent vector $\boldsymbol{h}(t) = \mathcal{R}_{\boldsymbol{u},\alpha(t)} \boldsymbol{h}$, where $\alpha(t) = \int_0^t \Omega d\tau$. In the Born-Oppenheimer approximation, the tensors $\boldsymbol{\Gamma}_j$ and $\boldsymbol{\Upsilon}_j$ are functions of the instantaneous values of $\boldsymbol{h}$ and $\boldsymbol{u}$, so we write

$$\begin{aligned} \tilde{\boldsymbol{\Gamma}}_j &= \mathcal{R}_{\boldsymbol{u},\alpha(t)} \boldsymbol{\Gamma}_j \mathcal{R}^{\dagger}_{\boldsymbol{u},\alpha(t)}, & (6.25) \\ \tilde{\boldsymbol{\Upsilon}}_j &= \mathcal{R}_{\boldsymbol{u},\alpha(t)} \boldsymbol{\Upsilon}_j. & (6.26) \end{aligned}$$

With this the time evolution of $\langle \boldsymbol{I}_0 \rangle$ in the rotating frame, $\langle \tilde{\boldsymbol{I}}_0 \rangle = \mathcal{R}_{\boldsymbol{u},\alpha(t)} \langle \boldsymbol{I}_0 \rangle$, is described by

$$\partial_t \langle \tilde{\boldsymbol{I}}_0 \rangle = -\tilde{\boldsymbol{\Gamma}}_0 \langle \tilde{\boldsymbol{I}}_0 \rangle + \tilde{\boldsymbol{\Upsilon}}_0. \tag{6.27}$$

To evaluate the tensors in this equation, we use the results of Sec. 6.3 and approximate the electronic states within the gap by Eq. (6.17) and the spectrum by Eq. (6.18) with $B_h = 0 = B_u$. We can then use Eq. (6.27) to describe the polarization of the nuclear spins in the wire as function of temperature and voltage.

6.5 Resulting Polarizations

To find the polarizations p_h and p_u from Eq. (6.27) we now evaluate the tensors $\mathbf{\Gamma}_0$ and $\mathbf{\Upsilon}_0$ explicitly. For that we first evaluate the correlator $\mathcal{J}_{nl}(\omega)$. Using Eqs. (6.17) and (6.18) we get

$$\mathcal{J}_{nl}(\omega) = \frac{A^2 a^2}{32\hbar^3 \pi v_F^2 N_\perp^2} \sum_{a,b\in\{L,R\}} M_{nl}^{ab} Q_{ab}, \tag{6.28}$$

$$M_{nl}^{ab} = \langle \xi_a | \sigma_n | \xi_b \rangle \langle \xi_b | \sigma_l | \xi_a \rangle, \tag{6.29}$$

$$Q_{ab} = \int d\varepsilon f\left(\varepsilon + eV_{ba}/2\right)\left[1 - f\left(\varepsilon + \hbar\omega - eV_{ba}/2\right)\right], \tag{6.30}$$

where $eV_{ba} = \mu_b - \mu_a$ is the difference between chemical potentials of branch b and a, with a and b denoting L (left-movers) or R (right-movers). Here we also use the Fermi distribution function $f(\varepsilon) = [\exp[\varepsilon/(k_B T)] + 1]^{-1}$. As was mentioned in Sec. 6.3, we consider voltages and temperatures smaller than the partial gap $2\mu_e B_h$ given by the helical polarization. Therefore the term $f(\varepsilon + eV_{ba}/2)[1 - f(\varepsilon + \hbar\omega - eV_{ba}/2)]$ allows us to consider only the energy window of $\pm\mu_e B_h$ around ε_F, because $f(\varepsilon)$ decays exponentially for $\varepsilon/k_B T \gg 1$. Consequently, we approximate the electron density of states (per spin) by $\nu(\varepsilon) \approx \nu(\varepsilon_F)$, Up to first order in Λ, we have $\nu(\varepsilon_F) = 1/(\pi\hbar v_F)$, where $v_F = \varepsilon_F/(\hbar k_F)$ is the Fermi velocity of the electrons.

Having obtained $\mathcal{J}_{nl}(\omega)$, it is straightforward to calculate $\mathbf{\Gamma}_0$ and $\mathbf{\Upsilon}_0$, using Eqs. (6.37)-(6.39) and (6.28)-(6.30). We can then solve Eq. (6.27) for the steady state polarizations (keeping ω_0 as a constant) and obtain

$$p_h = \frac{4\hbar\omega_0}{(\hbar\omega_0 - eV)\coth\left(\frac{\hbar\omega_0 - eV}{2k_BT}\right) + (\hbar\omega_0 + eV)\coth\left(\frac{\hbar\omega_0 + eV}{2k_BT}\right) + 2\hbar\omega_0\coth\left(\frac{\hbar\omega_0}{2k_BT}\right)}, \tag{6.31}$$

$$p_u = \frac{4\hbar\omega_0 \frac{(\hbar\omega_0 - eV)\coth\left(\frac{\hbar\omega_0 - eV}{2k_BT}\right) - (\hbar\omega_0 + eV)\coth\left(\frac{\hbar\omega_0 + eV}{2k_BT}\right)}{(\hbar\omega_0 - eV)\coth\left(\frac{\hbar\omega_0 - eV}{2k_BT}\right) + (\hbar\omega_0 + eV)\coth\left(\frac{\hbar\omega_0 + eV}{2k_BT}\right) + 2\hbar\omega_0\coth\left(\frac{\hbar\omega_0}{2k_BT}\right)} + 4eV}{(\hbar\omega_0 - eV)\coth\left(\frac{\hbar\omega_0 - eV}{2k_BT}\right) + (\hbar\omega_0 + eV)\coth\left(\frac{\hbar\omega_0 + eV}{2k_BT}\right) + 2eV\coth\left(\frac{eV}{2k_BT}\right)}. \tag{6.32}$$

However, from Eq. (6.11) it follows that $\hbar\boldsymbol{\omega}_0 = 2p_h N_\perp I J_{2k_F}\boldsymbol{h}$, *i.e.*, ω_0 depends on p_h. This leads to non-linear algebraic equations for two unknowns, p_u and p_h, which we solve numerically using material parameters for GaAs (analytical expressions for small deviations of the polarizations are given below). We plot the values obtained in this way and discuss their behaviour as a function of voltage and temperature, the experimental parameters that are most directly accessible.

The voltage dependence of the polarizations is shown in Fig. 6.3. We can see that the polarization p_u grows faster with voltage than p_h decays, therefore the overall polarization of the nuclei $\sqrt{p_u^2 + p_h^2}$ grows with voltage, too. This means that the nuclear spins are more polarized when a voltage is applied than when they are in equilibrium at the same temperature. We also note that having a non-zero component p_u means that nuclear spins have a conical polarization, rather than a helical one. To plot Fig. 6.3 we used Eqs. (C4), and (C5) from Ref. [182] as was mentioned above, where the dependence of $\hbar\omega_0$ on temperature is described in detail. To evaluate $\hbar\omega_0$ we used the characteristic values for GaAs: the Fermi velocity $v_F = 2.3 \times 10^5$ m/s, and the number of nuclei in the wire cross-section $N_\perp = 1300$. For the expression for J_{2k_F} taken from Ref. [182] we use the electron-electron interaction Luttinger liquid parameter $K_\rho = 0.2$ and the absolute value of spin $I = 3/2$. For the constants described above and at $T = 90$ mK and $p_u = 0.1$ the rotation frequency of the nuclear spin helix is $\Omega \approx 1.5 \times 10^6\ \text{s}^{-1}$.

It is natural to expect that high temperature destroys the nuclear helical order [1, 28, 180, 182]. Indeed, Fig. 6.4 shows that the helical polarization p_h decays with temperature and then drops in magnitude around $T \simeq 109$ mK. As our calculation is valid for $eV, k_BT < 2\mu_e B_h$, the smallest value of p_h allowed by self-consistency for our parameters is $p_h \simeq 0.2$. From Fig. 6.4 it also follows that the polarization p_u grows with temperature. This growth is explained by the fact that due to higher temperature the electron states with higher energy become occupied. This makes the nuclear spin flip more probable. It is obvious that there is a temperature where the polarization p_u gets destroyed, however, for the range of temperatures given in Fig. 6.4 p_u does grow, whereas the helical polarization p_h decays significantly. The decay of p_h with temperature is rapid, while the growth of p_u is less pronounced. Therefore, the overall nuclear polarization in the wire strongly decays with increasing temperature. For the parameters we used for Fig. 6.4 the effect of temperature on p_h is stronger than the one of a finite voltage. The initial temperature scaling of p_h away from unity (see Fig. 6.4) can be obtained readily from Eq. (6.31) by treating $1 - p_h$ as a small perturbation. This yields

$$p_h \approx 1 - \frac{2}{1 + e^{\frac{\kappa}{T^g}}} \cdot \frac{1}{1 - \frac{\kappa}{2T^g}\,\text{sech}^2\big(\frac{\kappa}{2T^g}\big)} \tag{6.33}$$

$$\approx 1 - 2e^{-\frac{\kappa}{T^g}}, \tag{6.34}$$

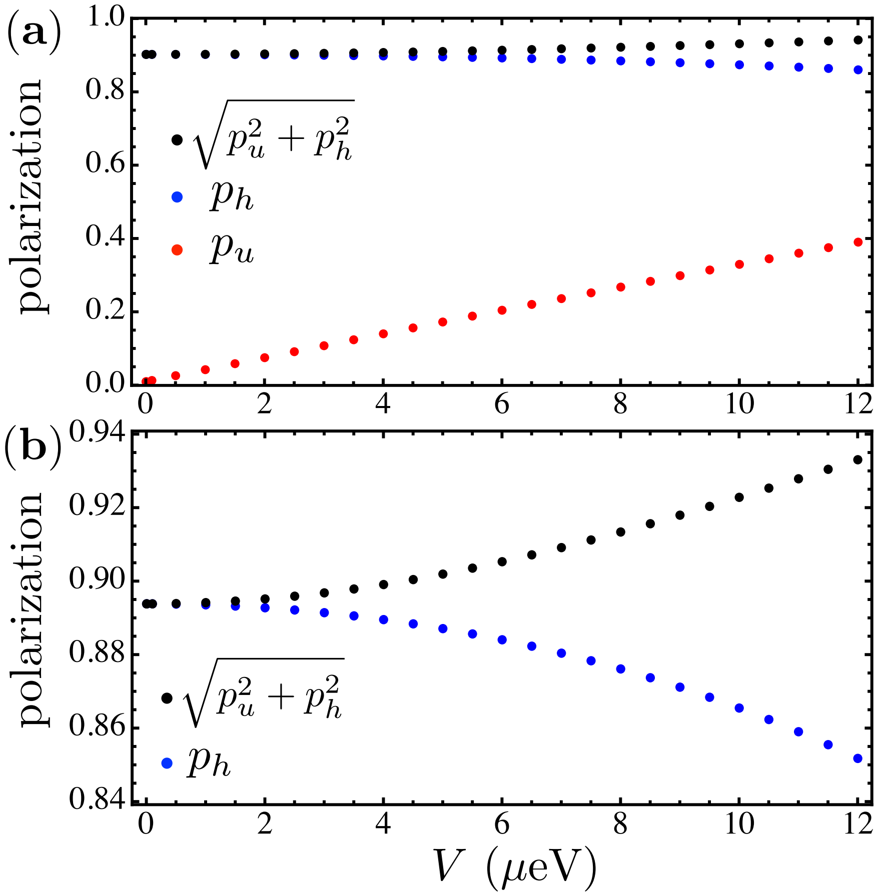

Figure 6.3: (a) The voltage dependence of the polarization p_h along helical direction $\boldsymbol{h}$ (blue), polarization p_u in the direction of $\boldsymbol{u}$ perpendicular to the helix plane (red), and the overall polarization of nuclei $\sqrt{p_u^2 + p_h^2}$ (black). (b) Enlarged from (a) the voltage dependence of p_h and $\sqrt{p_u^2 + p_h^2}$. We use $T = 90$ mK and other parameters as given in the text. We recall that our parametrization is such that $p_u = 1$ corresponds to $B_u = B_{max}$, which is about 5 T in GaAs, and analogously for B_h.

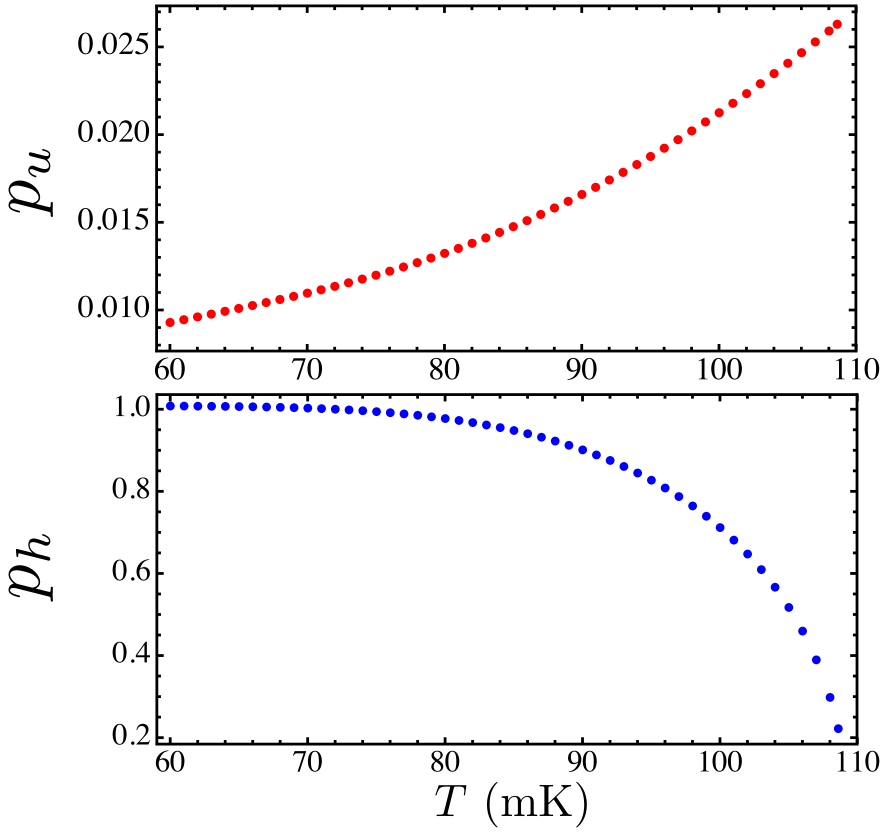

Figure 6.4: Plot of the temperature dependence of the polarization p_u (upper panel, red) and the polarization p_h (lower panel, blue). For these plots the same parameters were used as in Fig. 6.3 and the applied voltage is $eV = 0.5\ \mu$eV. We note that our calculation is valid for $eV, k_B T < 2\mu_e B_h$, therefore the smallest value of p_h we consider here is $p_h \simeq 0.2$.

where the first equality holds well for the temperature interval $60\text{mK} < T < 90\text{mK}$, while the second one is a good approximation for $60\text{mK} < T < 80\text{mK}$. Here we denoted $g = 3 - \frac{4K_\rho}{\sqrt{2(1+K_\rho^2)}}$, and the temperature-independent parameter $\kappa = 2N_\perp I|J_{2k_F}|T^{g-1}/k_B$ depends on the material and geometrical properties of the sample (see Eq. (11) and Eqs. (C4) and (C5) of Ref. [182]). For $K_\rho = 0.2$ (chosen for the plots) we get $g = 2.4$ (we recall that $K_\rho = g = 1$ corresponds to vanishing electron-electron interactions).

The initial decrease of p_h due to voltage in Fig. 6.3 for $V < 3\ \mu$eV scales as

$$p_h \approx \alpha - \gamma V^2, \tag{6.35}$$

where α and γ depend on material and geometrical parameters of the nanowire and on temperature.

Finally, we mention that recent progress in nuclear spin magnetometry on nanowires [202, 203] has opened the perspective to measure the nuclear spin polarizations directly and thus to test the predictions made here. Moreover, due to the helical nuclear polarization which acts on electrons as an Overhauser field $\boldsymbol{B}_h$ there is a partial gap in the electron spectrum [see Eq. (6.18)]. As a result, the conductance of a ballistic nanowire is less than $2e^2/h$ for sufficiently low temperatures and $V < 2\mu_e B_h$ [1, 28, 29, 182]. As was shown above, the polarization p_h, and consequently $\boldsymbol{B}_h$, decrease with increasing voltage and temperature. We thus expect qualitatively that the conductance of the wire will increase with the decrease of the partial gap $2\mu_e B_h \propto p_h$.However, we caution that the behaviour of the polarizations $p_{h,u}$ can only indicate the trend for the conductance but does not give its precise dependence on temperature and voltage. Indeed, in transport new temperature and voltage effects emerge, especially in the transition region where the partial gap is comparable to temperature and voltage.

6.6 Conclusions

We have shown that due to the hyperfine interaction between electrons and nuclei in the wire the applied voltage changes the form of the nuclear polarization and its amplitude. Assuming that in equilibrium there is a helical nuclear polarization p_h present in the wire due to RKKY interaction, a bias voltage induces a uniform polarization p_u perpendicular to the helix plane. Due to this polarization the nuclear spin helix starts to rotate around the axis perpendicular to the helical plane. When a non-zero polarization p_u buidls up, the nuclear polarization changes from helical to conical.

We have also presented the voltage dependence of p_u and p_h and seen that p_u increases with voltage, whereas p_h decreases. Following from these two effects the overall nuclear polarization in the wire grows with voltage. Remarkably, p_u grows with temperature in the considered range of temperatures. This is because the nuclear spin flip becomes more probable as electrons occupy higher energy states. This thermal activation effect is noticeable for the considered regime $\hbar\omega_0 > eV$. The growth of the overall polarization $\sqrt{p_u^2 + p_h^2}$ with voltage and the growth of p_u with temperature are intriguing and *a priori* non-obvious effects. The polarization effects predicted here might be observed in transport experiments [29] or more directly via cantilever based nanoscale magnetometry [202, 203].

Finally we note that the current induced dynamical effects we found are not restricted to nuclear helimagnets. Among other systems, they are expected to appear in a wire with magnetic impurities, such as Mn-doped GaAs, once the helical order in the impurities is RKKY-induced. Even for moderate dopings, in such a system the coupling constant A/ρ_0, which is central to the energy scales in question, is more than thousand times larger than for nuclear spins. Even though the critical temperature can not be directly estimated from this ratio, as it is strongly influenced also by the electron-electron interactions, it is still expected to be larger by several orders of magnitudes compared to the sub-Kelvin range typical for nuclear spins. Though this was not our focus here, we note that, correspondingly, the partial gap and the resulting upper bound on the applied voltage will move to mV scale, more realistic for possible spintronics device applications.

6.7 Acknowledgments

We thank V. N. Golovach, D. Becker, B. Braunecker, L. Glazman, C. Kloeffel, T. Meng, and C. Orth for helpful discussions and acknowledge support from the Swiss NF, NCCR QSIT, and S^{3}NANO.

6.A Bloch equation for one nuclear spin

To write down the Bloch equation for the total nuclear spin in the wire, we use Eqs. (7)-(11) from Ref. [86]. Here we present them adopted to our case of a nuclear spin interacting with the bath of electrons and placed into the effective field produced by all other nuclear spins in the wire.

The Bloch equation for the nth nuclear spin reads

$$\partial_t \langle \boldsymbol{I}_n \rangle = \boldsymbol{\omega}_n \times \langle \boldsymbol{I}_n \rangle - \boldsymbol{\Gamma}_n \langle \boldsymbol{I}_n \rangle + \boldsymbol{\Upsilon}_n. \tag{6.36}$$

To express tensors $\boldsymbol{\Gamma}_n$ and $\boldsymbol{\Upsilon}_n$ we introduce a unit vector $\boldsymbol{l}$ along $\boldsymbol{\omega}_n$, i.e. $\boldsymbol{\omega}_n = \omega_n \boldsymbol{l}$. The tensor $\boldsymbol{\Gamma}_n$ consists of a dephasing part $\boldsymbol{\Gamma}_n^d$ which comes from energy conserving processes and a pure relaxation part $\boldsymbol{\Gamma}_n^r$, which comes from the energy exchange with the bath [86, 96] (played here by the electron system),

$$\begin{aligned} \boldsymbol{\Gamma}^d_{n,ij} &= [\delta_{ij} l_p l_q \mathcal{J}^+_{pq}(0) - l_i l_p \mathcal{J}^+_{pj}(0)], && (6.37)\\ \boldsymbol{\Gamma}^r_{n,ij} &= [\delta_{ij}(\delta_{pq} - l_p l_q)\mathcal{J}^+_{pq}(\omega_n) - && (6.38)\\ - &\quad (\delta_{ip} - l_i l_p)\mathcal{J}^+_{pj}(\omega_n) - \delta_{ij}\epsilon_{kpq} l_k \mathcal{I}^-_{pq}(\omega_n) + \\ + &\quad \epsilon_{ipq} l_p \mathcal{I}^-_{qj}(\omega_n)]. \end{aligned}$$

Here, the indexes i, j denote components of tensors, and we use the Einstein convention of summation over repeated indexes. Further, ϵ_{pqk} is the Levi-Civita symbol and δ_{ij} the Kronecker delta, while l_k denotes the kth component of vector $\boldsymbol{l}$. The inhomogeneous part of the Bloch equation $\boldsymbol{\Upsilon}_n$ reads [86, 96]

$$\begin{aligned} \boldsymbol{\Upsilon}_{n,i} = \frac{1}{2}(l_j \mathcal{J}^-_{ij}(\omega_n) - l_i \mathcal{J}^-_{jj}(\omega_n) + \epsilon_{ipq}\mathcal{I}^+_{pq}(\omega_n) + \\ + \epsilon_{iqk} l_k l_p [\mathcal{I}^+_{pq}(\omega_n) - \mathcal{I}^+_{pq}(0)]), \end{aligned} \tag{6.39}$$

where i denotes the component of $\boldsymbol{\Upsilon}_n$. The terms $\mathcal{J}^\pm_{ij}(\omega)$, $\mathcal{I}^\pm_{ij}(\omega)$ are defined as

$$\begin{aligned} \mathcal{J}^\pm_{ij}(\omega) &= \mathrm{Re}[\mathcal{J}_{ij}(\omega) \pm \mathcal{J}_{ij}(-\omega)], && (6.40)\\ \mathcal{I}^\pm_{ij}(\omega) &= \mathrm{Im}[\mathcal{J}_{ij}(\omega) \pm \mathcal{J}_{ij}(-\omega)]. && (6.41) \end{aligned}$$

The term $\mathcal{J}_{ij}(\omega)$ is the Laplace transformation of the correlator of the fluctuating fields $\delta\boldsymbol{B}$ at different times,

$$\mathcal{J}_{ij}(\omega) = \frac{1}{2\hbar^2}\int_0^\infty e^{-i\omega t}\langle \delta B_i(0)\delta B_j(t)\rangle_{el} dt, \tag{6.42}$$

where $\delta\boldsymbol{B}(t) = e^{iH_{el}t/\hbar}\delta\boldsymbol{B}e^{-iH_{el}t/\hbar}$. Using Eq. (6.36) we expressed the Bloch equation for the total nuclear spin in the wire resulting in Eq. (6.24).

CHAPTER 7

Nuclear spin relaxation in Rashba nanowires

Adapted from:
Alexander A. Zyuzin, Tobias Meng, Viktoriia Kornich, and Daniel Loss
"Nuclear spin relaxation in Rashba nanowires",
Phys. Rev. B **90**, 195125 (2014),
ArXiv:1407.2582 (2015).

We study the nuclear spin relaxation in a ballistic nanowire with hyperfine and Rashba spin-orbit interactions (SOI) and in the presence of magnetic field and electron interactions. The relaxation rate shows pronounced peaks as function of magnetic field and chemical potential due to van Hove singularities in the Rashba bands. As a result, the regimes of weak and strong SOIs can be distinguished by the number of peaks in the rate. The relaxation rate increases with increasing magnetic field if both Rashba subbands are occupied, whereas it decreases if only the lowest one is occupied.

7.1 Introduction

In this work, we propose an alternative and non-invasive way to access information about the SOI and the helical regime in a Rashba nanowire, namely via the nuclear spins. These are sensitive to the electronic state due to the hyperfine interaction present in III-V semiconductors such as GaAs or InAs.

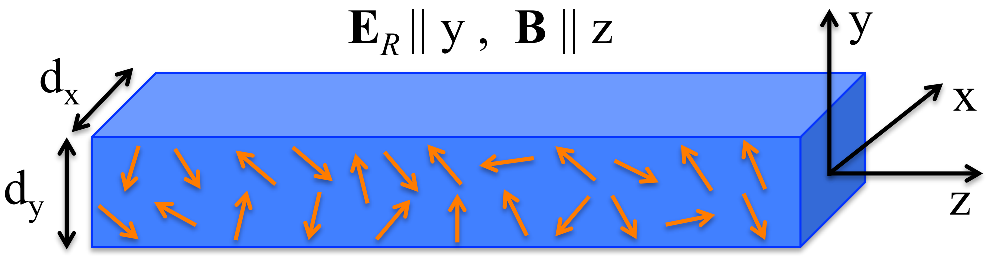

Figure 7.1: Schematics of a nanowire of cross-sectional area, $d_x \times d_y$, confining a one-dimensional electron gas with Rashba electric field $\mathbf{E}_R$ directed along y-axis and with magnetic field $\mathbf{B}$ along z-axis. The itinerant electrons are coupled by hyperfine interaction to localized nuclear spins (arrows). The Fermi wave-length $\lambda_F \approx d_x, d_y$ is much larger than the lattice spacing between nuclear spins.

A main motivation for our proposal stems from striking experimental progress in the field of nanoscale magnetometry. In particular, it has recently been demonstrated that cantilever-based magnetic sensing enables the nuclear spin magnetometry of nanostructures, in particular of InP and GaP nanowires [202]. In the remainder, we show how such ultrasensitive techniques can be used to probe the strength of the SOI, and to detect the helical states via the Korringa nuclear spin relaxation mechanism, i.e. the change of the nuclear spin state due to the spin-flip scattering of itinerant electrons of energies within the thermally broadened region close to the Fermi level [110].

We evaluate the nuclear spin relaxation rate in a one-dimensional ballistic electron gas in the presence of Rashba SOI and magnetic field. We first derive an explicit dependence of the nuclear relaxation rate on the parameters of the electronic spectrum for non-interacting electrons, in which the relaxation rate is proportional to the electronic temperature. We then discuss how electron interactions modify this temperature dependence to an interaction-dependent power law.

We find that the relaxation rate shows distinct peaks as function of magnetic field and chemical potential due to van Hove singularities in the Rashba bands. Remarkably, the regime of weak SOI is characterized by one peak while the one of strong SOI by three peaks. The relaxation rate for weak SOI vanishes as a function of μ if the Zeeman energy exceeds μ. Strong SOI gives rise to regions in the spectrum with negative group velocity and thus to pronounced peaks in the relaxation rate as function of μ. Finally, we show that the relaxation rate increases with increasing Zeeman energy if the Fermi level crosses both Rashba bands, while the rate decreases if only the lowest Rashba subband is occupied.

The outline of this Chapter is as follows. In Sec. II, we introduce the model Hamiltonian and derive the nuclear spin relaxation for non-interacting electrons for a Rashba band due to the hyperfine interaction. In Sec. III, we include electron-electron interactions described by a Luttinger liquid approach. In Sec. IV, we give numerical estimates for the nuclear spin relaxation making use of the material parameters appropriate for In-based nanowires.

7.2 Relaxation in a non-interacting electron gas

We consider nuclear spins coupled by hyperfine interaction to itinerant electrons in a semiconducting quantum or nano-wire with Rashba SOI. Our goal is to calculate the nuclear spin relaxation rate, first without electron-electron interactions. We assume the electrons to occupy the lowest transverse subband of the wire with cross-sectional area $d_x \times d_y$, see Fig. (7.1), described by the wave function

$$\Psi(x,y) = \frac{2}{\sqrt{d_x d_y}} \cos(\pi x/d_x)\cos(\pi y/d_y). \tag{7.1}$$

Taking into account that the nuclear density in the wire is much larger than the electron density we can approximate the wave function $|\Psi(x,y)| \approx 2/\sqrt{d_x d_y}$ by its value at the centre of the wire and sum over the nuclear spin density in the transverse direction. The Hamiltonian of the system becomes ($\hbar = 1$)

$$\begin{aligned} H = &\int dz c_s^\dagger(z)\left[-\left(\frac{\partial_z^2}{2m}+\mu\right)\delta_{ss'} - i\alpha\sigma_{ss'}^x\partial_z + h\sigma_{ss'}^z\right]c_{s'}(z) + \\ &+\int dz\left[\frac{\sqrt{d_x d_y}}{2}A\boldsymbol{I}(z)\cdot\frac{\boldsymbol{\sigma}_{ss'}}{2}c_s^\dagger(z)c_{s'}(z) - \omega_N I^z(z)\right]. \end{aligned} \tag{7.2}$$

Here, μ is the chemical potential of the electrons with effective mass m and spin projection s, where summation over repeated spin indexes is implied, α is the SOI constant, $h = g_e\mu_B B/2$ the Zeeman energy of the electrons due to the external magnetic field, B, applied along the z axis, where g_e is the electron g-factor and μ_B the Bohr magneton, $\sigma^{x,y,z}$ the Pauli matrices, and $A = A_{3D}4/(d_x d_y)$, where A_{3D} is the bulk value of the hyperfine interaction constant between a nuclear spin and the spin of an electron. We assume that the dominant contribution to the hyperfine interaction is given by Fermi contact interaction.

The nuclear spin density is given by $\mathbf{I}(z) = N_\perp \sum_j \mathbf{I}_j \delta(z-z_j)$, where $\mathbf{I}_j$ is the spin operator of the j-th nuclei, $N_\perp$ is the number of nuclear spins in the plane transverse to the wire axis, and the sum runs over the nuclear spins the wire axis. We assume that the Zeeman energy of the nuclear spins induced by the external magnetic field, $\omega_N = g_N \mu_N B$, where μ_N and g_N are the nuclear magneton and the effective g-factor, respectively, is small compared to the temperature T. We also assume temperature to be larger than the Kondo temperature associated with the localized spin.

It is convenient to express the single-particle Green function in the Rashba eigenbasis (for $A = 0$),

$$G_{ss'}(p, \epsilon_n) = \frac{1}{2} \sum_{\lambda=\pm 1} \frac{\delta_{ss'} - \lambda \frac{\alpha p \sigma^x_{ss'} + h \sigma^z_{ss'}}{\sqrt{\alpha^2 p^2 + h^2}}}{i\epsilon_n - \epsilon_\lambda(p)}, \tag{7.3}$$

where $\epsilon_\lambda(p) = p^2/2m - \mu - \lambda\sqrt{\alpha^2 p^2 + h^2}$ is the electron spectrum and p the momentum in the Rashba spin-split subband defined by $\lambda = \pm 1$; $\epsilon_n = (2n+1)\pi T$ is the fermionic Matsubara frequency.

We can now calculate the nuclear spin relaxation rate $1/T_1$ in a one-dimensional electron gas with SOI and Zeeman energy in second order perturbation theory in the hyperfine interaction between the nuclear spin and electron spin density. The relaxation rate is determined by the dynamical spin susceptibility of the conduction electrons at the nuclear site as [110, 206]:

$$\frac{1}{T_1} = \lim_{\omega_N \to 0} \frac{T A^2}{\omega_N} \int \frac{dq}{2\pi} \mathrm{Im}[\chi_{xx}(q, \omega_k)|_{i\omega_k \to \omega_N + i0^+}], \tag{7.4}$$

where $\omega_k = 2\pi k T$ is the bosonic Matsubara frequency and we take the analytical continuation of the spin susceptibility, which for noninteracting electrons is given by,

$$\begin{aligned} \chi_{ab}(q, \omega_k) &= -\frac{T}{2} \int \frac{dp}{2\pi} \sum_n G_{ss_1}(p+q, \epsilon_n + \omega_k) \sigma^a_{s_1 s_2} \\ &\times G_{s_2 s_3}(p, \epsilon_n) \sigma^b_{s_3 s}\,. \end{aligned} \tag{7.5}$$

Summing over spin indexes and Matsubara frequencies and taking the limit $\omega_N \to 0$ we obtain,

$$\begin{aligned}\frac{1}{T_1} &= -\frac{\pi A^2 T}{8}\sum_{\lambda,\lambda'}\int \frac{dpdq}{4\pi^2}\delta(\epsilon_\lambda(p)-\epsilon_{\lambda'}(q))\frac{\partial n_F(\epsilon)}{\partial\epsilon}\bigg|_{\epsilon=\epsilon_\lambda(p)} \\ &\times \left[\delta_{ss_1}-\frac{\lambda h\sigma^z_{ss_1}}{\sqrt{\alpha^2p^2+h^2}}\right]\sigma^x_{s_1s_2}\left[\delta_{s_2s_3}-\frac{\lambda' h\sigma^z_{s_2s_3}}{\sqrt{\alpha^2q^2+h^2}}\right]\sigma^x_{s_3s},\end{aligned} \tag{7.6}$$

where $n_F(\epsilon)$ is the Fermi distribution function.

We integrate over momentum and obtain the relaxation rate in the linear temperature regime as,

$$\begin{aligned}\frac{1}{T_1} &= \frac{\Theta(h^2+m^2\alpha^4+2m\alpha^2\mu)}{h^2+m^2\alpha^4+2m\alpha^2\mu}\Big\{m\alpha^2(\Theta(E_+)+\Theta(E_-)) \\ &+ 2\frac{\Theta(\mu^2-h^2)}{\sqrt{\mu^2-h^2}}(h^2+m\alpha^2\mu)\mathrm{sign}(h^2+2m\alpha^2\mu)\Big\}\frac{mA^2T}{4\pi},\end{aligned} \tag{7.7}$$

where $E_\pm = \mu + m\alpha^2 \pm \sqrt{h^2+m^2\alpha^4+2m\alpha^2\mu}$; $\Theta(x)$ and $\mathrm{sign}(x)$ are the Heaviside and sign functions, respectively. The dependencies of the relaxation rate on the chemical potential μ and the Zeeman energy h are plotted in Figs. 7.2 and 7.3, respectively.

Let us now consider the relaxation rate in several limiting regimes of the electronic spectrum. Without the SOI, *i.e.*, $\alpha = 0$, we obtain,

$$\frac{1}{T_1} = \frac{mA^2T}{2\pi}\frac{\Theta(\mu^2-h^2)}{\sqrt{\mu^2-h^2}}, \tag{7.8}$$

which in the absence of a magnetic field, $h = 0$, leads to the well-known result for the Korringa relaxation rate, $T_K^{-1} = \pi T A^2\nu^2$, where $\nu = 1/(\pi v_F)$ is the density of states per spin in the one-dimensional electron gas. If the chemical potential is smaller than the Zeeman energy, $|\mu| < |h|$, then the relaxation rate $1/T_1$ vanishes. Physically, this expresses the fact that the nuclear spin polarization cannot decay via flip-flop processes with the electrons if the latter are spin polarized due to the presence of a large Zeeman field. We note that the present calculation does not take into account competing nuclear spin relaxation mechanisms.

In the vicinity of the van-Hove singularity, $\mu \gtrsim h > 0$, see Fig. 7.2, the relaxation rate scales with the chemical potential as

$$T_1^{-1} = \frac{mA^2T}{4\pi}\frac{\Theta(\mu-h)}{h+m\alpha^2}\sqrt{\frac{2h}{\mu-h}}. \tag{7.9}$$

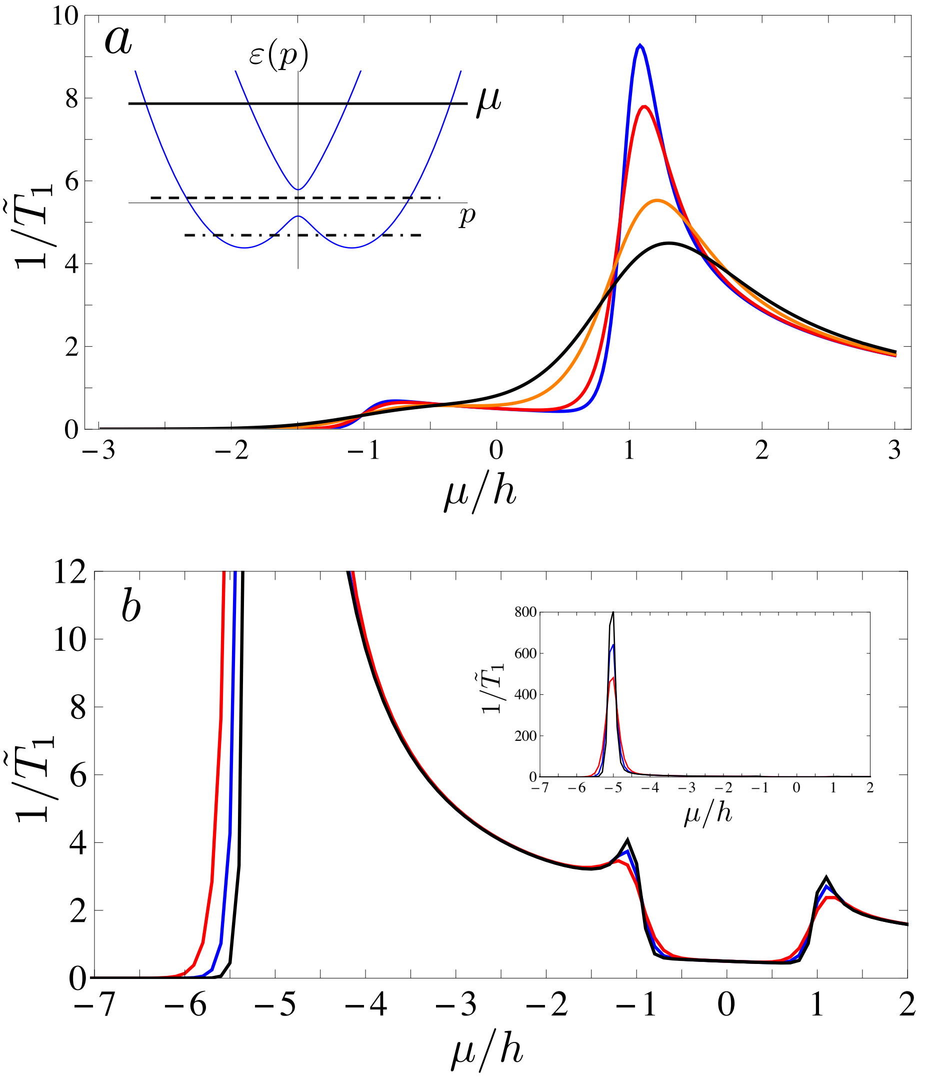

Figure 7.2: The nuclear spin relaxation rate $1/\tilde{T}_1 = T_1(0)/(2T_1(\mu/h))$ as function of μ/h for small (a) and large (b) SOI strengths $m\lambda^2/h = 0.2$ and $m\lambda^2/h = 10$, respectively, as numerically obtained from Eq. (7.6). The rate is normalized by its value at $\mu = 0$ (we set $\mu = 0$ at the middle of the Zeeman gap between the Rashba subbands at $p = 0$). The pronounced peaks are due to van Hove singularities at the edges of the Rashba subbands. (a) Curves from top to bottom are for $T/h = 0.07, 0.1, 0.2, 0.3$, respectively. (b) Curves from top to bottom are for $T/h = 0.05, 0.07, 0.1$, respectively. Inset (a): The Rashba spectrum with possible Fermi levels (lines). Strong SOI gives rise to regions in the spectrum (dashed-dotted line) with negative group velocity and non-monotonic relaxation rate as shown in (b). The strong increase of the rate for μ/h approaching the band bottom $E_0/h = -5$ (see also inset (b)) signals the breakdown of perturbation theory.

On the other hand, in the presence of both SOI and magnetic field, tuning the chemical potential to the middle of the gap of the spectrum at $p = 0$, $\mu = 0$, we obtain,

$$\frac{1}{T_1} = \frac{mA^2T}{4\pi} \frac{m\alpha^2}{h^2 + m^2\alpha^4} \, . \tag{7.10}$$

We note that the relaxation rate diverges at the van Hove singularities of the spectrum occurring at zeroes of $\partial\epsilon_\lambda(p)/\partial p$. For instance, $1/T_1 \sim [h(\mu - h)]^{-1/2}$ for weak SOI and $\mu > h$, and $1/T_1 \sim |\mu - E_0|^{-1}$ for strong SOI, where E_0 denotes the band bottom. Formally, the perturbation expansion in A for the rate breaks down at these singularities. However, these singularities turn into well-defined peaks by finite-temperature effects, as we confirmed by evaluating Eq. (7.6) numerically for various temperatures, see Figs. 7.2 and 7.3. The peak at E_0, however, remains large also for $T > 0$ and thus is outside the perturbative regime considered here. As an important result, we see that the relaxation rate behaves qualitatively very different for weak and for strong SOIs: in the former case, there is only one peak, while in the latter there are three peaks in $1/T_1$ as function of μ, see Figs. 7.2(a) and 7.2(b).

Finally, let us discuss the dependence of the relaxation rate on the magnetic field h. The relaxation rate increases with the increase of the Zeeman energy as $\sim h^2/\mu^2$ for $\mu > m\alpha^2$ if the Fermi level crosses both Rashba subbands, see Fig. 7.3(a) and inset in Fig. 7.2(a), where the position of the Fermi level is shown by the solid line. On the other hand, the relaxation rate decreases with increase of the Zeeman energy as $\sim -h^2/m^2\alpha^4$ for $|\mu| < m\alpha^2$ if the Fermi level crosses only the lowest Rashba subband, see Fig. 7.3(b) and inset in Fig. 7.2(a), where the position of the Fermi level is shown by the dashed-dotted line. The singularity of the relaxation rate shown in Figs. 7.3(a) and 7.3(b) corresponds to the condition when $h = |\mu|$.

7.3 Relaxation in an interacting electron system

In a one-dimensional system, electron-electron interactions modify the temperature dependence of the nuclear spin relaxation rate from a linear scaling to interaction dependent power laws. We derive these in a Luttinger liquid calculation valid when the chemical potential is sufficiently far from the van Hove singularities, so that the dispersion can be linearized. For $|\mu| \gg |h|$, $m\alpha^2$, the system can be understood as

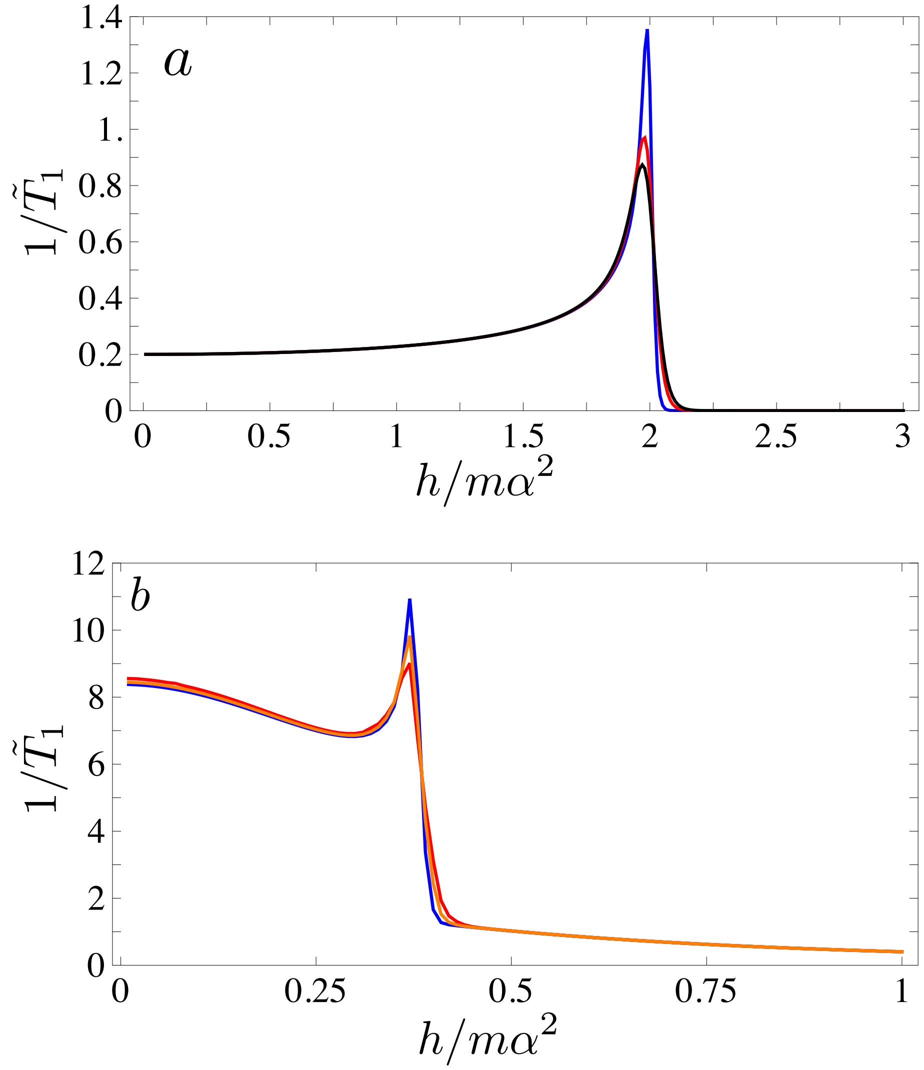

Figure 7.3: Nuclear spin relaxation rate $1/\tilde{T}_1 = T_1(h = 0)_{\mu=0}/(2T_1(h/m\alpha^2))$ as a function of Zeeman energy h normalized by the SOI energy $h/m\alpha^2$ for two cases: (a) $\mu/m\alpha^2 = 2$, $T/m\alpha^2 = 0.01, 0.02, 0.025$. The corresponding Fermi level is shown by the solid line in Fig. 7.2(a). (b) $\mu/m\alpha^2 = -0.38$, $T/m\alpha^2 = 0.005, 0.0075, 0.01$. The corresponding Fermi level is shown by the dashed-dotted line in Fig. 7.2(a). Note that the singularities are smoothened into finite peaks by temperature effects.

a spinful Luttinger liquid with subleading corrections due to the SOI and the magnetic field. Neglecting these subleading terms, we first decompose the fermionic operators into their right and left moving parts, $c_s(z) \approx e^{izk_F} R_s(z) + e^{-izk_F} L_s(z)$, where k_F is the Fermi momentum. Next, we bosonize these operators using standard techniques [36] as $r_s(z) = U_{rs}/\sqrt{2\pi a_0}\exp(-i(r\phi_c(z) + rs\phi_\sigma(z) - \theta_c(z) - s\theta_\sigma(z))/\sqrt{2})$, where U_{rs} is a Klein factor, and a_0 is the short distance cutoff of the Luttinger liquid theory (this cutoff is of the order of the lattice constant). The parameters $r = R, L \equiv +1, -1$ and $s = \uparrow, \downarrow \equiv +1, -1$ denote the direction of motion and the spin, respectively, while the bosonic fields ϕ_i are proportional to the integrated charge ($i = c$) or spin ($i = \sigma$) density, θ_i is proportional to the integrated charge or spin current, and $[\phi_i(z), \theta_j(z')] = \delta_{ij}(i\pi/2)\mathrm{sgn}(z' - z)$. The effect of electron-electron interactions is captured by a Luttinger liquid parameter $1 \geq K_c \geq 0$ for the charge fluctuations (we take the Luttinger parameter in the spin sector to be $K_\sigma \approx 1$), such that the Luttinger liquid Hamiltonian reads $H = \int \frac{dz}{2\pi} \sum_{i=c,\sigma} \left[\frac{u_i}{K_i}(\partial_z\phi_i)^2 + u_i K_i(\partial_z\theta_i)^2\right]$, where u_c (u_σ) is the effective velocity in the charge (spin) sector. This Hamiltonian in turn allows us to calculate the relaxation rate T_1^{-1} for interacting electrons. We first bosonize the real space, imaginary time susceptibility $\chi_{xx}(z, \tau)$ according to the above prescription, which yields

$$\begin{aligned}
\chi_{xx}(z,\tau) &= \sum_{r,r'} \frac{\langle T_\tau r_\uparrow^\dagger(z,\tau) r'_\downarrow(z,\tau) r'^\dagger_\downarrow(0,0) r_\uparrow(0,0)\rangle}{4} + \text{h.c.} \\
&= \sum_{r,r'} \frac{-e^{-i(r-r')zk_F}}{4(2\pi a_0)^2} \langle T_\tau\, e^{i(\tilde{\phi}_{rr'}(z,\tau) - \tilde{\phi}_{rr'}(0,0))}\rangle \\
&\quad + \text{h.c.}\,, \qquad (7.11)
\end{aligned}$$

with $\tilde{\phi}_{rr'}(z,\tau) = ((r-r')\phi_c(z,\tau) + (r+r')\phi_\sigma(z,\tau) - 2\theta_\sigma(z,\tau))/\sqrt{2}$. From this expression, the retarded spin susceptibility as a function of frequency can be calculated by virtue of a Wick rotation to real time, and a subsequent Fourier transformation [36]. Eq. (7.4) then yields the relaxation time as

$$\frac{1}{T_1} \approx \mathcal{T}(\mu, K_c)\, T + \widetilde{\mathcal{T}}(\mu, K_c)\, T^{K_c}\,. \qquad (7.12)$$

Here, $\mathcal{T}(\mu, K_c)$ and $\widetilde{\mathcal{T}}(\mu, K_c)$ are prefactors which in general depend on the short distance cutoff a_0, and which reduce to $\mathcal{T}(\mu, 1) = \widetilde{\mathcal{T}}(\mu, 1) = \frac{mA^2}{4\pi\mu}$

in the non-interacting limit. This is the expected scaling for the Korringa law in a Luttinger liquid, in which forward scattering gives rise to the term $\sim T$, while backscattering results in the contribution $\sim T^{K_c}$ [36].

In the limit $m\alpha^2 \gg |h| \gg |\mu|$, the system is to a good approximation helical (half of the spectrum is gapped, see Fig. 7.2(a), while the gapless modes move in opposite directions and have antiparallel spins). In this case, all terms in Eq. (7.11) involving the gapped modes (i.e. right and left movers of the "wrong" spin polarization) are negligibly small, while the contribution of the gapless helical modes can be derived from an effective spinless Luttinger liquid Hamiltonian. The latter can either be obtained by linearizing the gapless helical modes and then bosonizing these, or by starting from the full Luttinger liquid Hamiltonian including right and left movers of both spin species and integrating out the gapped degrees of freedom along the lines of Ref. [198]. In the latter case, the Luttinger liquid parameter of the helical modes relates to the ones in the spin and charge sectors as $K_{\text{hel}} = 2K_c\sqrt{u_c u_\sigma}/\sqrt{(u_c + K_c K_\sigma u_\sigma)(u_\sigma + u_c K_c K_\sigma)}$ (this implies $1 \geq K_{\text{hel}} \geq 0$), while their effective velocity is given by $\sqrt{u_c u_\sigma(u_c + u_\sigma K_c K_\sigma)}/\sqrt{u_\sigma + u_c K_c K_\sigma}$ [182]. Using these effective parameters, we find that the contribution of the gapless modes to $\chi_{xx}(0,\tau)$ is:

$$\chi_{xx}(0,\tau) = \frac{-1}{8(\pi a_0)^2} \frac{(\pi a_0 T/u_{\text{hel}})^{2K_{\text{hel}}}}{[\sinh(i\pi T\tau)\sinh(-i\pi T\tau)]^{K_{\text{hel}}}} \,. \tag{7.13}$$

This implies that the relaxation rate takes the form, [36]

$$\frac{1}{T_1} \approx \mathcal{T}_{\text{hel}}(\alpha, K_{\text{hel}})\, T^{2K_{\text{hel}}-1} \,, \tag{7.14}$$

where $\mathcal{T}_{\text{hel}}(\alpha, K_{\text{hel}})$ is again a cutoff-dependent prefactor that reduces to $\mathcal{T}_{\text{hel}}(\alpha, 1) = \frac{A^2}{4\pi\alpha^2}$ in the non-interacting limit. This power law complies with the fact that in the helical regime the nuclear spin relaxation results from electronic backscattering processes only. Quite remarkably, for strong interaction such that $K_{\text{hel}} < 1/2$ the relaxation rate increases with decreasing temperature, in stark contrast to weak or absent interactions where the rate decreases with decreasing temperature.

For $m\alpha^2 \gg |\mu| \gg |h|$, the system is gapless, and thus shows a scaling of the type given in Eq. (7.12). For $|h| \gg |\mu|$, $m\alpha^2$, finally, the system essentially behaves like a spinful wire with a Zeeman splitting between spin up and spin down in which only the lower of the two Zeeman-split band is occupied. In this case, we obtain $T_1^{-1} \approx 0$, which follows from Eq. (7.8), as well as from Eq. (7.10) in the limit $m\alpha^2/h \to 0$.

7.4 Conclusions

Let us now comment on the experimental observability of the predicted behavior of the nuclear spin relaxation rates in InAs nanowires. For an InAs nanowire with a cross-sectional area of $d_x \times d_y = 50 \times 50$ nm^2, and with Fermi velocity $v_F = 3 \times 10^6$ cm/s, we obtain for the one-dimensional density of states $\nu = 1/(\pi\hbar v_F) \approx 16$ (eVnm)$^{-1}$. For an electron g-factor $g = 8$, the Zeeman energy $h \approx 4$ K at a magnetic field of 1 T, requires correspondingly low temperatures, $T \lesssim 4$ K. The dominant hyperfine coupling comes from In with nuclear spin $I = 9/2$ and bulk constant $A_{3D} = 3$ μeVnm^3. With this, we estimate the nuclear spin relaxation time $T_K \approx (\frac{d_x d_y}{4\nu A_{3D}})^2 \frac{\hbar}{\pi k_B T} \approx 380$ s, at $T = 1$K. Remarkably, this estimate for T_K is consistent with recent measurements performed on InP nanowires with cantilever techniques [202].

The phonon-assisted relaxation mechanism can be distinguished by the temperature dependence of the relaxation rate, $1/T_1^{\rm ph} \sim T^7$ (T^2) for T smaller (larger) than the Debye temperature [207], which is 280K in InAs. The effect of the nuclear dipole-dipole interaction on the nuclear relaxation can be suppressed by small magnetic fields of the order of few mT when the nuclear Zeeman splitting is larger than the dipolar energy [208].

Hence, we conclude that the hyperfine contact interaction is the most important term for describing nuclear spin relaxation in In-based nanowires with s-type conduction band at low temperatures. Again, this conclusion is supported by recent experiments [202], which measured values for T_K of the same order as found above for the hyperfine interaction.

The measurement of the Rashba and Dresselhaus SOI coefficients via weak antilocalization (WAL) effects in quasi-one dimensional InGaAs wires was recently reported in Ref. [209] These 750nm wide wires with several transverse conduction channels were treated as quasi-one dimensional due to the fact that the spin-relaxation length is much larger than the width of the wire. For a 1D wire with only a single conduction channel the WAL mechanism does not work, in contrast to the mechanism of the nuclear spin relaxation proposed here. The nuclear relaxation rate measures directly the spectrum of the electrons via the density of states, while the WAL signal is more indirect, and could also be strongly affected by 'extrinsic' spin orbit effects, Elliot-Yafet effect, etc. Thus, it seems worthwhile to search experimentally for the predicted signatures of the SOI in the relaxation rate as a function of magnetic field, chemical potential, and temperature.

7.5 Acknowledgements

We thank M. Poggio and D. Becker for discussions and acknowledge support from the Swiss NSF and NCCR QSIT.

Bibliography

[1] B. Braunecker, P. Simon, and D. Loss, Phys. Rev. Lett. **102**, 116403 (2009).

[2] D. P. DiVincenzo, in *Mesoscopic Electron Transport,* edited by L. Kowenhoven, G. Schoen, and L. Sohn, NATO ASI Series (Kulwer Academic Press, Dordrecht, 1997), Vol. 345, pp. 657-677.

[3] D. Loss and D. P. DiVincenzo, Phys. Rev. A **57**, 120 (1998).

[4] J. Levy, Phys. Rev. Lett. **89**, 147902 (2002).

[5] J. R. Petta, A. C. Johnson, J. M. Taylor, E. A. Laird, A. Yacoby, M. D. Lukin, C. M. Marcus, M. P. Hanson, and A. C. Gossard, Science **309**, 2180 (2005).

[6] S. Foletti, H. Bluhm, D. Mahalu, V. Umansky, and A. Yacoby, Nat. Phys. **5**, 903 (2009).

[7] H. Bluhm, S. Foletti, D. Mahalu, V. Umansky, and A. Yacoby, Phys. Rev. Lett. **105**, 216803 (2010).

[8] H. Bluhm, S. Foletti, I. Neder, M. Rudner, D. Mahalu, V. Umansky, and A. Yacoby, Nature **7**, 109 (2011).

[9] J. R. Petta, J. M. Taylor, A. C. Johnson, A. Yacoby, M. D. Lukin, C. M. Marcus, M. P. Hanson, and A. C. Gossard, Phys. Rev. Lett. **100**, 067601 (2008).

[10] O. E. Dial, M. D. Shulman, S. P. Harvey, H. Bluhm, V. Umansky, and A. Yacoby, Phys. Rev. Lett. **110**, 146804 (2013).

[11] G. Dresselhaus, Phys. Rev. **100**, 580 (1955).

[12] A. V. Khaetskii, Y. V. Nazarov, Phys. Rev. B **61**, 12639 (2000).

[13] Vitaly N. Golovach, Massoud Borhani, and Daniel Loss, Phys. Rev. B **74**, 165319 (2006).

[14] J. You, H.-O. Li, K. Wang, G. Cao, X.-X. Song, M. Xiao, and G.-P. Guo, Appl. Phys. Lett. **107**, 233104 (2015).

[15] S. Chesi, Y.-D. Wang, J. Yoneda, T. Otsuka, S. Tarucha, and D. Loss, Phys. Rev. B **90**, 235311 (2014).

[16] E. Kawakami, P. Scarlino, D. R. Ward, F. R. Braakman, D. E. Savage, M. G. Lagally, M. Friesen, S. N. Coppersmith, M. A. Eriksson, and L. M. K. Vandersypen, Nat. Nanotechnol. **9**, 666 (2014).

[17] X. Wu, D. R. Ward, J. R. Prance, D. Kim, J. K. Gamble, R. T. Mohr, Z. Shi, D. E. Savage, M. G. Lagally, M. Friesen, S. N. Coppersmith, and M. A. Eriksson, Proc. Natl. Acad. Sci. (U. S. A.), **111**, 11938 (2014).

[18] Y.-S. Shin, T. Obata, Y. Tokura, M. Pioro-Ladriére, R. Brunner, T. Kubo, K. Yoshida, and S. Tarucha, Phys. Rev. Lett. **104**, 046802 (2010).

[19] S. S. P. Parkin, M. Hayashi, and L. Thomas, Science **320**, 190 (2008).

[20] D. Rugar, H. J. Mamin, M. H. Sherwood, M. Kim, C. T. Rettner, K. Ohno, and D. D. Awschalom, Nat. Nanotechnol. **10**, 120 (2015).

[21] T. Dietl, A. Haury, and Y. M. d'Aubigné, Phys. Rev. B **55**, R3347 (1997).

[22] H. Ohno, Science **281**, 951 (1998).

[23] P. Simon and D. Loss, Phys. Rev. Lett. **98**, 156401 (2007).

[24] P. Simon, B. Braunecker, and D. Loss, Phys. Rev. B **77**, 045108 (2008).

[25] H. Ohno, D. Chiba, F. Matsukura, T. Omiya, E. Abe, T. Dietl, Y. Ohno, and K. Ohtani, Nature (London) **408**, 944 (2000).

[26] D. Chiba, M. Sawicki, Y. Nishitani, Y. Nakatani, F. Matsukura, and H. Ohno, Nature (London) **455**, 515 (2008).

[27] D. Chiba, T. Ono, F. Matsukura, and H. Ohno, Appl. Phys. Lett. **103**, 142418 (2013).

[28] B. Braunecker, P. Simon, and D. Loss, Phys. Rev. B **80**, 165119 (2009).

[29] C. P. Scheller, T.-M. Liu, G. Barak, A. Yacoby, L. N. Pfeiffer, K. W. West, and D. M. Zumbühl, Phys. Rev. Lett. **112**, 066801 (2014).

[30] J. C. Slonczewski, J. Magn. Magn. Mater. **159**, L1 (1996).

[31] L. Berger, Phys. Rev. B **54**, 9353 (1996).

[32] M. Yamanouchi, D. Chiba, F. Matsukura, and H. Ohno, Nature **428**, 539 (2004).

[33] V. K. Dugaev, V. R. Vieira, P. D. Sacramento, J. Barnaś, M. A. N. Araújo, and J. Berakdar, Phys. Rev. B **74**, 054403 (2006).

[34] L. Berger, J. Phys. Chem. Solids **35**, 947 (1974).

[35] C.-Y. Hung and L. Berger, J. Appl. Phys. **63**, 4276 (1988).

[36] T. Giamarchi, *Quantum Physics in One Dimension* (Oxford University Press, New York, 2003).

[37] J. Voit, Rep. Prog. Phys. **58**, 9 (1995).

[38] C. Kloeffel and D. Loss, Annu. Rev. Condens. Matter Phys. **4**, 51 (2013).

[39] J. R. Petta, A. C. Johnson, J. M. Taylor, E. A. Laird, A. Yacoby, M. D. Lukin, C. M. Marcus, M. P. Hanson, and A. C. Gossard, Science **309**, 2180 (2005).

[40] M. D. Shulman, O. E. Dial, S. P. Harvey, H. Bluhm, V. Umansky, A. Yacoby, Science **336**, 202 (2012).

[41] J. Klinovaja, D. Stepanenko, B. I. Halperin, and D. Loss, Phys. Rev. B **86**, 085423 (2012).

[42] A. V. Khaetskii, D. Loss, and L. Glazman, Phys. Rev. Lett. **88**, 186802 (2002).

[43] I. A. Merkulov, A. L. Efros, and M. Rosen, Phys. Rev. B **65**, 205309 (2002).

[44] W. A. Coish and D. Loss, Phys. Rev. B **70**, 195340 (2004).

[45] A. C. Johnson, J. R. Petta, J. M. Taylor, A. Yacoby, M. D. Lukin, C. M. Marcus, M. P. Hanson, and A. C. Gossard, Nature (London) **435**, 925 (2005).

[46] C. Barthel, J. Medford, C. M. Marcus, M. P. Hanson, and A. C. Gossard, Phys. Rev. Lett. **105**, 266808 (2010).

[47] H. Bluhm, S. Foletti, I. Neder, M. Rudner, D. Mahalu, V. Umansky, and A. Yacoby, Nat. Phys. **7**, 109 (2011).

[48] J. Medford, L. Cywinski, C. Barthel, C. M. Marcus, M. P. Hanson, and A. C. Gossard, Phys. Rev. Lett. **108**, 086802 (2012).

[49] A. P. Higginbotham, F. Kuemmeth, M. P. Hanson, A. C. Gossard, and C. M. Marcus, Phys. Rev. Lett. **112**, 026801 (2014).

[50] G. Burkard, D. Loss, and D. P. DiVincenzo, Phys. Rev. B **59**, 2070 (1999).

[51] J. M. Taylor, H.-A. Engel, W. Dür, A. Yacoby, C. M. Marcus, P. Zoller, and M. D. Lukin, Nat. Phys. **1**, 177 (2005).

[52] S. Foletti, H. Bluhm, D. Mahalu, V. Umansky, and A. Yacoby, Nat. Phys. **5**, 903 (2009).

[53] M. D. Shulman, O. E. Dial, S. P. Harvey, H. Bluhm, V. Umansky, and A. Yacoby, Science **336**, 202 (2012).

[54] J. Yoneda, T. Otsuka, T. Nakajima, T. Takakura, T. Obata, M. Pioro-Ladrière, H. Lu, C. J. Palmstrøm, A. C. Gossard, and S. Tarucha, Phys. Rev. Lett. **113**, 267601 (2014).

[55] P. Scarlino, E. Kawakami, P. Stano, M. Shafiei, C. Reichl, W. Wegscheider, and L. M. K. Vandersypen, Phys. Rev. Lett **113**, 256802 (2014).

[56] P. Cerfontaine, T. Botzem, D. P. DiVincenzo, and H. Bluhm, Phys. Rev. Lett. **113**, 150501 (2014).

[57] D. E. F. Biesinger, C. P. Scheller, B. Braunecker, J. Zimmerman, A. C. Gossard, and D. M. Zumbühl, Phys. Rev. Lett. **115**, 106804 (2015).

[58] M. P. Wardrop and A. C. Doherty, Phys. Rev. B **93**, 075436 (2016).

[59] F. Martins, F. K. Malinowski, P. D. Nissen, E. Barnes, S. Fallahi, G. C. Gardner, M. J. Manfra, C. M. Marcus, and F. Kuemmeth, arXiv:1511.07336.

[60] A. Laucht, R. Kalra, J. T. Muhonen, J. P. Dehollain, F. A. Mohiyaddin, F. Hudson, J. C. McCallum, D. N. Jamieson, A. S. Dzurak, and A. Morello, Appl. Phys. Lett. **104**, 092115 (2014).

[61] A. M. Tyryshkin, S. Tojo, J. J. L. Morton, H. Riemann, N. V. Abrosimov, P. Becker, H.-J. Pohl, T. Schenkel, M. L. W. Thewalt, K. M. Itoh, and S. A. Lyon, Nat. Mater. **11**, 143 (2012).

[62] S. J. Hile, M. G. House, E. Peretz, J. Verduijn, D. Widmann, T. Kobayashi, S. Rogge, and M. Y. Simmons, Appl. Phys. Lett. **107**, 93504 (2015).

[63] T. F. Watson, B. Weber, M. G. House, H. Büch, and M. Y. Simmons, Phys. Rev. Lett. **115**, 166806 (2015).

[64] J. J. Pla, F. A. Mohiyaddin, K. Y. Tan, J. P. Dehollain, R. Rahman, G. Klimeck, D. N. Jamieson, A. S. Dzurak, and A. Morello, Phys. Rev. Lett. **113**, 246801 (2014).

[65] B. E. Kane, Nature **393**, 133 (1998).

[66] C. D. Hill, E. Peretz, S. J. Hile, M. G. House, M. Fuechsle, S. Rogge, M. Y. Simmons, and L. C. L. Hollenberg, Science Advances **1**, e1500707 (2015).

[67] M. Usman, C. D. Hill, R. Rahman, G. Klimeck, M. Y. Simmons, S. Rogge, and L. C. L. Hollenberg, Phys. Rev. B **91**, 245209 (2015).

[68] M. Steger, K. Saeedi, M. L. W. Thewalt, J. J. L. Morton, H. Riemann, N. V. Abrosimov, P. Becker, and H.-J. Pohl, Science **336**, 1280 (2012).

[69] K. Saeedi, S. Simmons, J. Z. Salvail, P. Dluhy, H. Riemann, N. V. Abrosimov, P. Becker, H.-J. Pohl, J. J. Morton, and M. L. Thewalt, Science **342**, 830 (2013).

[70] G. W. Morley, P. Lueders, M. H. Mohammady, S. J. Balian, G. Aeppli, C. W. M. Kay, W. M. Witzel, G. Jeschke, and T. S. Monteiro, Nat. Mater. **12**, 103 (2013).

[71] J. T. Muhonen, A. Laucht, S. Simmons, J. P. Dehollain, R. Kalra, F. E. Hudson, S. Freer, K. M. Itoh, D. N. Jamieson, J. C. McCallum, A. S. Dzurak, and A. Morello, J. Phys. Condens. Matter **27**, 154205 (2015).

[72] M. Veldhorst, C. H. Yang, J. C. C. Hwang, W. Huang, J. P. Dehollain, J. T. Muhonen, S. Simmons, A. Laucht, F. E. Hudson, K. M. Itoh, A. Morello, and A. S. Dzurak, Nature **526**, 410 (2015).

[73] M. J. Calderón, B. Koiller, X. Hu, and S. Das Sarma, Phys. Rev. Lett. **96**, 096802 (2006).

[74] C. Kloeffel, M. Trif, and D. Loss,Phys. Rev. B **84**, 195314 (2011).

[75] Y. Hu, F. Kuemmeth, C. M. Lieber, and C. M. Marcus, Nat. Nanotechnol. **7**, 47 (2012).

[76] F. Maier, C. Kloeffel, and D. Loss, Phys. Rev. B **87**, 161305(R) (2013).

[77] C. Kloeffel, M. Trif, P. Stano, and D. Loss, Phys. Rev. B **88**, 241405(R) (2013).

[78] D. M. Zajac, T. M. Hazard, X. Mi, K. Wang, and J. R. Petta, Appl. Phys. Lett. **106**, 223507 (2015).

[79] K. Takeda, T. Obata, Y. Fukuoka, W. M. Akhtar, J. Kamioka, T. Kodera, S. Oda, and S. Tarucha, Appl. Phys. Lett. **102**, 123113 (2013).

[80] C. Tahan and R. Joynt, Phys. Rev. B **89**, 075302 (2014).

[81] F. A. Zwanenburg, A. S. Dzurak, A. Morello, M. Y. Simmons, L. C. L. Hollenberg, G. Klimeck, S. Rogge, S. N. Coppersmith, and M. A. Eriksson, Rev. Mod. Phys. **85**, 961 (2013).

[82] S. Goswami, K. A. Slinker, M. Friesen, L. M. McGuire, J. L. Truitt, C. Tahan, L. J. Klein, J. O. Chu, P. M. Mooney, D. W. van der Weide, R. Joynt, S. N. Coppersmith, and M. A. Eriksson, Nat. Phys. **3**, 41 (2007).

[83] M. Xiao, M. G. House, and H. W. Jiang, Appl. Phys. Lett. **97**, 032103 (2010).

[84] C. H. Yang, A. Rossi, R. Ruskov, N. S. Lai, F. A. Mohiyaddin, S. Lee, C. Tahan, G. Klimeck, A. Morello, and A. S. Dzurak, Nat. Commun. **4**, 2069 (2013).

[85] I. L. Aleiner and V. I. Fal′ko, Phys. Rev. Lett. **87**, 256801 (2001).

[86] V. N. Golovach, A. V. Khaetskii, and D. Loss, Phys. Rev. Lett. **93**, 016601 (2004).

[87] P. Stano and J. Fabian, Phys. Rev. B **72**, 155410 (2005).

[88] P. Stano and J. Fabian, Phys. Rev. Lett. **96**, 186602 (2006).

[89] V. N. Golovach, A. V. Khaetskii, and D. Loss, Phys. Rev. B **77**, 045328 (2008).

[90] M. Raith, P. Stano, F. Baruffa, and J. Fabian, Phys. Rev. Lett. **108**, 246602 (2012).

[91] E. A. Laird, C. Barthel, E. I. Rashba, C. M. Marcus, M. P. Hanson, and A. C. Gossard, Phys. Rev. Lett. **99**, 246601 (2007).

[92] M. Pioro-Ladrière, T. Obata, Y. Tokura, Y.-S. Shin, T. Kubo, K. Yoshida, T. Taniyama, and S. Tarucha, Nat. Phys. **4**, 776 (2008).

[93] R. Brunner, Y.-S. Shin, T. Obata, M. Pioro-Ladrière, T. Kubo, K. Yoshida, T. Taniyama, Y. Tokura, and S. Tarucha, Phys. Rev. Lett. **107**, 146801 (2011).

[94] D. Stepanenko, M. Rudner, B. I. Halperin, and D. Loss, Phys. Rev. B **85**, 075416 (2012).

[95] T. Meunier, I. T. Vink, L. H. Willems van Beveren, K-J. Tielrooij, R. Hanson, F. H. L. Koppens, H. P. Tranitz, W. Wegscheider, L. P. Kouwenhoven, and L. M. K. Vandersypen, Phys. Rev. Lett. **98**, 126601 (2007).

[96] M. Borhani, V. N. Golovach, and D. Loss, Phys. Rev. B **73**, 155311 (2006).

[97] A. N. Cleland, *Foundations of Nanomechanics: From Solid-State Theory to Device Applications* (Springer, Berlin, 2003).

[98] S. Adachi, *Properties of Group-IV, III-V and II-VI Semiconductors* (John Wiley & Sons, Chichester, 2005).

[99] http://www.ioffe.ru/SVA/NSM/Semicond/GaAs

[100] K. Hübner, Phys. Status Solidi B **57**, 627 (1973).

[101] S. Adachi, *GaAs and Related Materials: Bulk Semiconducting and Superlattice Properties* (World Scientific, Singapore, 1994).

[102] C. G. Van de Walle, Phys. Rev. B **39**, 1871 (1989).

[103] F. F. Fang and W. E. Howard, Phys. Rev. Lett. **16**, 797 (1966).

[104] A. V. Khaetskii and Y. V. Nazarov, Phys. Rev. B **64**, 125316 (2001).

[105] R. Hanson, L. P. Kouwenhoven, J. R. Petta, S. Tarucha, and L. M. K. Vandersypen, Rev. Mod. Phys. **79**, 1217 (2007).

[106] R. Winkler, *Spin-Orbit Coupling Effects in Two-Dimensional Electron and Hole Systems* (Springer, Berlin, 2003).

[107] D. V. Bulaev and D. Loss, Phys. Rev. Lett. **95**, 076805 (2005).

[108] M. Trif, P. Simon, and D. Loss, Phys. Rev. Lett. **103**, 106601 (2009).

[109] M. O. Hachiya, G. Burkard, and J. C. Egues, Phys. Rev. B **89**, 115427 (2014).

[110] C. P. Slichter, *Principles of Magnetic Resonance* (Springer, Berlin, 1980).

[111] K. Roszak and P. Machnikowski, Phys. Rev. B **80**, 195315 (2009).

[112] D. E. McCumber and M. D. Sturge, J. Appl. Phys. **34**, 1682 (1963).

[113] W. M. Yen, W. C. Scott, and A. L. Schawlow, Phys. Rev. **136**, A271 (1964).

[114] S. B. Altner, G. Zumofen, U. P. Wild, and M. Mitsunaga, Phys. Rev. B **54**, 17493 (1996).

[115] R. S. Meltzer, in *Spetroscopic Properties of Rare Earths in Optical Materials*, edited by G. Liu and B. Jacquier (Springer, Berlin, 2005), Chap. 4, pp. 191-265.

[116] J. Medford, J. Beil, J. M. Taylor, E. I. Rashba, H. Lu, A. C. Gossard, and C. M. Marcus, Phys. Rev. Lett. **111**, 050501 (2013).

[117] B. M. Maune, M. G. Borselli, B. Huang, T. D. Ladd, P. W. Deelman, K. S. Holabird, A. A. Kiselev, I. Alvarado-Rodriguez, R. S. Ross, A. E. Schmitz, M. Sokolich, C. A. Watson, M. F. Gyure, and A. T. Hunter, Nature (London) **481**, 344 (2012).

[118] J. R. Prance, Z. Shi, C. B. Simmons, D. E. Savage, M. G. Lagally, L. R. Schreiber, L. M. K. Vandersypen, M. Friesen, R. Joynt, S. N. Coppersmith, and M. A. Eriksson, Phys. Rev. Lett. **108**, 046808 (2012).

[119] D. Stepanenko, N. E. Bonesteel, D. P. DiVincenzo, G. Burkard, and D. Loss, Phys. Rev. B **68**, 115306 (2003).

[120] V. F. Gantmakher and Y. B. Levinson, *Carrier Scattering in Metals and Semiconductors* (North-Holland, Amsterdam, 1987).

[121] U. Rössler, *Solid State Theory: An Introduction* (Springer, Berlin, 2009), 2nd edition.

[122] P. Y. Yu and M. Cardona, *Fundamentals of Semiconductors: Physics and Materials Properties* (Springer, Berlin, 2010), 4th edition.

[123] K. A. Benedict, R. K. Hills, and C. J. Mellor, Phys. Rev. B **60**, 10984 (1999).

[124] M. Prada, R. H. Blick, and R. Joynt, Phys. Rev. B **77**, 115438 (2008).

[125] M. Raith, P. Stano, and J. Fabian, Phys. Rev. B **86**, 205321 (2012).

[126] D. Culcer, L. Cywiński, Q. Li, X. Hu, and S. Das Sarma, Phys. Rev. B **80**, 205302 (2009).

[127] J.-T. Hung, L. Cywiński, X. Hu, and S. Das Sarma, Phys. Rev. B **88**, 085314 (2013).

[128] L. V. C. Assali, H. M. Petrilli, R. B. Capaz, B. Koiller, X. Hu, and S. Das Sarma, Phys. Rev. B **83**, 165301 (2011).

[129] D. Culcer, A. L. Saraiva, B. Koiller, X. Hu, and S. Das Sarma, Phys. Rev. Lett. **108**, 126804 (2012).

[130] C. B. Simmons, J. R. Prance, B. J. Van Bael, T. S. Koh, Z. Shi, D. E. Savage, M. G. Lagally, R. Joynt, M. Friesen, S. N. Coppersmith, and M. A. Eriksson, Phys. Rev. Lett. **106**, 156804 (2011).

[131] A. Tyryshkin, S. Lyon, T. Schenkel, J. Bokor, J. Chu, W. Jantsch, F. Schäffler, J. Truitt, S. Coppersmith, and M. Eriksson, Physica E **35**, 257 (2006).

[132] C. Tahan, M. Friesen, and R. Joynt, Phys. Rev. B **66**, 035314 (2002).

[133] B. A. Glavin and K. W. Kim, Phys. Rev. B **68**, 045308 (2003).

[134] L. Wang and M. W. Wu, J. Appl. Phys. **110**, 043716 (2011).

[135] L. Wang, K. Shen, B. Y. Sun, and M. W. Wu, Phys. Rev. B **81**, 235326 (2010).

[136] K. Shen and M. W. Wu, Phys. Rev. B **76**, 235313 (2007).

[137] C. H. Wong, M. A. Eriksson, S. N. Coppersmith, and M. Friesen, Phys. Rev. B **92**, 045403 (2015).

[138] V. Kornich, C. Kloeffel, and D. Loss, Phys. Rev. B **89**, 085410 (2014).

[139] C. Herring and E. Vogt, Phys. Rev. **101**, 944 (1956).

[140] P. Y. Yu and M. Cardona, *Fundamentals of Semiconductors: Physics and Material Properties*, 4th ed. (Springer, Berlin, 2010).

[141] Z. Wilamowski, W. Jantsch, H. Malissa, and U. Rössler, Phys. Rev. B **66**, 195315 (2002).

[142] L. Vervoort, R. Ferreira, and P. Voisin, Phys. Rev. B **56**, R12744 (1997).

[143] L. Vervoort, R. Ferreira, and P. Voisin, Semicond. Sci. Technol. **14**, 227 (1999).

[144] M. O. Nestoklon, E. L. Ivchenko, J.-M. Jancu, and P. Voisin, Phys. Rev. B **77**, 155328 (2008).

[145] V. Kornich, C. Kloeffel, and D. Loss, Phys. Rev. B **90**, 079901(E) (2014).

[146] D. Culcer, L. Cywiński, Q. Li, X. Hu, and S. Das Sarma, Phys. Rev. B **82**, 155312 (2010).

[147] A. V. Kuhlmann, J. Houel, A. Ludwig, L. Greuter, D. Reuter, A. D. Wieck, M. Poggio, and R. J. Warburton, Nat. Phys. **9**, 570 (2013).

[148] D. Kim, D. R. Ward, C. B. Simmons, J. K. Gamble, R. Blume-Kohout, E. Nielsen, D. E. Savage, M. G. Lagally, M. Friesen, S. N. Coppersmith, and M. A. Eriksson, Nat. Nanotechnol. **10**, 243 (2015).

[149] X. Hu and S. Das Sarma, Phys. Rev. Lett. **96**, 100501 (2006).

[150] D. Culcer, X. Hu, and S. Das Sarma, Appl. Phys. Lett. **95**, 073102 (2009).

[151] L. Cywiński, R. M. Lutchyn, C. P. Nave, and S. Das Sarma, Phys. Rev. B **77**, 174509 (2008).

[152] L. Viola, S. Lloyd, and E. Knill, Phys. Rev. Lett. **83**, 4888 (1999).

[153] D. Kim, D. R. Ward, C. B. Simmons, D. E. Savage, M. G. Lagally, M. Friesen, S. N. Coppersmith, and M. A. Eriksson, NPJ Quantum Information **1**, 15004 (2015).

[154] M. D. Reed, B. M. Maune, R. W. Andrews, M. G. Borselli, K. Eng, M. P. Jura, A. A. Kiselev, T. D. Ladd, S. T. Merkel, I. Milosavljevic, E. J. Pritchett, M. T. Rakher, R. S. Ross, A. E. Schmitz, A. Smith, J. A. Wright, M. F. Gyure, and A. T. Hunter, arXiv:1508.01223.

[155] X. Hu, Phys. Rev. B **83**, 165322 (2011).

[156] A. L. Saraiva, M. J. Calderón, R. B. Capaz, X. Hu, S. Das Sarma, and B. Koiller, Phys. Rev. B **84**, 155320 (2011).

[157] M. O. Nestoklon, L. E. Golub, and E. L. Ivchenko, Phys. Rev. B **73**, 235334 (2006).

[158] S. Chutia, S. N. Coppersmith, and M. Friesen, Phys. Rev. B **77**, 193311 (2008).

[159] J. K. Gamble, M. A. Eriksson, S. N. Coppersmith, and M. Friesen, Phys. Rev. B **88**, 035310 (2013).

[160] T. B. Boykin, G. Klimeck, M. A. Eriksson, M. Friesen, S. N. Coppersmith, P. von Allmen, F. Oyafuso, and S. Lee, Appl. Phys. Lett. **84**, 115 (2004).

[161] D. Rugar, H. J. Mamin, M. H. Sherwood, M. Kim, C. T. Rettner, K. Ohno, and D. D. Awschalom, Nat. Nanotechnol. **10**, 120 (2015).

[162] H. Fröhlich and F. R. N. Nabarro, Proc. R. Soc. London, Ser. A **175**, 382 (1940).

[163] M. A. Ruderman and C. Kittel, Phys. Rev. **96**, 99 (1954).

[164] T. Kasuya, Prog. Theor. Phys. **16**, 45 (1956).

[165] K. Yosida, Phys. Rev. **106**, 893 (1957).

[166] D. C. Dixon, K. R. Wald, P. L. McEuen, and M. R. Melloch, Phys. Rev. B **56**, 4743 (1997)

[167] T. Machida, S. Ishizuka, T. Yamazaki, S. Komiyama, K. Muraki, and Y. Hirayama, Phys. Rev. B **65**, 233304 (2002).

[168] E. V. Deviatov, A. Würtz, A. Lorke, M. Yu. Melnikov, V. T. Dolgopolov, D. Reuter, and A. D. Wieck, Phys. Rev. B **69**, 115330 (2004).

[169] C. J. Trowbridge, B. M. Norman, Y. K. Kato, D. D. Awschalom, and V. Sih, Phys. Rev. B, **90**, 085122 (2014).

[170] K. Chida, M. Hashisaka, Y. Yamauchi, S. Nakamura, T. Arakawa, T. Machida, K. Kobayashi, and T. Ono, Phys. Rev. B **85**, 041309 (R) (2012).

[171] S. Chesi and W. A. Coish, Phys. Rev. B **91**, 245306 (2015).

[172] G. Tatara, H. Kohno, and J. Shibata, Phys. Rep. **468**, 213301 (2008).

[173] F. Li, T. Nattermann, and V. L. Pokrovsky, Phys. Rev. Lett. **108**, 107203 (2012).

[174] K. M. D. Hals and A. Brataas, Phys. Rev. B **87**, 174409 (2013).

[175] J. C. Budich, F. Dolcini, P. Recher, and B. Trauzettel, Phys. Rev. Lett. **108**, 086602 (2012).

[176] J. Maciejko, C. Liu, Y. Oreg, X.-L. Qi, C. Wu, and S.-C. Zhang, Phys. Rev. Lett. **102**, 256803 (2009).

[177] T. L. Schmidt, S. Rachel, F. von Oppen, and L. I. Glazman, Phys. Rev. Lett. **108**, 156402 (2012).

[178] A. M. Lunde and G. Platero, Phys. Rev. B **86**, 035112 (2012).

[179] A. Del Maestro, T. Hyart, and B. Rosenow, Phys. Rev. B **87**, 165440 (2013).

[180] P. Stano and D. Loss, Phys. Rev. B **90**, 195312 (2014).

[181] A. A. Zyuzin, T. Meng, V. Kornich, and D. Loss, Phys. Rev. B **90**, 195125 (2014).

[182] T. Meng, P. Stano, J. Klinovaja, and D. Loss, Eur. Phys. J. B **87**, 203 (2014).

[183] Y. Oreg, G. Refael, and F. von Oppen, Phys. Rev. Lett. **105**, 177002 (2010).

[184] R. M. Lutchyn, J. D. Sau, and S. Das Sarma, Phys. Rev. Lett. **105**, 077001 (2010).

[185] G. E. Volovik, *The Universe in a Helium Droplet* (Oxford University Press, Oxford, 2003).

[186] M. Sato and S. Fujimoto, Phys. Rev. B **79**, 094504 (2009).

[187] L. Fu and C. L. Kane, Phys. Rev. Lett. **100**, 096407 (2008).

[188] V. Mourik, K. Zuo, S. M. Frolov, S. R. Plissard, E. P. A. M. Bakkers, and L. P. Kouwenhoven, Science **336**, 1003 (2012).

[189] M. T. Deng, C. L. Yu, G. Y. Huang, M. Larsson, P. Caro, and H. Q. Xu, Nano Lett. **12**, 6414 (2012).

[190] A. Das, Y. Ronen, Y. Most, Y. Oreg, M. Heiblum, H. Shtrikman, Nat. Phys. **8**, 887 (2012).

[191] L. P. Rokhinson, X. Liu, and J. K. Furdyna, Nat. Phys. **8**, 795 (2012).

[192] E. I. Rashba, Sov. Phys. Solid State **2**, 1109 (1960).

[193] R. Jackiw and C. Rebbi, Phys. Rev. D **13**, 3398 (1976).

[194] J. Klinovaja, P. Stano, and D. Loss, Phys. Rev. Lett. **109**, 236801 (2012).

[195] J. Alicea, Rep. Prog. Phys. **75**, 076501 (2012).

[196] C. H. L. Quay, T. L. Hughes, J. A. Sulpizio, L. N. Pfeiffer, K. W. Baldwin, K. W. West, D. Goldhaber-Gordon, and R. de Picciotto, Nat. Phys. **6**, 336 (2010).

[197] P. Streda and P. Seba, Phys. Rev. Lett. **90**, 256601 (2003).

[198] T. Meng and D. Loss, Phys. Rev. B **88**, 035437 (2013).

[199] C. Fasth, A. Fuhrer, L. Samuelson, V. N. Golovach, and D. Loss, Phys. Rev. Lett. **98**, 266801 (2007).

[200] Y. Kanai, R. S. Deacon, S. Takahashi, A. Oiwa, K. Yoshida, K. Shibata, K. Hirakawa, Y. Tokura, and S. Tarucha, Nat. Nano **6**, 511 (2011).

[201] S. Nadj-Perge, V. S. Pribiag, J. W. G. van den Berg, K. Zuo, S. R. Plissard, E. P. A. M. Bakkers, S. M. Frolov, and L. P. Kouwenhoven, Phys. Rev. Lett. **108**, 166801 (2012).

[202] P. Peddibhotla, F. Xue, H. I. T. Hauge, S. Assali, E. P. A. M. Bakkers, and M. Poggio, Nat. Phys. **9**, 631 (2013).

[203] B. E. Herzog, D. Cadeddu, F. Xue, P. Peddibhotla, and M. Poggio, Appl. Phys. Lett. **105**, 043112 (2014).

[204] P. Simon and D. Loss, Phys. Rev. Lett. **98**, 156401 (2007).

[205] K. Blum, *Density Matrix Theory and Applications,* 2nd ed. (Plenum Press, New York, 1996).

[206] R. White, *Quantum Theory of Magnetism* (Springer, Berlin, 2007).

[207] A. Abragam, *The principles of nuclear magnetism* (Clarendon Press, Oxford, 1961).

[208] P. Maletinsky, A. Badolato, and A. Imamoglu, Phys. Rev. Lett. **99**, 056804 (2007).

[209] A. Sasaki, S. Nonaka, Y. Kunihashi, M. Kohda, T. Bauernfeind, T. Dollinger, K. Richter, and J. Nitta, Nat. Nanotechnol. **9**, 703 (2014).

Viktoriia Kornich

Curriculum Vitae

Date of Birth	07 October 1989
Place of Birth	Debaltsewo, Donetsk Reg., Ukraine

Education

31.03.2016– 1.07.2012	**PhD student**, *in the Condensed Matter Theory group of the University of Basel*, under the supervision of Prof. Dr. Daniel Loss.
30.06.2012– 01.09.2010	**Master of Science**, *Degree in Applied Physics and Mathematics*, at the Faculty of Physical and Quantum Electronics, Moscow Institute of Physics and Technology (MIPT), with distinction. Thesis on AC Response of the Quantum Wire with Bulk Contacts.
30.06.2010– 01.09.2006	**Bachelor of Science**, *Degree in Applied Physics and Mathematics*, at the Faculty of Physical and Quantum Electronics in MIPT, with distinction. Bachelor thesis on Electronic Transport in Quantum Wire with Non-stationary Impurity.
30.06.2010– 01.09.2009	**Translator in the field of professional communication (English-Russian)**, *Certificate of additional education.*
30.06.2006– 01.09.1996	**Grammar School**, *Grammar School N28 (physico-mathematical class) in Zaporizhzhya, Ukraine*, with distinction. The Winner of competitions in Physics, Chemistry and Mathematics. The Winner of the All-Ukrainian competition in Physics of the Youth Academy of Science in 2006, the 2nd place in 2005, etc.
30.05.2005– 01.09.2000	**School of Art**, *in Zaporizhzhya*, Painting, Graphic Art, Sculpture, World History of Art.

Publications (An asterisk denotes a publication covered in this thesis.)

*[6] Viktoriia Kornich, Christoph Kloeffel, and Daniel Loss, *Phonon-assisted relaxation and decoherence of singlet-triplet qubits in Si/SiGe quantum dots*, arXiv:1511.07369.

*[5] Viktoriia Kornich, Peter Stano, Alexander A. Zyuzin, and Daniel Loss, *Voltage-induced conversion of helical to uniform nuclear spin polarization in a quantum wire*, Phys. Rev. B **91**, 195423 (2015).

*[4] Alexander A. Zyuzin, Tobias Meng, Viktoriia Kornich, and Daniel Loss, *Nuclear spin relaxation in Rashba nanowires*, Phys. Rev. B **90**, 195125 (2014).

*[3] Viktoriia Kornich, Christoph Kloeffel, and Daniel Loss, *Phonon-mediated decay of singlet-triplet qubits in double quantum dots*, Phys. Rev. B **89**, 085410 (2014).

[2] V.G. Kornich, S.N. Artemenko, *Electron Transport in Quantum Wire with Non-stationary Impurity*, Non-linear World **2**, 90 (2012), (Russian).

[1] S.N. Artemenko, V.G. Kornich, D.S. Shapiro, *Linear response of quantum wire with bulk contacts*, Electronic Journal of RAS Radioelectronics **11**, 1-17 (2011), (Russian, http://jre.cplire.ru/jre/nov11/index.html).